

Item 830-14-15

NAS 1-60:7/39

JAN 30 1978

NASA Technical Paper 1139

COMPLETED

ORIGINAL

Effects of Mass Addition on Blunt-Body Boundary-Layer Transition and Heat Transfer

George E. Kaattari

JANUARY 1978

NASA

69

NASA Technical Paper 1139

**Effects of Mass Addition
on Blunt-Body Boundary-Layer
Transition and Heat Transfer**

George E. Kaattari
Ames Research Center
Moffett Field, California



**National Aeronautics
and Space Administration**

**Scientific and Technical
Information Office**

1978

SYMBOLS

a_s	area-averaged mass-flow coefficient on porous model surface
A	cross section area of porosity probe tube
b_s	area-averaged function of local mass-flow coefficient and surface pressure on porous model surface
B	stagnation point mass-flow heating rate parameter, $\frac{\dot{m}\Delta H}{\dot{q}_0}$
B'	mass-flow heating rate parameter, reference 9
\underline{B}	area-averaged mass-flow heating rate parameter, $\frac{\dot{m}\Delta H}{\dot{q}_{os}}$
c_s	local mass-flow coefficient on porous model surface
c_f	skin friction coefficient
c_p	specific heat of air or calorimeter slug
k	roughness height
\dot{m}	local mass-flow addition rate
\dot{m}_∞	free-stream mass-flow rate
$\underline{\dot{m}}$	area-averaged mass-flow addition rate to a given location, s
$\underline{\dot{m}}^*$	mass-flow rate ratio, $\frac{\dot{m}}{\dot{m}_\infty}$
P	pressure
\dot{q}_0	reference heat transfer coefficient (stagnation point value on hemisphere model at $\dot{m} = 0$)
\dot{q}_{os}	local heat transfer coefficient at s with $\underline{\dot{m}} = 0$
$\underline{\dot{q}}_{os}$	area-averaged heat transfer coefficient up to location s on model surface with $\underline{\dot{m}} = 0$
\dot{q}_s, \dot{q}	local heat transfer coefficient at s with $\underline{\dot{m}} \neq 0$
Re	Reynolds number
r	normal distance to point on model surface from axis of symmetry

s	radial distance from model apex (stagnation point) measured along model surface
t	time, sec
T	temperature, K
T'	turbulence intensity, reference 8
ΔH	heat-transfer driving potential, $c_p(T_{tt} - T_w)$
θ	momentum thickness
μ	viscosity of air
ρ	air density or calorimeter density
τ	calorimeter slug length
ϕ	azimuthal angle on model surface
ψ	stagnation point heating rate ratio, $\frac{\dot{q}}{\dot{q}_0}$
ψ'	function of B', reference 9
$\frac{\psi}{-}$	heating rate ratio, $\frac{\dot{q}_s}{\dot{q}_{0s}}$

Subscripts:

D	model diameter
ex	external surface of model
in	internal surface of model
lam	laminar
st	stagnation point
trns	transition point on model surface
tt	tunnel total condition
turb	turbulent
w	model wall or surface
∞	free-stream condition

EFFECTS OF MASS ADDITION ON BLUNT-BODY BOUNDARY-LAYER

TRANSITION AND HEAT TRANSFER

George E. Kaattari

Ames Research Center

SUMMARY

Heat-transfer data were obtained on blunt models at Mach number 7.32 and free-stream Reynolds numbers in the range of 0.6×10^6 to 5.2×10^6 to investigate the effect of ablation on boundary-layer transition. Ablation was simulated by mass addition of air through the porous surface of the models. The ratio of the mass addition rate to the free-stream mass flow was varied from 0 to 0.5. The models were 17.8 cm in diameter and consisted of hemispheres, spherical segments, and blunted 60° cones.

The data were compared with various applicable boundary-layer codes in the laminar and transitional flow regimes. Empirical heating rate data correlations were developed for the laminar and turbulent flow regimes.

INTRODUCTION

Vehicles entering planetary atmospheres at high speeds are enveloped by high-temperature shock layers. At sufficiently high speeds, certain surface materials may ablate from the vehicle in gaseous form and protect the vehicle at the expense of surface material mass loss. The transferred heat from the high-temperature shock envelope is expended by converting a thin layer of the vehicle surface into hot ablative products that are subsequently carried away by the external flow field. Problems then arise in predicting the effect of ablation of heat transfer (particularly in the turbulent flow regime) and in predicting the effect of ablation on the transition from laminar to turbulent flow.

Much experimental and theoretical study has been devoted to predicting laminar heat transfer in the presence of ablation for both blunt and slender configurations. These studies (refs. 1-5) indicate a reduction in heat transfer and have produced correlations and theory relating the heat transfer decrease as a function of the ablation rate. Along with ablation, the effects of surface roughness and free-stream turbulence on transitional and turbulent flow have been studied (refs. 6-9). Some results of these investigations are compared with the results of the present investigation.

Studies of heat transfer in the literature are largely restricted to low ablation rates. The present investigation involves massive rates, approaching those anticipated for Jovian atmosphere entry. The primary purpose, along

with providing boundary-layer transition data, is to determine to what extent massive ablation affects turbulent heat transfer rates. This aspect of ablation is important both in planetary exploration and in military application since, if the heating rate is significantly increased, nonuniform heat shield erosion and attendant thermal stress and aerodynamic stability problems may arise.

EXPERIMENTAL CONSIDERATIONS

Models

The models used consisted of three 6.35-mm-thick porous, stainless steel headers in the forms of a hemisphere, a 60° blunt cone, and a spherical segment, as shown in figure 1. The headers were made interchangeable to a steel pressure chamber to which air was led through piping. The assembled header, chamber, and support system are shown in figure 2. Each header was provided with 15 to 16 calorimeters. A calorimeter (fig. 1) consisted of a 1.6-mm-diameter, 1.27-mm-long copper slug tightly fitted into a cavity at the end of a 2.4-mm-diameter, 13.7-mm-long insulating dowel. A chromel-constantan junction was peened to the base of the slug and the wire leads passed through the dowel to a male plug. Each calorimeter was press-fitted to the header hole so that the dowel and slug surface were flush to the header external surface. Each header was also provided with five 1.6-mm stainless steel tube pressure taps. Figure 1 gives the location of the calorimeters and pressure taps for each header. Although the figure indicates spacing of the calorimeters in a single radial plane, they were actually arranged in a spiral 360° pattern to reduce "downwind" interference effects. Not shown in figure 1 are thermocouples that were interdigitated with the calorimeter locations and spotted to the internal surface of the header. These thermocouples monitored the entering air temperature during the tests. The pressure taps were located in a single radial plane as indicated.

The models were intended to have uniform porosity. No attempt was made to "tailor" header porosity to simulate ablated mass addition rate distribution of actual atmospheric entry. Pretest porosity surveys of the headers indicated the presence of manufacturing imperfections resulting in deviation from uniform porosity. Figure 3 shows a plot of representative mass-flow rate variations with radial distance s determined from the porosity surveys. Except for deficiencies near the stagnation region existing for the hemispherical models and the conical models (not shown), the porosity deviation was generally within $\pm 10\%$ of the mean value.

Initial tests were made to check out the systems and to determine the feasibility of the thermocouple installation. Some model degradation occurred during these initial tests. The hemispherical and spherical segment models were refurbished, and the conical model was replaced since the original model proved to have a nearly impervious nose section. The refurbishing and replacement resulted in models with somewhat different porosity distributions. The altered models were tested to a higher mass-flow rate range in the second

phase of the investigation. To distinguish the results presented herein, the models are referred to by phase number, that is, by model 1 or model 2.

Test Conditions and Procedures

The tests were performed in the Ames 3.5-Foot Hypersonic Wind Tunnel at Mach number 7.32. A description of the facility and its operations appears in reference 11. The Reynolds number, based on model diameter, ranged from 0.6×10^6 to 5.2×10^6 and the temperature from 660 to 880 K.

A test run established a predetermined flow rate of air through the model at about 27° C, the flow being gaged with a swirlmeter. The model was then inserted into the tunnel windstream for about 1-1/2 sec, during which interval a shadowgraph picture of the model was taken and the time-temperature history of the model calorimeters was recorded. The pressure transducers reached equilibrium well within the insertion time. The mass-flow rate ratios with respect to free-stream flow varied from 0.0 to a maximum value of about 0.5 for cone model 2 at the lower Reynolds number range.

Data Reduction

Mass-addition rate distribution—Pretest porosity surveys of the model headers were required to determine mass-addition flow rates as a function of radial location, s . This was accomplished by pressurizing the chamber and holding to the external header surface a 6.4-mm-diameter "sniffer" tube attached to a low-capacity floatmeter. Floatmeter readings were taken at 6.4-mm intervals in the radial direction and at 5° intervals in the azimuthal direction. The local conductance c_s at each location on the header surface was then evaluated with the equation

$$\dot{m}_s = c_s A (P_{in}^2 - P_{ex}^2) \quad (1)$$

where

\dot{m}_s = flow rate measured by the floatmeter

A = area of the "sniffer" tube

P_{in} = chamber pressure

P_{ex} = external (atmosphere) pressure

The local conductances were area-integrated to determine the mean conductance. This conductance coefficient was then checked with a high-capacity venturi meter by passing air through the header. The resulting flow rate was compared with that calculated by equation (1) using the mean conductance and total header area. The comparison gave satisfactory agreement for a wide

range of chamber pressures. Proportional adjustments to the local values of c_s were made to bring the calculated flow rate into exact agreement with the venturi-meter measurements.

The mass-addition flow rate distribution used in this investigation was defined as the area-integrated unit mass flow to the radial position s of interest. The mass flow rate determinations for the test runs involved a variable external pressure P_{ex} as well as the variable conductance coefficient c_s . These were taken into account by equation (2).

$$\dot{m} = a_s P_{in}^2 - b_s P_{tt}^2 \quad (2)$$

where P_{tt} is the tunnel total pressure. The coefficients a_s and b_s were tabulated as functions of radial location s , dependent on the local conductance of each model and the external pressure suitably related to the tunnel total pressure. Detailed derivation of equation (2) is given in the appendix.

The mass-flow rate distributions for all test runs of the investigation, calculated with equation (2), are presented in tables 1 to 4.

Heating rate distribution—The heat transfer rates were calculated from calorimeter temperature versus time transients recorded while the model was in the tunnel stream. The usual formula was applied, namely

$$\dot{q}_s = \rho c_p \tau \left(\frac{dT}{dt} \right) \quad (3)$$

Because of slight misalignments in positioning the calorimeter surfaces flush to the external header surface, repeatable scatter in the heat transfer rates was noted. The magnitude of the scatter was determined by comparing the no-flow results of the present tests with unpublished test results of identically proportioned, solid thin-skin models tested in the same tunnel and flow conditions. Correction factors were determined for each calorimeter such that the ablation model results at the condition of no-flow were made to agree with those of the solid thin-skin models.

Transition location—The tested models had a decreasing heating rate distribution with distance s from the stagnation point at the lower Reynolds numbers and at near-zero mass addition rates. This distribution is characteristic of laminar heating for the model shapes considered. The transition from laminar to turbulent flow at certain increased mass addition rates was made evident by sudden increases in heating rates occurring beyond a definite location s . This location or transition point s_{trns} in the present investigation was defined as the last location beyond which point a reversal to an increased heating rate occurred. The transition point is evident in figures 4(a)-(e). The transition point and other significant features of the heating rate distributions are labeled in figure 4(c) where they are particularly well defined.

RESULTS AND DISCUSSION

Experiment

The heat-transfer distribution results for the range of variables test are presented in figures 4 to 9 in the form of normalized heat-transfer coefficients plotted as a function of distance s from the stagnation point location of the models. A nominal mass addition rate ratio parameter \underline{m}^* is associated with each curve of the figures. The test numbers and pertinent flow variables are also indicated. The reference heat-transfer coefficient \dot{q}_0 is the theoretical stagnation point value for a 17.8-cm-diameter hemisphere with no mass addition at the test conditions of each run.

Table 1 contains tabulations of the mass addition flow rate distributions \dot{m} as a function of s for each run presented in figures 4 to 9. The value of the free-stream mass-flow rate \dot{m}_∞ of each run is also listed for convenience in determining the local mass addition flow rate ratio ($\underline{m}^* = \dot{m}/\dot{m}_\infty$) if desired.

Hemispherical models— The results for hemispherical model 1 are presented in figure 4. The mass addition initially decreased the level of heating over the entire model surface with increasing \underline{m}^* and indicated the presence of a laminar boundary layer. Then, with further increases in \underline{m}^* , a transition to a turbulent boundary layer occurred, as indicated by a rapid increase in heating rates beginning at definite locations s as previously described (at $s = 2.5$ cm in fig. 4(a) and at $s = 5.8$ cm in fig. 4(c)). The transition location shifted progressively to lower values of s with increasing values of \underline{m}^* , as is particularly evident from figures 4(c) and 4(e). Continued increases in \underline{m}^* ultimately decreased the heating rates, as is shown in figure 4(d). Note that the heating rates at, and near, the stagnation point $s = 0$ are relatively insensitive to \underline{m}^* . This phenomenon was also noted in a similar investigation of a hemisphere reported in reference 1.

The heating rate distributions for hemispherical model 2 are presented in figure 5. Most of the data were taken at higher mass addition flow rate ratios \underline{m}^* than with model 1. Tests with model 2 were also run at a lower Reynolds number (0.5×10^6). The mass addition rate distribution of the two models (tables 1 and 2) differs somewhat, model 2 being less permeable to flow near the stagnation point. Model 2 also had a local flow rate irregularity at $s \approx 1.3$ cm, which caused a conspicuous perturbation in the heating rate in that vicinity. The transition point movement with increasing \underline{m}^* is apparent in figure 5(e).

Spherical segment models— The results for the spherical segment models are presented in figure 6. The effect of small negative mass addition rates, shown in the data of figures 6(a) and 6(c), causes large increases in heating rates, undoubtedly due to partial inspiration of the oncoming hot airstream. Positive values of mass addition affected the heat transfer in a similar manner as that noted for the hemispherical models. In the case of the spherical model, however, no progressive movement toward the stagnation region

occurred at the lowest Reynolds numbers (fig. 6(a)) and the transition location became established at $s = 3.3$ cm and remained fixed for values of \underline{m}^* from 0.018 to 0.079. A perceptible shift of the transition point from $s = 3.6$ cm to $s = 2.5$ cm occurs in the range of \underline{m}^* presented in the intermediate Reynolds number range (fig. 6(b)). The largest Reynolds number data (fig. 6(c)) exhibit the same behavior as those of figure 6b; however, calorimeter malfunction precluded definite fixes for the transition location. The large increase in heating rate in the stagnation regions at Reynolds number 4.93×10^6 with $\underline{m}^* = 0.004$ (round symbols, fig. 6(c)) was probably due to combined effects of mass addition and tunnel free-stream turbulence since, at this Reynolds number, enhanced heating rates were also found at $\underline{m}^* = 0$ in preliminary tests of a thin-skin nonporous version of the spherical segment model (dashed-line curve). The spherical segment model did not exhibit the stagnation point heating rate insensitivity to mass addition to the degree noted for the hemispherical models.

The heating rate distributions for the spherical segment model 2 are presented in figure 7. Model 2 generally exhibited higher heating rates near the stagnation point than did model 1 under similar flow conditions. The difference in heating rates was probably due to differences in the mass addition rate distributions between the models (tables 2 and 4). Model 2 had a somewhat irregular mass flow distribution, with minimum values near $s = 0$. Model 1 had a nearly constant mass flow distribution over the entire model surface. The nonuniform mass addition rate distribution of model 2 may have caused its somewhat earlier transition to turbulent flow.

Conical models—The test results for conical model 1 are presented in figure 8. The effects of mass addition on the heating rate distribution followed the pattern of the hemispherical models. The transition point moved forward (towards $s = 0$) with increasing values of \underline{m}^* (figs. 8(a), 8(c), and 8(e)). Large heating rate increases resulted when transition-to-turbulent flow was attained at the larger Reynolds numbers (fig. 8(c), run 63C1 and fig. 8(e), run 70C1). The range of s which was relatively impervious to flow is noted ($0 < s < 3.4$) in figure 8. However, there is a small effect of mass "leakage" in this region which, at the highest Reynolds number (fig 8(e)), was sufficient to cause early transition to turbulent flow (runs 71C1 and 73C1).

The heating rate distributions for cone model 2 are presented in figure 9. Comparison of the data between models 1 and 2 at approximately the same flow conditions (run 45C1 and 42C2) indicates turbulent flow for model 2 and transitional flow for model 1. The differences in heat transfer rates between the models must then be due to gross differences in mass addition rate distributions (tables 5 and 6). Model 1 had an nearly impervious nose section; model 2 was porous over the entire surface. Table I indicates, however, that the mass flow rate distribution for model 2 varied in an irregular manner. A particularly "high spot" occurred at $s = 1.27$ cm. This is reflected in the heating rate data of figure 9 by a substantially reduced heating rate at this location. It should be clarified that the irregular mass flow distribution of model 2 was in respect to azimuthal location. The radial or s -wise distribution was fairly uniform upstream of each calorimeter location; thus, "high

spots" of mass addition were only apparent locally and were not instrumental in promoting early flow transition.

Correlations

The results of the investigation were examined and attempts were made to correlate the results. Limited comparisons were made with the results of other investigations.

Laminar heating rates—A semiempirical method for correlating the effect of mass addition on laminar heat transfer distribution is described and compared with a more sophisticated method and with experimental results of the present investigation.

The effect of mass addition on stagnation point heating (ref. 2) is generally well predicted for laminar flow by

$$\begin{aligned}\psi &= \frac{\dot{q}_s}{\dot{q}_o} \\ &= 1 - 0.72B + 0.13B^2\end{aligned}\quad (4)$$

The term ψ is the ratio of the heat transfer coefficient \dot{q}_s at the stagnation point in the presence of mass addition with respect to the heat transfer coefficient \dot{q}_o with no mass addition. The independent variable $B = \dot{m}\Delta H/\dot{q}_o$ is the mass addition parameter. Equation (4) was found to apply to locations other than the stagnation point when the term ψ was redefined as $\psi = \dot{q}_s/\dot{q}_{os}$, or the ratio of the heat transfer coefficient at location s in the presence of mass addition with respect to the coefficient at the same location with no mass addition. The mass addition parameter B is modified to $B = \dot{m}\Delta H/\dot{q}_{os}$. The term \dot{m} is the area-averaged mass-addition rate to the location s and $1/\dot{q}_{os}$ is the area-averaged, inverse heat transfer coefficient (no mass addition) to the same location

$$\dot{q}_{os}^{-1} = \frac{\int_0^s r \frac{ds}{\dot{q}_{os}}}{\int_0^s r ds} \quad (5)$$

Equation (4) in the modified form was tested for the hemispherical model by correlating surface heating rates generated with the boundary-layer code reported in reference 5. The results are shown in figure 10(a) for various mass addition rate distributions. The agreement is considered good. Some small second-order deviations from perfect agreement are apparent.

Experimentally determined surface heating data for the hemispherical models were similarly correlated with equation (4). The results are shown in figure 10(b). Note that the conspicuous perturbations in the heat transfer coefficients of model 2 at $s \approx 1.7$ cm (shown previously in fig. 5) do not impair the correlation of figure 10(b) (solid symbols).

The correlation of the heating data over the spherical segment model surfaces with modified equation (4) is shown in figure 10(c). Generally fair agreement is indicated except for the data of run 97SS2.

The data of conical model 1 (fig. 10(d)) correlates well, with the exception of some data points of run 45C and an isolated data point of run 63C1. Only the data of model 1 were considered since most of the model 2 data were taken at high mass-addition rates where transition occurred close to the stagnation point.

No effect of Reynolds number was apparent in the correlations of the data of figures 10.

Anomalous stagnation point heating— In the experimental results, the heating rates at the stagnation point were relatively insensitive to mass addition rates. This fact was most evident for the hemispherical model data. In reference 1, similar results were noted for a hemispherical model tested at Mach number 5 with nitrogen gas for mass addition. The results of reference 1 and the present data are compared in figure 11(a). The free-stream Reynolds number based on model diameter is closely matched. Statistically, the present results indicate less effect of mass addition than those of reference 1, although the results overlap at Reynolds number 5.2×10^6 . No consistent effect of free-stream Reynolds number is evident in figure 11(a) in the data of reference 1 or of the present investigation.

The effect of mass addition on stagnation point heating for the spherical segment model is shown in figure 11(b). The data indicate that the heat transfer rates are reduced significantly compared to those for the hemispherical model. The data tend to approach the laminar distribution, but nevertheless are still far above theoretical expectations at large injection rates.

The effect of mass addition on the stagnation point heating of the conical models is not well documented. Model 1 was impervious to mass addition at the stagnation point and only three test runs performed in the mass addition range, $0 < \underline{B} < 3$, with conical model 2. These runs gave values of \dot{q}/\dot{q}_0 ranging from 1.01 to 0.95, indicating the least effect of mass addition on the stagnation point heating among the three configurations tested.

The apparent configuration effect on the stagnation point heating indicated by the present data is probably a scale effect due to nose radius, which primarily affects the stagnation point velocity gradient.

High heating rates (above laminar) at the stagnation point can be caused by free-stream turbulence (ref. 6). The difference in the two sets of data in figure 11(a) may then be ascribed to the turbulence levels in the facilities used. A peculiarity of the heating rate distribution immediately downstream of the stagnation point occurs in the present data and is particularly evident for the hemispherical models in the $\underline{\psi} - \underline{B}$ coordinate plots of figure 12. The data of the indicated runs do not correlate with the predicted laminar (dash line) curve, but plot on a series of parallel curves. Apparently, the enhancement due to turbulence at the stagnation point does

not persist downstream, and the flow tends to be laminar-like up to the point where transition ultimately occurs.

Boundary-layer transition—Gaseous mass addition from a body surface forms a layer that interfaces with the external flow. At small mass addition rates, the layer is thin and the interface is stable. When mass addition is increased, the layer thickens and, ultimately, the interface becomes unstable. Turbulent mixing with the external flow ensues with concomitant increase in heat transfer to the body surface. The beginning of instability, or transition, was evident in the data previously described where a sudden increase in heating rates occurred with increased mass addition. The problem of predicting the occurrence of transition as affected by mass addition is complicated by other contributing factors. Two significant parameters have received experimental and theoretical study (refs. 6-9) and are discussed in the light of the present investigation.

Effect of free-stream turbulence: While free-stream turbulence was not an experimental variable in this investigation, it is an important factor in comparing data from different facilities. A correlation between computed transition Reynolds numbers utilizing the test conditions and tunnel turbulence level T of the present investigation was found by Mr. Wilcox of DCW Industries and is presented in reference 8. This theoretically based correlation relates the boundary-layer edge Reynolds number to the local flow rate momentum thickness Reynolds number at the transition location of the hemispherical models by

$$\frac{Re_{trns}}{43000} = 1 + 41 \exp\left(-\frac{13}{12} \frac{\dot{m}_0}{\rho U} \frac{trns}{\mu}\right) \quad (6)$$

Experimental transition point Reynolds numbers for the hemispherical models are shown in figure 13. The data are represented by sets of two points. The lower point of each set indicates incipient transition. The upper point (with arrowhead) represents completed transition. The data sets bracket the theoretical correlation curve at all Reynolds numbers. However, in general, the experimental values indicate earlier transition than is predicted, particularly at the lower Reynolds numbers. The relatively poor correlation at the lower Reynolds numbers (lower surface pressures) may possibly be attributed to "mass-flow roughness" or minute jetting action, which tends to be suppressed at the higher Reynolds numbers.

Effect of surface roughness: A degree of surface roughness existed in the models of the present investigation because of the permeable, porous structure necessary to permit mass flow through the surface. A photomicrograph of the hemispherical model surface section (fig. 14) shows a fairly consistent surface texture in terms of "valley-to-peak" height. This dimension was taken as the roughness parameter k of the model. The experimental transition Reynolds number based on momentum thickness was compared with those given by the correlation relationship of reference 9, where combined roughness and mass addition rates are taken into account

$$Re_{\theta_{trns}} \left(\frac{1}{\psi'} \frac{k}{\phi_{trns}} \right)^{0.7} = 215 \quad (7)$$

where

$$\psi' = \left[\frac{B'}{10} + \left(1 + \frac{B'}{4} \right) \frac{\rho_e}{\rho_w} \right]$$

Qualifications for application of the above correlation relationship are stated in reference 9: "A computed value of 255 must be reached or exceeded at the sonic point location; if this condition is satisfied, the transition zone is predicted to physically begin at the surface point where this parameter attains a value of 215. If predicted to occur, the transition zone will always be located in the subsonic flow region." The correlation relationship (eq. (7)) was tested with the hemispherical model data. The results are shown in figure 15. The data group labeled $Re_{\theta} < 255$ and two data points with transition occurring beyond the sonic point do not meet the qualifications quoted above and also do not correlate. The remaining data meet the qualifications and are in fair accord with the indicated PANT correlation curve.

Turbulent heating rates— The $\dot{q} - B$ curves of figures 10(a) through 10(d), discussed previously, relate the heating rate in the presence of mass addition with reference to a no-mass-addition laminar heating rate as a function of the mass flow rate parameter. Satisfactory correlation of the experimental results over the model surfaces was obtained at low mass-addition rates. Logically, the effect of mass-addition in the cases where turbulent heating is predominant should be measured with respect to a no-mass-addition turbulent heating rate reference. A correlation of the data on this premise was made and is described in the following paragraph.

Turbulent flow factor: The procedure for correlating the turbulent heating rate data of this investigation was simply to multiply the laminar based coordinates \dot{q} and B by the factor $\dot{q}_0/\dot{q}_{0,turb}$, thus shifting them to a turbulent heating rate reference. Numerical values for the factor were obtained by applying Reynolds analogy (proportionality) between heat and skin friction coefficients

$$\frac{c_{f, lam}}{c_{f, turb}} = \frac{1.328 \times Re^{-0.5}}{0.072 \times Re^{-0.2}} = \frac{\dot{q}_0}{\dot{q}_{0,turb}} = \frac{18.44}{Re^{0.3}} \quad (8)$$

The numerical values for the skin friction coefficients c_f were taken from reference 10.

Turbulent heat transfer correlations: The turbulent flow factor defined in equation (8) was applied to the laminar parameters \dot{q} and B to convert them to turbulent flow parameters

$$\left(\frac{18.44}{Re_D^{0.3}}\right) \psi = \psi_{turb}$$

and

(9)

$$\left(\frac{18.44}{Re_D^{0.3}}\right) B = B_{turb}$$

Turbulent data were taken as the values downstream of the peak heating rate after transition (see fig. 4(c)). The turbulent data of the hemispherical models were plotted in the above defined $\psi_{turb} - B_{turb}$ coordinates of figure 16(a) as case I. All data of both models and Reynolds numbers correlate except for the data of model 1 at the highest Reynolds number (solid symbols). The data from the hemispherical model at this Reynolds number (fig. 4(e)) show a more pronounced shift of the transition point with mass addition than is generally the case with the data at lower Reynolds numbers. An attempt to account for the fact that the flow was not fully turbulent over the entire model surface in all cases was made in the following approximate manner: The local reference \dot{q}_{os} (eq. (5)) was assumed to retain laminar values up to the midpoint location between the transition point and peak turbulent heating point and then to assume the fully turbulent value to the point in question. The "weighted" reference \dot{q}_{os} was used to modify the values of ψ_{turb} and B_{turb} . The data, plotted in the modified coordinates, are shown as case II in figure 16(a). The high Reynolds number data in this case correlates with the data at the lower values. The scatter of the data is random and the correlation is considered satisfactory.

The data of conical model 1 was plotted only in the fully turbulent coordinates defined by equation (9). The results are shown in figure 16(b). An excellent correlation of the data in the Reynolds number range tested is evident. The high degree of correlation is due, in part, to the fact that the plotted data were confined to runs having approximately the same transition point location. In addition, the reference coefficients \dot{q}_{os} and \dot{q}_{os} are relatively independent of s in the transition region; thus, ψ_{turb} and B_{turb} are less sensitive to transition point shifts than in the case of the hemispherical model. In this regard, preliminary plots of the data in "transition modified" coordinates indicated no significant changes to the degree of correlation shown by the fully turbulent correlation shown in figure 16(b).

Correlation of conical model 2 and the spherical model data was not attempted. Thermocouple failures in the region of anticipated turbulent flow for conical model 2 precluded well-defined indications of turbulent heating. Data for the spherical models did not indicate the development of fully turbulent flow as was well-noted by the "peak heating" locations evident for the hemispherical models and conical model 1.

CONCLUSIONS

An experimental investigation was made of the effects of mass addition on the heat transfer to hemispheres, spherical segments, and blunted 60° cone models at Mach number of 7.4 in free-stream Reynolds number range 0.6 to 5.2×10^6 based on model diameter. The ratio of mass-addition rate to free-stream mass flow was varied from 0 to about 0.5. The results of this investigation were compared with empirically derived correlations and with the applicable results of various computer codes. Significant features of the data and conclusions drawn from comparisons of the data with applicable boundary-layer theories follow.

The theoretically predicted effect of mass addition on stagnation point heating in laminar flow (ref. 2) was extended by an empirical, area-averaged heating reference technique to correlate laminar heat transfer distributions over the models' surfaces. The method was in good agreement with the results of both experiment and the laminar boundary-layer code of reference 5.

Anomalously high stagnation point heating based on laminar theory was noted in the data of the present investigation. The same results were found in a similar investigation reported in reference 1. Enhanced stagnation point heating is generally believed to be due to free-stream turbulence. The data of the present investigation at low mass addition rates seem to indicate that the anomalous stagnation point heating is due to localized turbulence with subsequent downstream flow tending to become laminar.

The effect of free-stream turbulence on boundary-layer transition has been investigated theoretically (ref. 7). Using this work as a basis, and utilizing the tunnel test conditions and turbulence level of the present investigation, reference 8 presents a formula (eq. (6)) relating the boundary-layer edge transition Reynolds number to the local momentum thickness and ablation rate for the hemispherical model. This relationship correlated the experimental data satisfactorily, particularly at the higher Reynolds number where transition was markedly abrupt.

The effect of surface roughness on transition has been investigated theoretically (ref. 9). This work presents a correlation of momentum thickness Reynolds number at transition as a function of local mass flow, momentum thickness, and roughness parameter (eq. (7)). Although not a considered variable in the present investigation, roughness measurements were available for the hemispherical model and some experimental confirmation of the correlation was found. The correlation was limited in extent due to qualifying restrictions.

The empirical correlation parameters ψ and B for laminar flow heat-transfer distributions were modified by application of Reynolds analogy, and correlation of heat-transfer distribution data was extended to areas of turbulent flow on the conical and hemispherical models.

Ames Research Center

National Aeronautics and Space Administration

Moffett Field, California 94035, Sept. 8, 1977

APPENDIX

DERIVATION OF MASS-FLOW RATES

The computation required for the area-averaged mass-flow rate distribution for each test run was cast into a convenient form requiring only the measured model internal pressure, the tunnel total pressure, and tabulated factors predetermined for each model. The derivation of the form used in the computation follows.

The local mass-flow rate associated with the differential area element, $r d\phi ds$, at the radial distance, r , from the stagnation point is

$$\dot{m} = \frac{c_s (P_{in}^2 - P_{ex}^2) r d\phi ds}{r d\phi ds} \quad (A1)$$

P_{in} and P_{ex} are the local internal and external pressures on the porous header, and c_s is the flow coefficient at location r .

Equation (A1) is integrated in the azimuthal direction ϕ .

$$\dot{m} = \frac{d\phi \int_0^s c_s (P_{in}^2 - P_{ex}^2) r ds}{d\phi \int_0^s r ds} \quad (A2)$$

The value of P_{in} is constant for a given run. The variable P_{ex} is a function of s and of the tunnel total pressure P_{tt} .

$$P_{ex} = f(s, M_\infty) P_{tt}$$

from

$$P_{ex} = \frac{P}{P_{st}} \frac{P_{st}}{P_{tt}} P_{tt}$$

since

$$\frac{P}{P_{st}} = f(s), \text{ theory or experiment}$$

and

$$\frac{P_{st}}{P_{tt}} = f(M_\infty), \text{ a constant}$$

Substituting the above into equation (A2)

$$\dot{m} = \frac{\int_0^s c_s [P_{in}^2 - f^2(s, M_\infty) P_{tt}^2] r ds}{\int_0^s r ds} = a_s P_{in}^2 - b_s P_{tt}^2 \quad (A3)$$

REFERENCES

1. Feldhuhn, R. H.: Heat Transfer from a Turbulent Boundary Layer on a Porous Hemisphere. AIAA Paper 76-119, 1976.
2. Marvin, Joseph G.; and Pope, Ronald B.: Laminar Convective Heating and Ablation in the Mars Atmosphere. AIAA Journal, vol. 5, no. 2, 1967, pp. 240-248.
3. Yoshikawa, Kenneth K.: Linearized Theory of Stagnation Point Heat and Mass Transfer at Hypersonic Speeds. NASA TN D-5246, 1969.
4. Howe, John T.; and Viegas, John R.: Solutions of the Ionized Radiating Shock Layer, Including Reabsorption and Foreign Species Effects, and Stagnation Region Heat Transfer. NASA TR R-159, 1963.
5. Marvin, Joseph G.; and Sheaffer, Yvonne S.: A Method for Solving the Nonsimilar Laminar Boundary-Layer Equations Including Foreign Gas Injection. NASA TN D-5516, 1969.
6. Traci, R. M.; and Wilcox, D. C.: Analytical Study of Freestream Turbulence Effects on Stagnation Point Flow and Heat Transfer. AIAA 7th Fluid and Plasma Dynamics Conference, Palo Alto, Calif., June 17-19, 1974.
7. Wilcox, D. C.: Turbulence-Model Transition Predictions for Blunt-Body Flows. Interim Scientific Report, DCW-R-03-01, AFOSR-TR-74-1714, 1974.
8. Wilcox, David C.: Combined Effects of Freestream Turbulence and Mass Addition on Blunt-Body Heating and Transition. Interim Scientific Report, DCW-R-11-02, 1977.
9. Reda, D. C.; and Leverance, R. A.: Boundary-Layer Transition Experiments on Pre-Ablated Graphite Nostips in a Hyperballistics Range. NSWC/WOL/TR 76-71, 1976.
10. Prandtl, Ludwig; and Tietjens, O. G.: Applied Hydro and Aeromechanics, McGraw-Hill Book Company, Inc., 1934.
11. Stainback, Calvin P.; Wagner, Richard D.; Owen, Kevin F.; and Horstman, Clifford C.: Experimental Studies of Hypersonic Boundary Layer Transition and Effects of Wind-Tunnel Disturbances. NASA TN D-7453, 1974.

TABLE 1.- MASS ADDITION RATE DISTRIBUTION, HEMISPHERICAL MODEL 1

Run \dot{m}_0	77H1 3.068	78H1 2.949	79H1 2.973	80H1 3.001	81H1 3.016	82H1 3.015	83H1 3.020	84H1 3.006	88H1 6.147	89H1 6.213	95H1 5.971
s=0.00	0.0021	0.0104	0.0434	0.0550	0.0713	0.0871	0.109	0.120	0.0022	0.0258	0.0387
.85	.0026	.0128	.0530	.0671	.0869	.106	.133	.147	.0031	.0317	.0475
1.68	.0030	.0143	.0587	.0744	.0964	.118	.147	.163	.0039	.0356	.0531
2.51	.0039	.0160	.0641	.0810	.105	.128	.160	.176	.0067	.0409	.0598
3.35	.0046	.0169	.0664	.0838	.108	.132	.165	.182	.0084	.0436	.0631
4.19	.0049	.0176	.0678	.0854	.110	.134	.168	.185	.0104	.0462	.0660
5.03	.0058	.0182	.0684	.0861	.111	.135	.168	.186	.0129	.0487	.0685
5.87	.0063	.0186	.0682	.0856	.110	.134	.167	.184	.0158	.0511	.0705
6.70	.0068	.0190	.0678	.0849	.109	.132	.165	.182	.0180	.0528	.0720
7.54	.0074	.0193	.0674	.0843	.108	.131	.163	.180	.0202	.0545	.0734
8.38	.0078	.0195	.0668	.0835	.107	.129	.161	.177	.0219	.0556	.0742
9.22	.0082	.0200	.0673	.0840	.107	.130	.161	.178	.0237	.0575	.0761
10.06	.0085	.0200	.0666	.0830	.106	.128	.159	.176	.0247	.0580	.0763
10.90	.0086	.0199	.0659	.0820	.105	.127	.157	.173	.0254	.0581	.0762
11.73	.0089	.0202	.0662	.0823	.105	.127	.157	.173	.0267	.0594	.0775
12.57	.0090	.0201	.0653	.0812	.104	.125	.155	.171	.0270	.0593	.0771

Run \dot{m}_0	91H1 6.248	92H1 6.268	93H1 6.127	94H1 5.891	99H1 13.378	100H1 12.993	101H1 12.710	102H1 13.197	103H1 12.824	104H1 12.352
s=0.00	0.0569	0.0792	0.0891	0.111	-0.0127	0.0048	0.0218	0.0372	0.0550	0.934
.85	.0695	.0967	.109	.135	-.0141	.0072	.0279	.0467	.0684	.115
1.68	.0775	.108	.121	.150	-.0137	.0099	.0328	.0537	.0776	.129
2.51	.0862	.119	.133	.165	-.0048	.0206	.0453	.0681	.0937	.149
3.35	.0902	.124	.139	.171	.0012	.0275	.0528	.0764	.103	.159
4.19	.0935	.127	.143	.176	.0093	.0359	.0616	.0858	.112	.169
5.03	.0960	.130	.145	.178	.0195	.0461	.0716	.0961	.122	.179
5.87	.0976	.131	.146	.178	.0317	.0579	.0829	.107	.133	.188
6.70	.0987	.132	.147	.178	.0414	.0671	.0917	.116	.141	.195
7.54	.0997	.132	.147	.178	.0511	.0764	.101	.125	.149	.202
8.38	.100	.132	.147	.178	.0582	.0832	.107	.131	.155	.206
9.22	.102	.134	.149	.180	.0658	.0907	.114	.139	.162	.213
10.06	.102	.133	.148	.178	.0704	.0950	.118	.142	.165	.215
10.90	.101	.132	.146	.177	.0737	.0979	.121	.145	.167	.216
11.73	.103	.134	.148	.178	.0788	.103	.126	.150	.172	.221
12.57	.102	.132	.146	.176	.0809	.105	.127	.151	.173	.220

TABLE 2.- MASS ADDITION RATE DISTRIBUTION, HEMISPHERICAL MODEL 2

Run \dot{m}_m	60H2 1.563	70H2 1.477	90H2 1.524	61H2 1.563	67H2 1.522	62H2 1.559	63H2 1.569	64H2 1.500	87H2 1.531	71H2 2.956	91H2 3.004	75H2 3.076	68H2 2.926	77H2 3.195
$\alpha=0.00$	-0.0005	0.0028	0.0038	0.0129	0.0207	0.0267	0.0394	0.0564	0.104	0.0013	0.0072	0.0122	0.0197	0.0265
.85	-.0009	.0050	.0067	.0227	.0365	.0472	.0695	.0996	.183	.0022	.0127	.0215	.0347	.0467
1.68	-.0008	.0047	.0063	.0213	.0341	.0441	.0649	.0930	.171	.0022	.0120	.0202	.0326	.0437
2.51	-.0013	.0076	.0101	.0342	.0549	.0709	.104	.149	.275	.0036	.0194	.0326	.0524	.0703
3.35	-.0013	.0088	.0115	.0389	.0623	.0805	.118	.169	.312	.0046	.0225	.0375	.0600	.0802
4.19	-.0013	.0095	.0123	.0412	.0661	.0853	.125	.180	.330	.0052	.0242	.0400	.0638	.0852
5.03	-.0012	.0097	.0127	.0422	.0675	.0870	.128	.183	.336	.0059	.0252	.0414	.0657	.0875
5.87	-.0011	.0104	.0135	.0445	.0713	.0919	.133	.193	.355	.0069	.0273	.0443	.0699	.0929
6.70	-.0010	.0109	.0141	.0463	.0739	.0953	.140	.200	.367	.0077	.0288	.0464	.0729	.0967
7.54	-.0009	.0110	.0143	.0465	.0741	.0954	.140	.200	.367	.0083	.0293	.0469	.0734	.0972
8.38	-.0008	.0111	.0144	.0466	.0742	.0955	.140	.200	.367	.0086	.0297	.0473	.0738	.0976
9.22	-.0008	.0109	.0141	.0466	.0730	.0939	.138	.197	.361	.0084	.0291	.0465	.0725	.0959
10.06	-.0006	.0107	.0138	.0467	.0707	.0909	.133	.190	.349	.0088	.0289	.0456	.0707	.0934
10.90	-.0005	.0114	.0147	.0468	.0745	.0958	.140	.200	.368	.0099	.0310	.0486	.0751	.0988
11.73	-.0004	.0111	.0142	.0453	.0721	.0926	.133	.194	.356	.0097	.0301	.0471	.0727	.0957
12.57	-.0003	.0111	.0143	.0454	.0722	.0927	.133	.194	.356	.0099	.0303	.0474	.0730	.0959
Run \dot{m}_m	79H2 3.217	65H2 2.985	82H2 2.966	85H2 2.996	88H2 3.025	72H2 5.966	76H2 6.204	92H2 5.913	69H2 5.879	78H2 6.406	80H2 6.434	66H2 5.947	83H2 5.742	89H2 6.258
$\alpha=0.00$	0.0402	0.0542	0.0674	0.0821	0.0976	-0.0053	0.0067	0.0089	0.0137	0.0206	0.0341	0.0501	0.0606	0.0913
.85	.0710	.0957	.119	.145	.172	-.0076	.0116	.0155	.0241	.0363	.0600	.0882	.107	.161
1.68	.0664	.0894	.111	.135	.161	-.0066	.0114	.0151	.0230	.0344	.0566	.0829	.100	.151
2.51	.107	.144	.179	.217	.259	-.0102	.0187	.0246	.0374	.0556	.0912	.134	.162	.243
3.35	.122	.164	.203	.247	.294	-.0093	.0234	.0301	.0446	.0653	.106	.154	.185	.277
4.19	.129	.174	.216	.262	.311	-.0086	.0260	.0332	.0485	.0704	.113	.164	.197	.295
5.03	.132	.177	.220	.267	.318	-.0062	.0291	.0363	.0520	.0743	.118	.170	.204	.303
5.87	.140	.188	.233	.283	.336	-.0039	.0333	.0410	.0575	.0810	.127	.181	.217	.322
6.70	.145	.195	.241	.293	.348	-.0018	.0367	.0446	.0616	.0860	.133	.190	.227	.335
7.54	.146	.195	.242	.293	.348	.0003	.0388	.0468	.0638	.0882	.136	.192	.229	.338
8.38	.146	.196	.242	.294	.349	.0019	.0404	.0484	.0654	.0897	.137	.194	.231	.339
9.22	.144	.192	.238	.289	.343	.0017	.0395	.0473	.0641	.0880	.135	.190	.227	.333
10.06	.140	.187	.231	.280	.332	.0043	.0408	.0484	.0646	.0877	.133	.186	.222	.325
10.90	.147	.197	.244	.295	.350	.0069	.0454	.0533	.0704	.0947	.142	.199	.236	.344
11.73	.143	.191	.236	.285	.339	.0073	.0445	.0523	.0687	.0922	.138	.193	.229	.333
12.57	.143	.191	.236	.286	.339	.0083	.0455	.0532	.0696	.0932	.139	.194	.229	.334

TABLE 3.- MASS ADDITION RATE DISTRIBUTION, SPHERICAL SEGMENT MODEL 1

Run \dot{m}_m	15SS1 3.196	14SS1 3.308	17SS1 3.049	31SS1 3.115	18SS1 3.180	32SS1 3.072	33SS1 3.073	20SS1 6.250	27SS1 6.182
s=0.00	-0.0086	0.0034	0.0277	0.0611	0.0909	0.168	0.267	-0.0068	0.0590
.89	-.0084	.0034	.0278	.0614	.0912	.189	.268	-.0056	.0601
1.78	-.0081	.0039	.0270	.0593	.0882	.182	.259	-.0055	.0581
2.67	-.0077	.0039	.0274	.0597	.0885	.183	.259	-.0040	.0596
3.56	-.0074	.0044	.0271	.0589	.0872	.180	.255	-.0030	.0595
4.45	-.0071	.0044	.0274	.0592	.0875	.190	.255	-.0019	.0606
4.90	-.0069	.0049	.0276	.0594	.0877	.180	.255	-.0011	.0614
5.33	-.0067	.0049	.0278	.0596	.0879	.180	.256	-.0003	.0622
5.79	-.0066	.0049	.0279	.0598	.0881	.181	.258	.0004	.0629
6.22	-.0065	.0049	.0274	.0587	.0865	.177	.251	.0003	.0617
6.68	-.0062	.0054	.0277	.0589	.0867	.178	.252	.0014	.0628
7.11	-.0060	.0054	.0273	.0579	.0853	.175	.247	.0017	.0620
7.57	-.0057	.0059	.0275	.0582	.0856	.175	.247	.0028	.0631
8.00	-.0054	.0059	.0278	.0585	.0858	.175	.248	.0040	.0642
8.26	-.0053	.0059	.0274	.0575	.0844	.172	.243	.0042	.0634

Run \dot{m}_m	21SS1 6.374	28SS1 6.286	22SS1 6.065	30SS1 6.097	35SS1 12.642	38SS1 12.529	39SS1 11.087	40SS1 12.363
s=0.00	0.108	0.162	0.217	0.292	0.0162	0.146	0.231	0.314
.89	.109	.163	.218	.293	.0207	.150	.235	.319
1.78	.105	.158	.211	.284	.0198	.145	.227	.308
2.67	.107	.159	.212	.285	.0259	.151	.232	.314
3.56	.106	.158	.209	.281	.0292	.152	.232	.312
4.45	.107	.159	.211	.282	.0337	.157	.236	.317
4.90	.108	.159	.211	.283	.0368	.160	.238	.320
5.33	.109	.160	.212	.284	.0398	.163	.241	.323
5.79	.109	.161	.213	.285	.0428	.166	.244	.326
6.22	.107	.158	.209	.279	.0417	.162	.239	.320
6.68	.109	.159	.210	.281	.0462	.167	.243	.325
7.11	.107	.157	.207	.276	.0465	.165	.240	.320
7.57	.108	.158	.208	.277	.0511	.169	.244	.324
8.00	.109	.159	.209	.278	.0556	.174	.248	.329
8.26	.107	.156	.205	.273	.0559	.172	.245	.324

TABLE 4.- MASS ADDITION RATE DISTRIBUTION, SPHERICAL SEGMENT MODEL 2

Run \bar{m}_n	4SS2 1.616	97SS2 1.675	3SS2 1.552	21SS2 1.420	6SS2 1.630	20SS2 1.442	100SS2 1.494	10SS2 3.070	11SS2 2.956	8SS2 3.054	98SS2 3.176	24SS2 2.813	9SS2 3.032	12SS2 3.075	13SS2 3.192
s=0.00	-0.0018	0.0155	0.0374	0.0730	0.140	0.263	0.623	-0.0065	0.0095	0.0191	0.0340	0.0509	0.0878	0.117	0.160
.89	-.0015	.0117	.0306	.0626	.119	.225	.534	-.0054	.0094	.0166	.0293	.0439	.0755	.101	.138
1.78	-.0017	.0133	.0349	.0713	.135	.257	.608	-.0062	.0095	.0189	.0334	.0500	.0859	.115	.157
2.67	-.0021	.0166	.0434	.0887	.168	.319	.756	-.0075	.0120	.0236	.0417	.0623	.107	.143	.195
3.56	-.0021	.0166	.0434	.0887	.168	.319	.756	-.0074	.0121	.0237	.0418	.0624	.107	.143	.195
4.45	-.0019	.0182	.0471	.0960	.182	.496	.816	-.0069	.0142	.0267	.0462	.0684	.117	.155	.212
4.90	-.0020	.0174	.0452	.0923	.175	.478	.786	-.0071	.0132	.0252	.0440	.0655	.112	.149	.203
5.33	-.0021	.0191	.0496	.101	.192	.522	.860	-.0075	.0147	.0278	.0484	.0718	.123	.163	.223
5.79	-.0020	.0189	.0488	.0995	.188	.514	.846	-.0073	.0146	.0275	.0477	.0708	.121	.160	.219
6.22	-.0020	.0189	.0489	.0995	.188	.514	.846	-.0071	.0148	.0277	.0479	.0709	.121	.161	.219
6.68	-.0021	.0209	.0540	.110	.208	.568	.935	-.0077	.0165	.0308	.0532	.0786	.134	.177	.243
7.11	-.0018	.0187	.0482	.0979	.185	.505	.831	-.0063	.0151	.0278	.0476	.0703	.119	.158	.216
7.57	-.0018	.0183	.0472	.0961	.182	.496	.816	-.0064	.0147	.0272	.0467	.0689	.117	.155	.212
8.00	-.0016	.0168	.0430	.0874	.165	.497	.742	-.0058	.0136	.0249	.0426	.0628	.107	.142	.193
8.25	-.0015	.0164	.0422	.0857	.162	.442	.727	-.0052	.0135	.0246	.0420	.0618	.105	.139	.189

Run \bar{m}_n	14SS2 3.114	15SS2 3.213	17SS2 2.972	101SS2 2.941	104SS2 3.068	96SS2 6.140	27SS2 6.003	99SS2 6.254	25SS2 5.779	26SS2 5.848	102SS2 5.953	103SS2 6.128	106SS2 6.232	105SS2 6.149
s=0.00	0.210	0.312	0.394	0.515	0.624	-0.0242	0.0186	0.0222	0.0921	0.167	0.274	0.371	0.447	0.539
.89	.180	.268	.338	.442	.535	-.0198	.0169	.0200	.0799	.144	.236	.319	.384	.463
1.78	.205	.305	.384	.503	.610	-.0226	.0191	.0227	.0909	.164	.268	.363	.438	.527
2.67	.255	.379	.478	.626	.758	-.0276	.0243	.0288	.114	.204	.335	.452	.545	.656
3.56	.255	.379	.478	.626	.758	-.0276	.0247	.0292	.114	.205	.334	.453	.545	.656
4.45	.276	.410	.517	.676	.819	-.0250	.0310	.0359	.127	.225	.365	.493	.592	.712
4.90	.266	.395	.498	.651	.789	-.0259	.0281	.0327	.121	.215	.350	.475	.569	.685
5.33	.291	.432	.545	.713	.864	-.0275	.0315	.0366	.133	.236	.384	.518	.623	.750
5.79	.286	.425	.536	.701	.849	-.0264	.0316	.0366	.131	.233	.378	.510	.613	.738
6.22	.287	.425	.536	.708	.849	-.0256	.0325	.0375	.132	.234	.379	.511	.614	.739
6.68	.317	.470	.593	.775	.939	-.0276	.0366	.0421	.147	.259	.419	.565	.679	.817
7.11	.282	.418	.527	.689	.828	-.0229	.0342	.0391	.132	.232	.374	.504	.606	.728
7.57	.277	.410	.518	.677	.820	-.0230	.0331	.0379	.129	.227	.367	.495	.594	.714
8.00	.252	.373	.471	.616	.745	-.0200	.0308	.0353	.118	.208	.335	.451	.541	.650
8.26	.247	.366	.461	.603	.731	-.0189	.0310	.0353	.117	.204	.329	.442	.531	.638

TABLE 5.- MASS ADDITION RATE DISTRIBUTION, CONICAL MODEL 1

Run \bar{t}_m	43C1 3.392	52C1 3.083	44C1 3.374	45C1 3.016	46C1 3.127	47C1 3.128	48C1 2.960	49C1 3.157	50C1 3.044	51C1 3.025	53C1 6.084	54C1 6.031	63C1 6.222
s=0.00	0.000	0.000	0.000	0.000	0.000	0.000	0.000	0.000	0.000	0.000	0.000	0.000	0.000
.94	.000	.000	.000	.000	.000	.000	.000	.000	.000	.000	.000	.000	.000
1.96	.000	.000	.000	.000	.000	.000	.000	.000	.000	.000	.000	.000	.000
2.97	.000	.000	.000	.000	.000	.000	.000	.000	.000	.000	.000	.000	.000
3.99	-.0006	.0013	.0015	.0030	.0105	.0137	.0176	.0215	.0254	.0298	-.0022	.0004	.0036
5.00	-.0015	.0036	.0042	.0081	.0281	.0372	.0474	.0582	.0689	.0792	-.0057	.0016	.0130
5.51	-.0022	.0052	.0062	.0118	.0411	.0538	.0694	.0846	.100	.116	-.0078	.0025	.0148
6.02	-.0029	.0074	.0086	.0166	.0572	.0753	.0963	.118	.139	.161	-.0108	.0038	.0208
6.53	-.0035	.0090	.0105	.0201	.0694	.0914	.117	.143	.169	.195	-.0132	.0048	.0255
7.04	-.0042	.0109	.0127	.0244	.0836	.111	.141	.173	.204	.236	-.0156	.0059	.0309
7.54	-.0044	.0117	.0136	.0261	.0895	.118	.151	.184	.218	.252	-.0166	.0066	.0333
8.05	-.0045	.0124	.0145	.0275	.0944	.124	.159	.194	.230	.266	-.0171	.0072	.0354
8.56	-.0045	.0127	.0148	.0281	.0963	.127	.162	.198	.234	.270	-.0171	.0077	.0364
9.07	-.0046	.0129	.0151	.0286	.0978	.129	.165	.201	.238	.275	-.0171	.0079	.0370
9.32	-.0045	.0129	.0150	.0284	.0968	.128	.163	.200	.236	.273	-.0171	.0079	.0368
Run \bar{t}_m	57C1 6.502	64C1 6.243	58C1 6.247	59C1 6.191	60C1 6.157	61C1 6.258	62C1 6.320	65C1 5.949	66C1 6.166	69C1 12.559	70C1 12.654	71C1 12.854	73C1 13.024
s=0.00	0.000	0.000	0.000	0.000	0.000	0.000	0.000	0.000	0.000	0.000	0.000	0.000	0.000
.94	.000	.000	.000	.000	.000	.000	.000	.000	.000	.000	.000	.000	.000
1.96	.000	.000	.000	.000	.000	.000	.000	.000	.000	.000	.000	.000	.000
2.97	.000	.000	.000	.000	.000	.000	.000	.000	.000	.000	.000	.000	.000
3.99	.0078	.0103	.0132	.0171	.0200	.0249	.0279	.0347	.0396	-.0024	.0079	.0177	.0328
5.00	.0213	.0284	.0362	.0460	.0543	.0665	.0748	.0929	.106	-.0050	.0226	.0488	.0890
5.51	.0312	.0416	.0533	.0670	.0792	.0973	.109	.135	.155	-.0064	.0338	.0719	.131
6.02	.0437	.0582	.0743	.0934	.110	.136	.152	.188	.215	-.0078	.0481	.101	.183
6.53	.0533	.0704	.0905	.113	.135	.165	.184	.228	.251	-.0087	.0592	.123	.223
7.04	.0645	.0856	.109	.137	.162	.199	.223	.276	.316	-.0101	.0719	.150	.269
7.54	.0689	.0914	.117	.147	.174	.213	.238	.295	.337	-.0096	.0730	.161	.289
8.05	.0729	.0968	.124	.155	.183	.225	.251	.312	.356	-.0090	.0833	.171	.305
8.56	.0748	.0988	.126	.158	.187	.229	.256	.317	.362	-.0074	.0865	.176	.313
9.07	.0758	.100	.128	.161	.190	.233	.260	.323	.369	-.0075	.0880	.179	.318
9.32	.0753	.100	.127	.159	.189	.231	.258	.320	.365	-.0068	.0877	.177	.315

TABLE 6.- MASS ADDITION RATE DISTRIBUTION, CONICAL MODEL 2

Run \dot{m}_m	36C2 1.513	29C2 1.737	30C2 1.455	58C2 1.585	57C2 1.560	51C2 1.567	43C2 3.072	42C2 3.059	41C2 2.885	40C2 2.936
$s=0.00$	-0.0010	0.0347	0.0876	0.196	0.473	0.706	-0.0038	0.0187	0.115	0.185
.64	-.0009	.0337	.0849	.189	.458	.683	-.0033	.0185	.112	.180
1.27	-.0011	.0461	.116	.259	.626	.934	-.0041	.0256	.153	.246
1.91	-.0008	.0360	.0907	.202	.489	.729	-.0030	.0202	.119	.192
2.54	-.0008	.0407	.102	.227	.550	.820	-.0030	.0231	.135	.217
3.18	-.0007	.0327	.0822	.183	.443	.661	-.0026	.0184	.109	.174
3.81	-.0007	.0338	.0851	.190	.458	.683	-.0027	.0190	.112	.180
4.45	-.0007	.0315	.0794	.177	.428	.638	-.0026	.0177	.105	.168
5.08	-.0008	.0338	.0850	.190	.458	.683	-.0028	.0190	.112	.180
5.72	-.0009	.0395	.0993	.221	.535	.797	-.0032	.0222	.131	.210
6.35	-.0007	.0293	.0737	.164	.397	.592	-.0024	.0164	.0971	.157
6.99	-.0008	.0350	.0879	.196	.473	.704	-.0028	.0197	.116	.186
7.62	-.0008	.0361	.0908	.202	.489	.729	-.0029	.0203	.120	.192
8.26	-.0008	.0373	.0936	.209	.504	.752	-.0028	.0211	.124	.199
8.89	-.0007	.0350	.0880	.196	.473	.706	-.0026	.0199	.116	.187
9.53	-.0008	.0396	.0993	.221	.535	.797	-.0028	.0225	.131	.211
Run \dot{m}_m	39C2 2.806	55C2 3.139	50C2 3.170	44C2 5.964	48C2 6.080	47C2 6.004	46C2 5.625	45C2 5.918	53C2 6.116	52C2 5.978
$s=0.00$	0.262	0.434	0.695	-0.0132	0.0181	0.149	0.276	0.365	0.425	0.708
.64	.254	.421	.673	-.0112	.0191	.146	.269	.356	.414	.687
1.27	.348	.575	.920	-.0142	.0274	.201	.369	.487	.567	.940
1.91	.271	.466	.718	-.0103	.0220	.158	.289	.381	.443	.735
2.54	.306	.506	.808	-.0098	.0264	.179	.326	.430	.500	.828
3.18	.246	.407	.651	-.0088	.0205	.143	.262	.346	.402	.666
3.81	.255	.421	.673	-.0093	.0215	.148	.271	.358	.416	.689
4.45	.238	.393	.628	-.0068	.0196	.138	.252	.334	.388	.643
5.08	.255	.421	.673	-.0093	.0210	.148	.271	.358	.416	.689
5.72	.297	.491	.786	-.0108	.0249	.173	.316	.417	.485	.804
6.35	.221	.365	.583	-.0083	.0181	.128	.235	.310	.360	.597
6.99	.263	.435	.696	-.0093	.0220	.153	.280	.370	.430	.712
7.62	.271	.449	.718	-.0098	.0230	.158	.289	.381	.454	.735
8.26	.280	.463	.741	-.0098	.0240	.163	.299	.394	.458	.758
8.89	.264	.435	.696	-.0083	.0230	.154	.281	.371	.431	.713
9.53	.297	.491	.786	-.0093	.0259	.174	.317	.419	.481	.805

BLANK PAGE

**CALORIMETER
DETAIL**

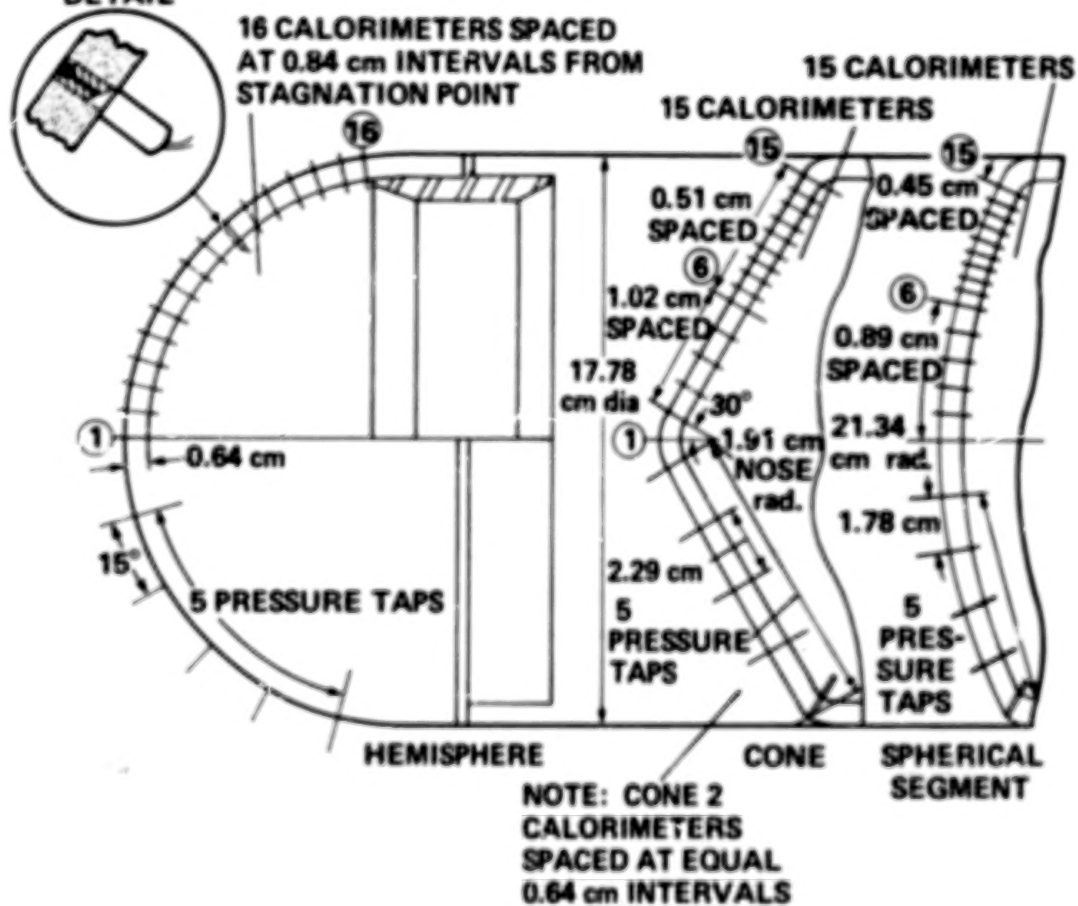


Figure 1.- Porous model headers.

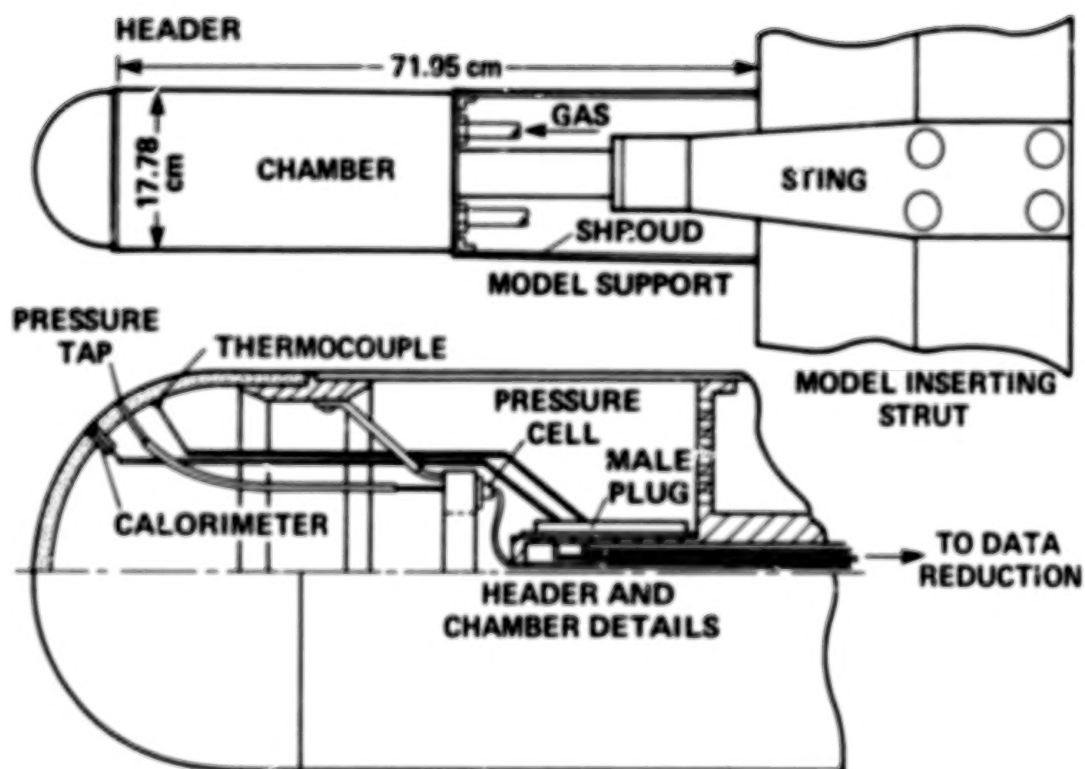


Figure 2.- Model support and details.

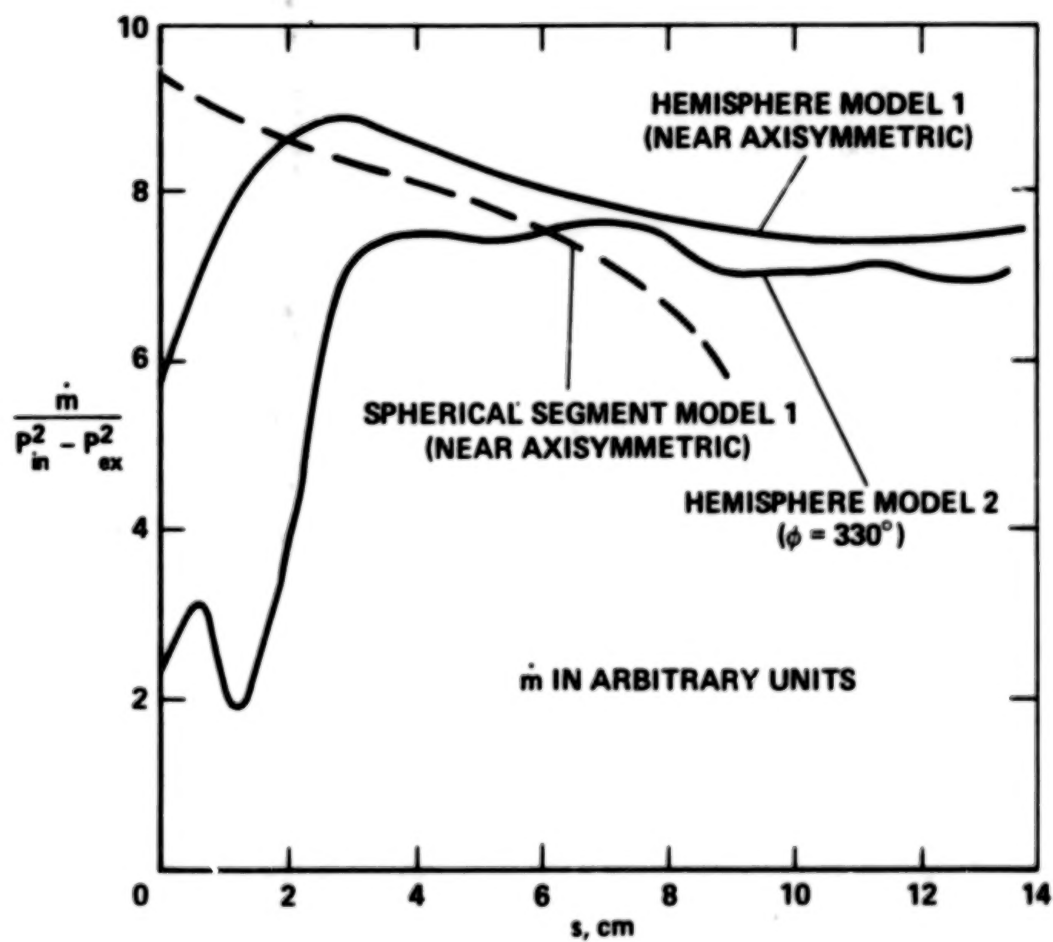
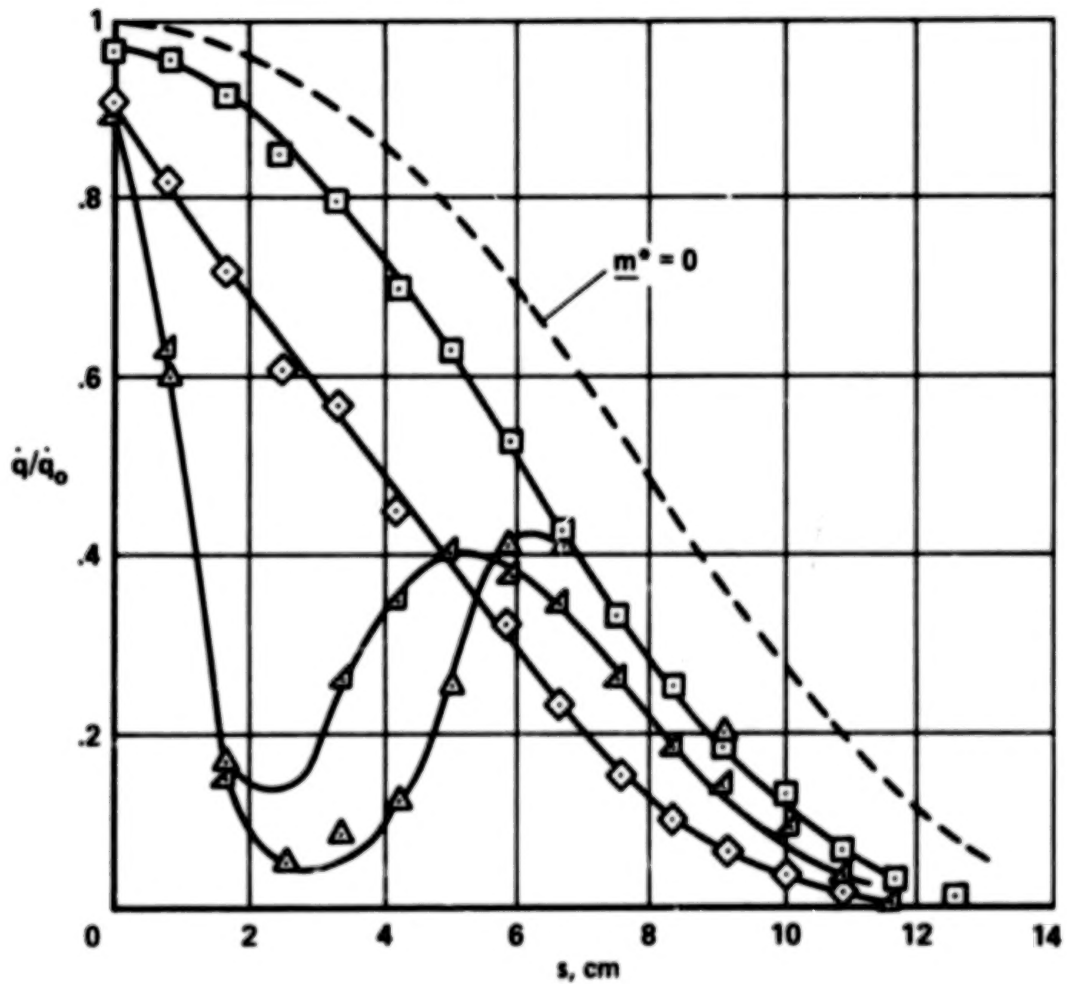


Figure 3.- Typical variation of mass flow rate with radial distance s with constant pressure drop across headers.

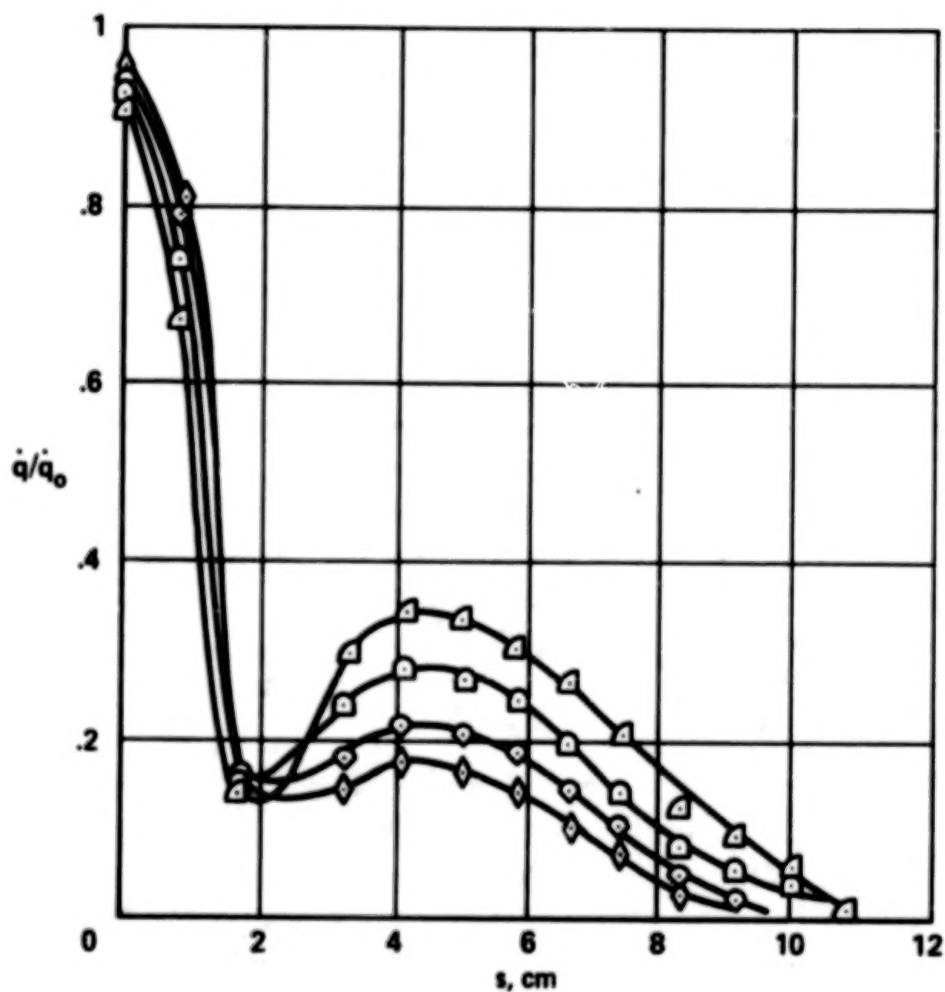
RUN	Re_D	T_{tt}	\dot{q}_0	\underline{m}^*
□ 77H1	1.11×10^6	782	9.80	0.003
◇ 78H1	1.05×10^6	793	9.83	0.007
△ 79H1	1.07×10^6	788	9.77	0.022
▴ 80H1	1.10×10^6	775	9.51	0.027



(a) $P_{tt} = 276 \text{ N/cm}^2$ (400 psi), $0.003 < \underline{m}^* < 0.027$.

Figure 4.- Heat transfer distribution over hemispherical model 1.

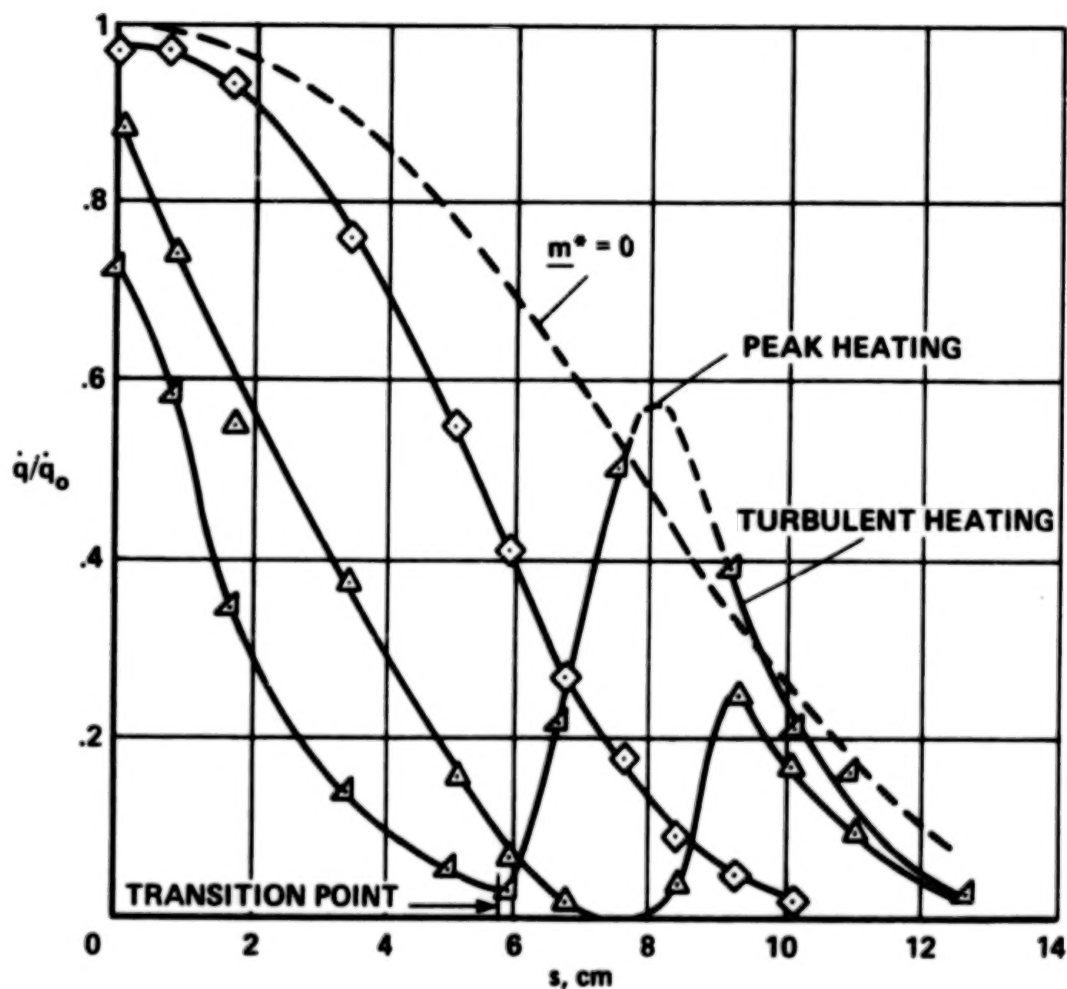
	RUN	Re_D	T_{tt}	\dot{q}_0	\underline{m}^*
\triangle	81H1	1.11×10^6	769	9.36	0.034
\square	82H1	1.11×10^6	768	9.47	0.041
\diamond	83H1	1.12×10^6	767	9.36	0.051
\diamond	84H1	1.10×10^6	773	9.60	0.057



(b) $P_{tt} = 276 \text{ N/cm}^2$ (400 psi), $0.034 < \underline{m}^* < 0.057$.

Figure 4.- Continued.

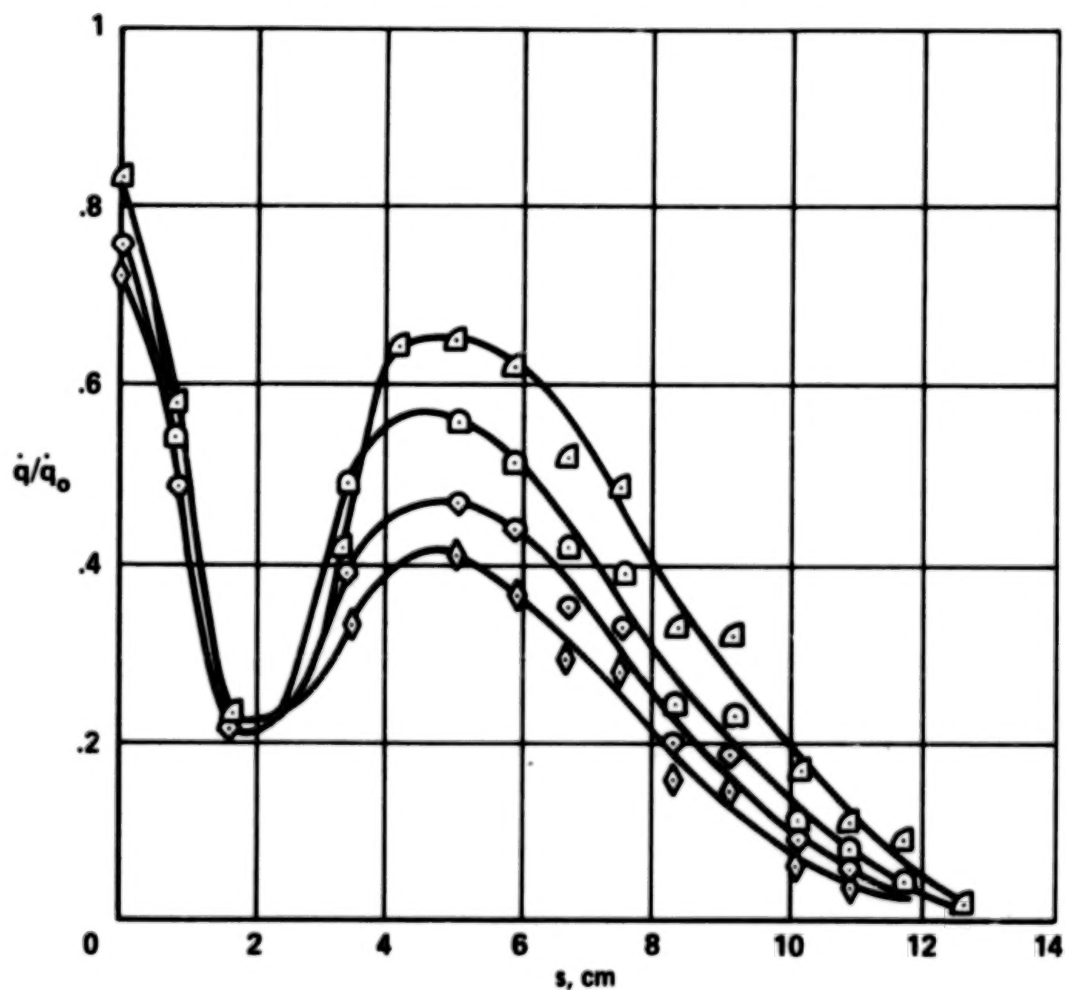
RUN	Re_D	T_{tt}	\dot{q}_0	\underline{m}^*
◇ 88H1	2.29×10^6	761	13.13	0.004
△ 89H1	2.37×10^6	748	12.94	0.010
△ 95H1	2.12×10^6	797	14.16	0.013



(c) $P_{tt} = 552 \text{ N/cm}^2$ (800 psi), $0.004 < \underline{m}^* < 0.013$.

Figure 4.- Continued.

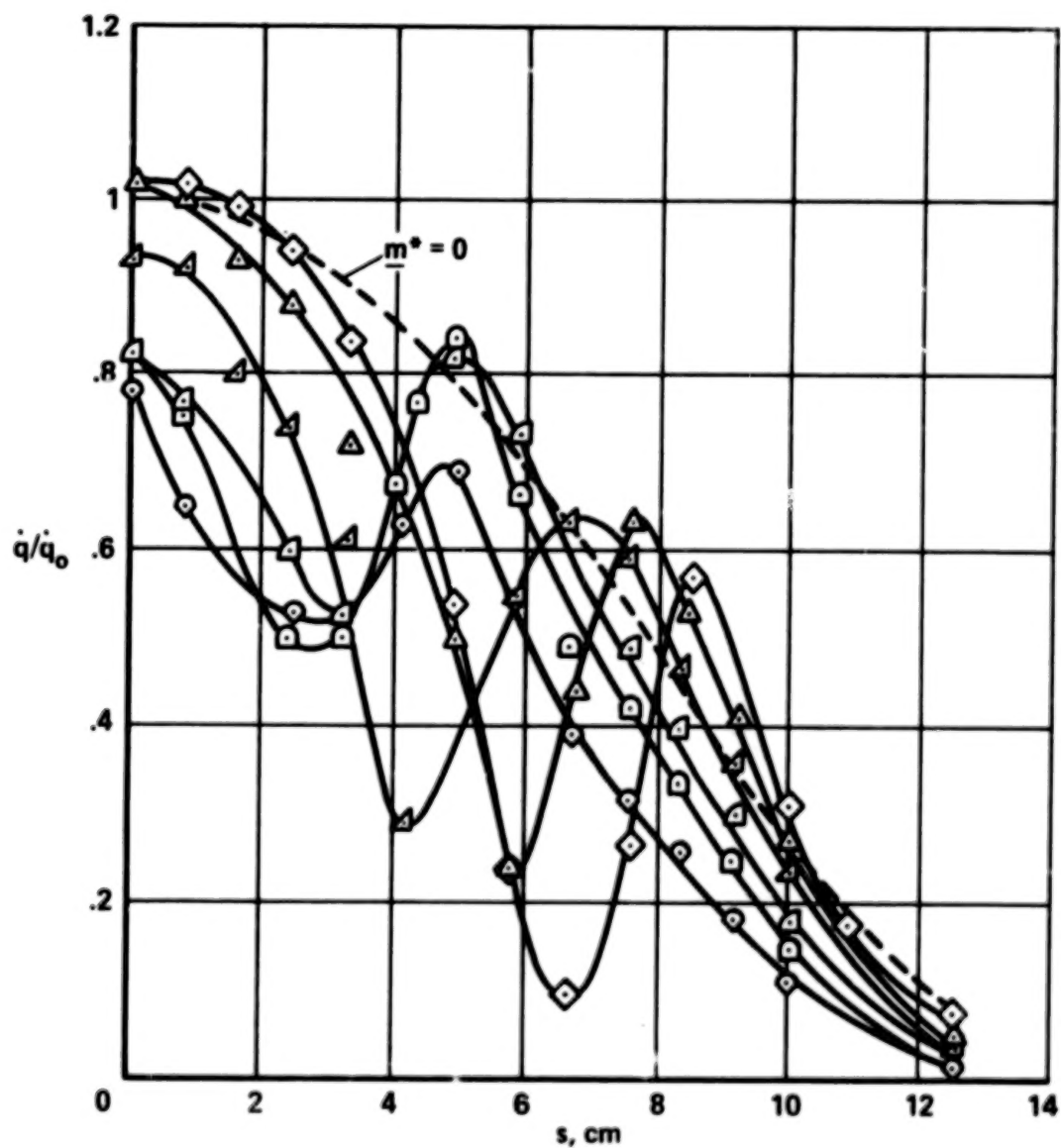
	RUN	Re_D	T_{tt}	\dot{q}_o	\underline{m}^*
\triangle	91H1	2.40×10^6	740	12.50	0.016
\square	92H1	2.42×10^6	737	12.45	0.021
\diamond	93H1	2.26×10^6	767	13.54	0.024
\diamond	94H1	2.01×10^6	815	14.96	0.030



(d) $P_{tt} = 552 \text{ N/cm}^2$ (800 psi), $0.016 < \underline{m}^* < 0.030$.

Figure 4.- Continued.

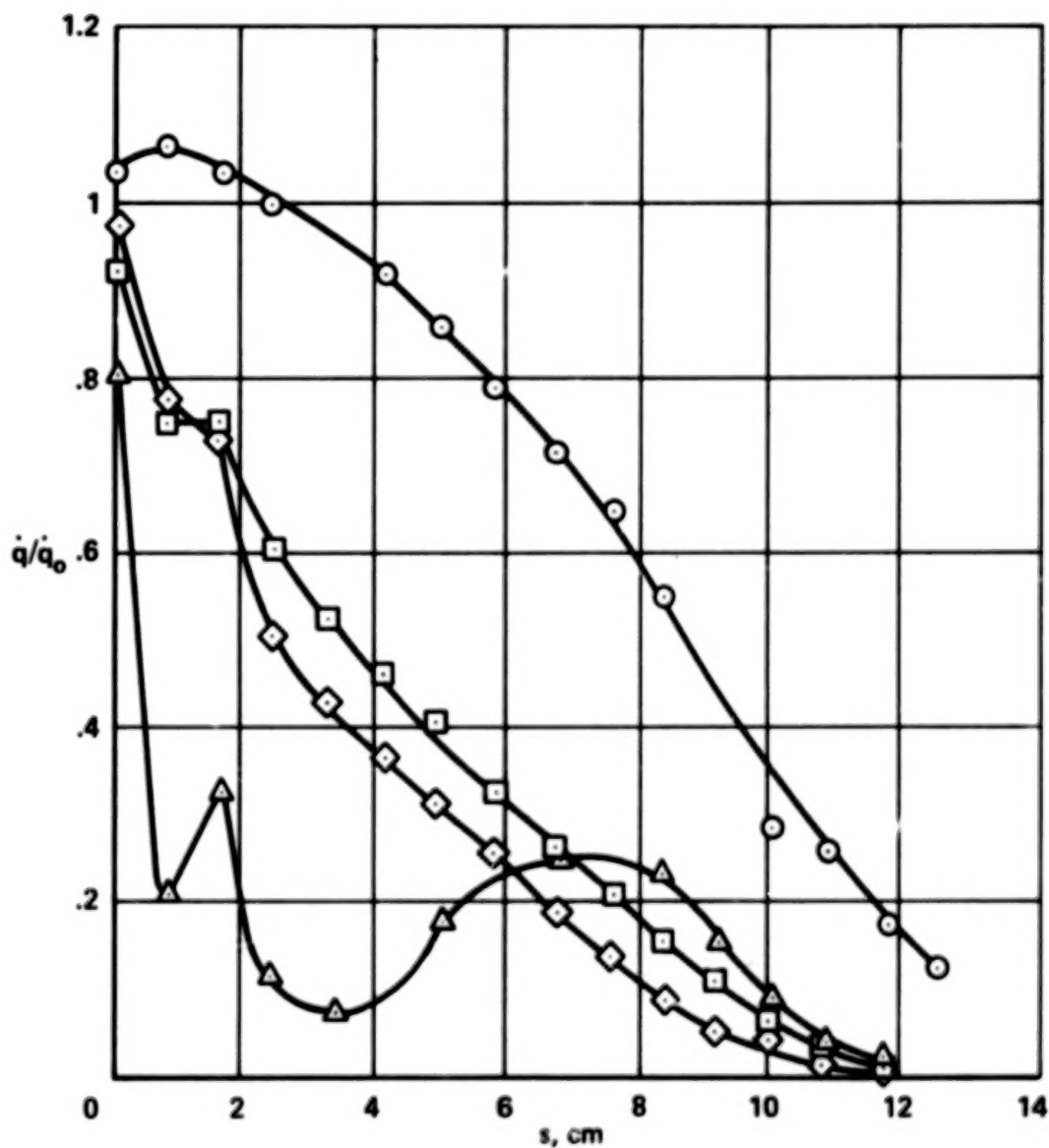
	RUN	Re_D	T_{tt}	\dot{q}_0	\underline{m}^*
◇	99H1	5.66×10^6	674	14.19	0.006
△	100H1	5.23×10^6	707	16.31	0.008
▵	101H1	4.96×10^6	728	17.09	0.010
▹	102H1	5.38×10^6	699	16.12	0.011
□	103H1	5.06×10^6	721	17.01	0.013
◇	104H1	4.80×10^6	733	17.30	0.018



(e) $P_{tt} = 1103 \text{ N/cm}^2$ (1600 psi), $0.006 < \underline{m}^* < 0.018$.

Figure 4.- Concluded.

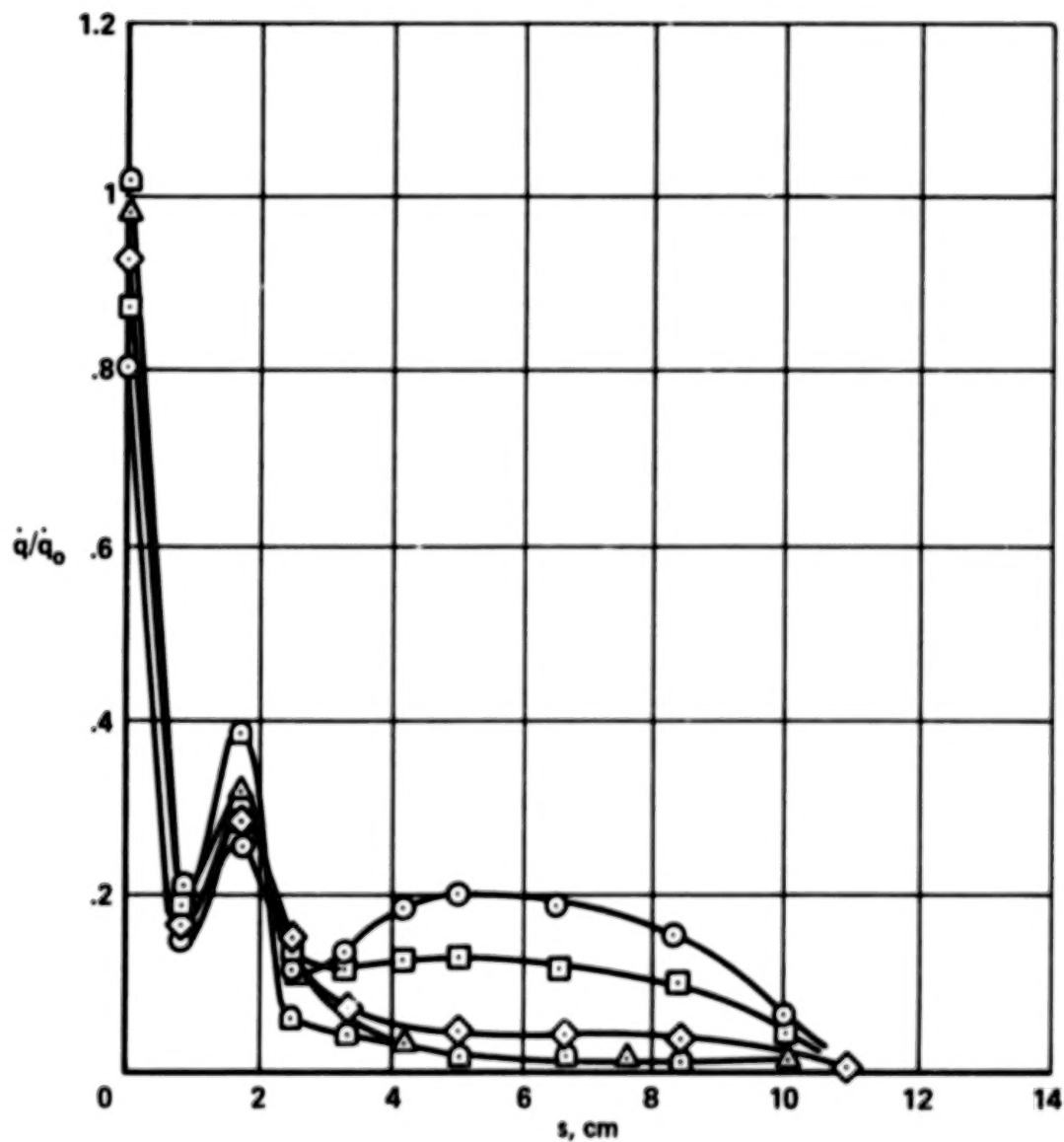
RUN	Re_D	T_{tt}	\dot{q}_0	\underline{m}^*
○ 60H2	0.61×10^6	732	6.19	-0.000
□ 70H2	0.53×10^6	797	7.17	0.008
◇ 90H2	0.56×10^6	768	6.78	0.003
△ 61H2	0.61×10^6	733	6.12	0.029



(a) $P_{tt} = 138 \text{ N/cm}^2$ (200 psi), $0 < \underline{m}^* < 0.029$.

Figure 5.- Heat transfer distribution over hemispherical model 2.

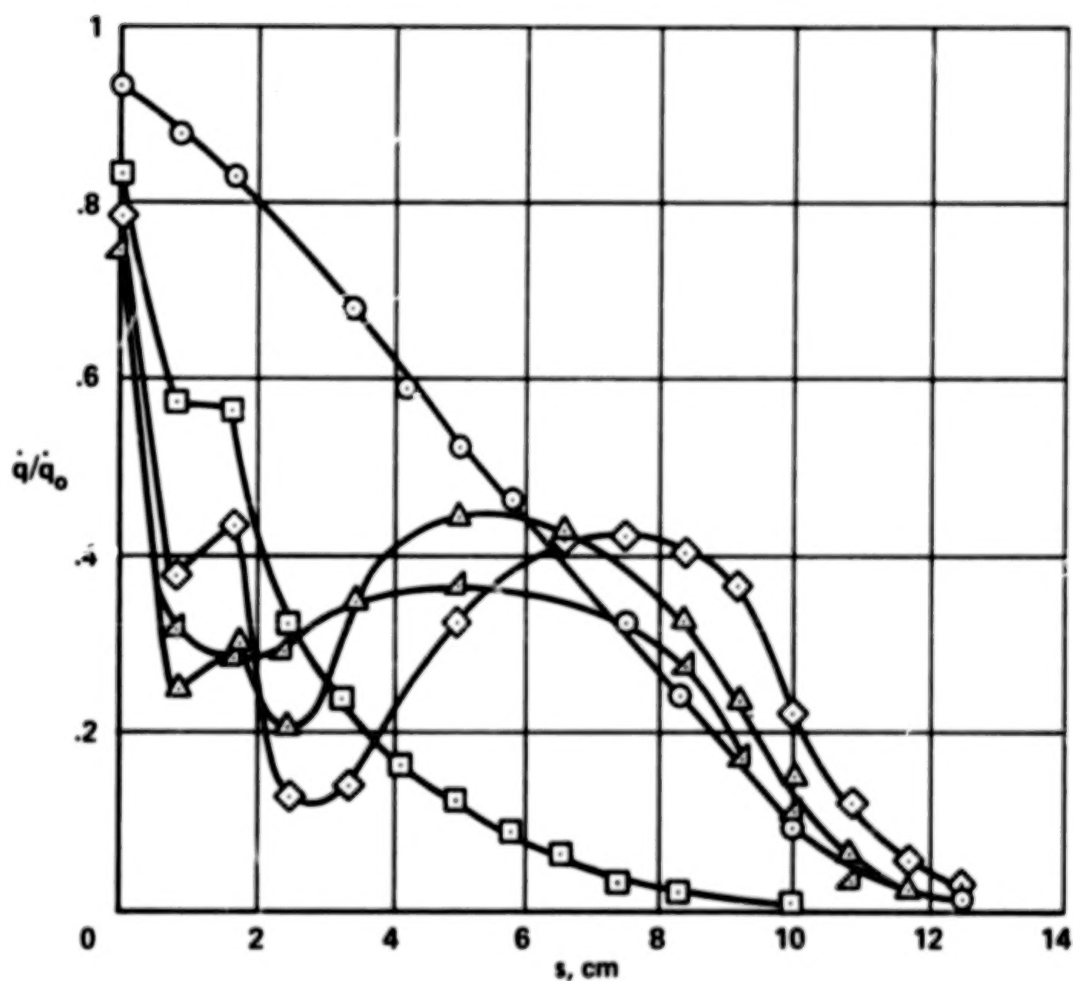
RUN	Re_D	T_{tt}	\dot{q}_0	\underline{m}^*
○ 67H2	0.52×10^6	832	7.81	0.047
□ 62H2	0.60×10^6	736	6.17	0.059
◇ 63H2	0.61×10^6	726	6.03	0.087
△ 64H2	0.54×10^6	786	6.96	0.129
◻ 87H2	0.57×10^6	758	6.57	0.232



(b) $P_{tt} = 138 \text{ N/cm}^2$ (200 psi), $0.047 < \underline{m}^* < 0.232$.

Figure 5.- Continued.

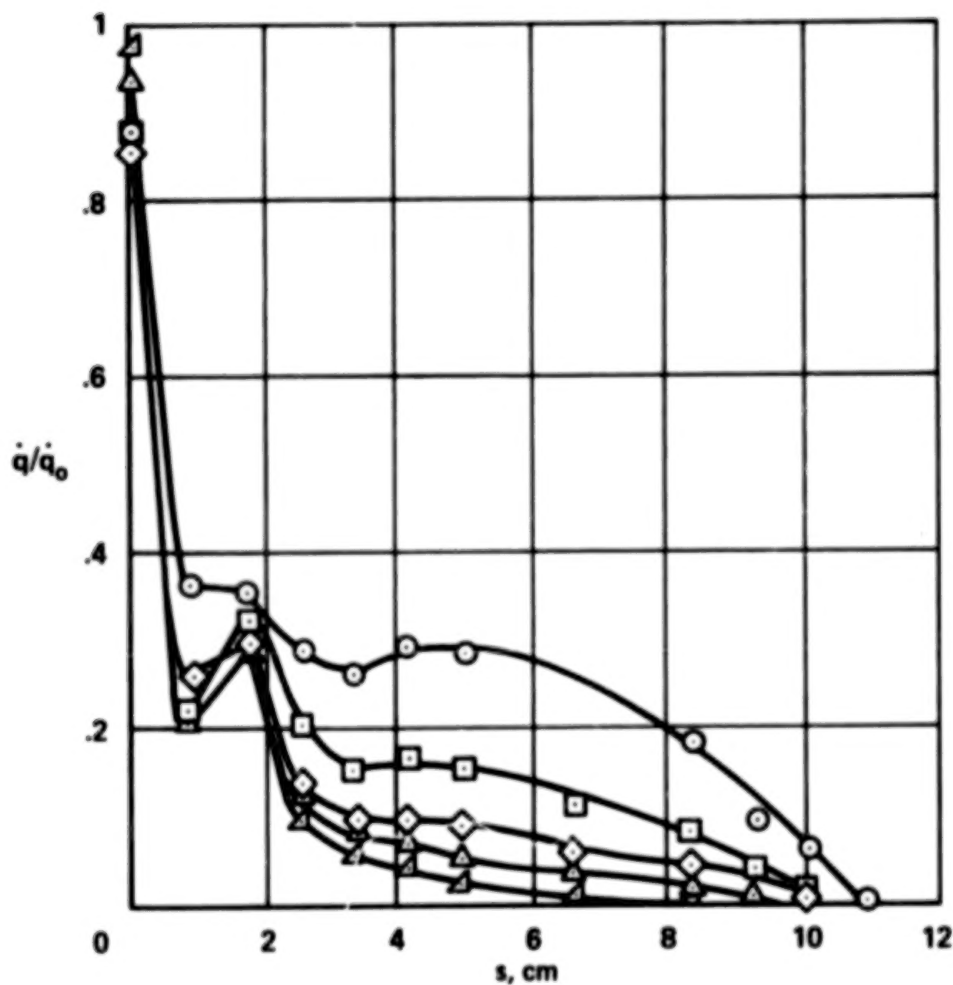
	RUN	Re_D	T_{tt}	\dot{q}_0	\underline{m}^*
○	71H2	1.03×10^6	813	10.52	0.003
□	91H2	1.07×10^6	794	10.17	0.010
◇	75H2	1.14×10^6	763	9.31	0.015
△	68H2	0.99×10^6	832	10.82	0.025
◀	77H2	1.27×10^6	717	8.36	0.030



(c) $P_{tt} = 276 \text{ N/cm}^2$ (400 psi), $0.003 < \underline{m}^* < 0.030$.

Figure 5.- Continued.

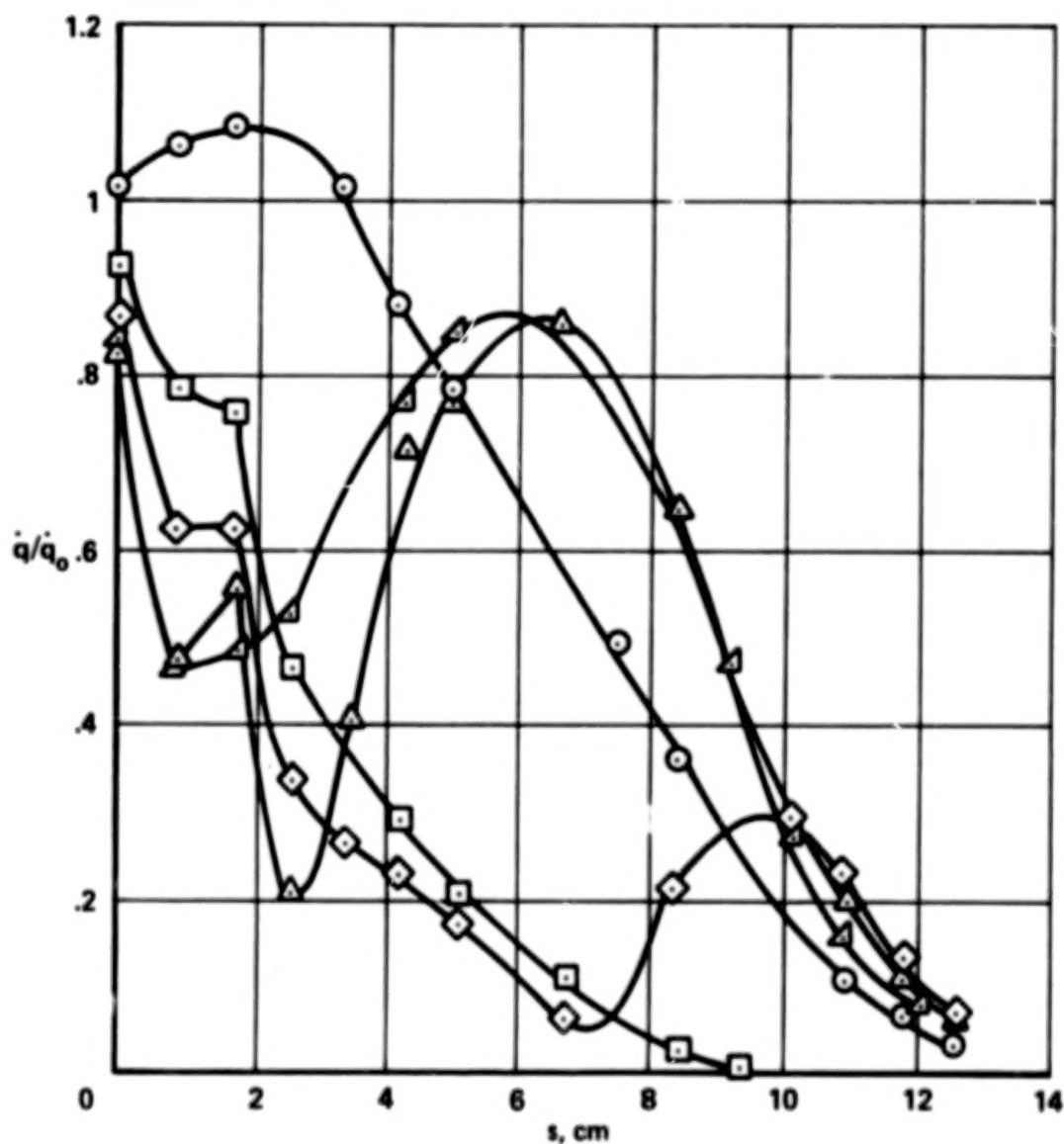
	RUN	Re_D	T_{tt}	\dot{q}_0	\underline{m}^*
○	79H2	1.30×10^6	707	8.14	0.044
□	65H2	1.06×10^6	799	10.19	0.064
◇	82H2	1.04×10^6	807	10.51	0.079
△	85H2	1.07×10^6	795	10.20	0.095
▴	88H2	1.16×10^6	758	9.32	0.110



(d) $P_{tt} = 276 \text{ N/cm}^2$ (400 psi), $0.044 < \underline{m}^* < 0.110$.

Figure 5.- Continued.

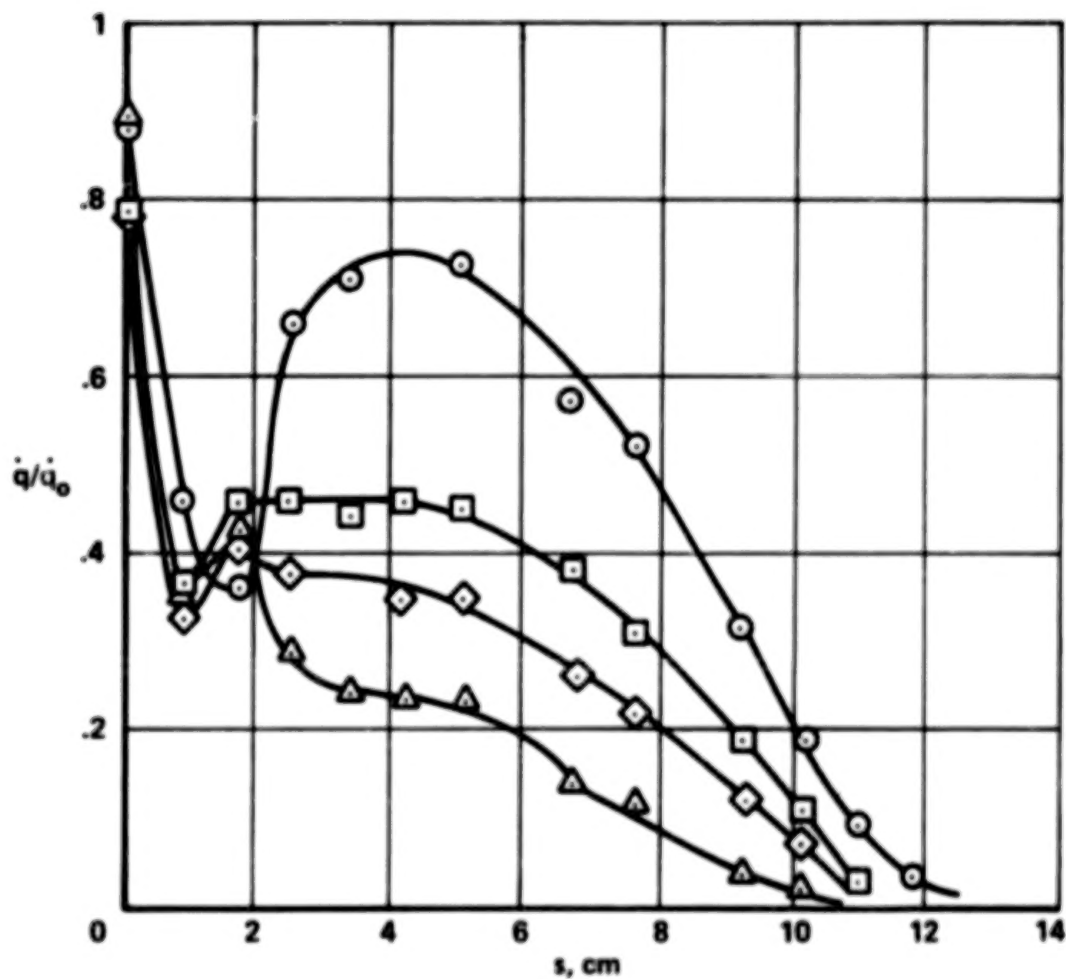
RUN	Re_D	T_{tt}	\dot{q}_0	\underline{m}^*
○ 72H2	2.11×10^6	801	14.39	-0.001
□ 76H2	2.34×10^6	753	12.83	0.007
◇ 92H2	2.05×10^6	817	14.99	0.009
△ 69H2	2.02×10^6	823	14.98	0.012
◐ 78H2	2.55×10^6	715	11.77	0.015



(e) $P_{tt} = 552 \text{ N/cm}^2$ (800 psi), $-0.001 < \underline{m}^* < 0.015$.

Figure 5.- Continued.

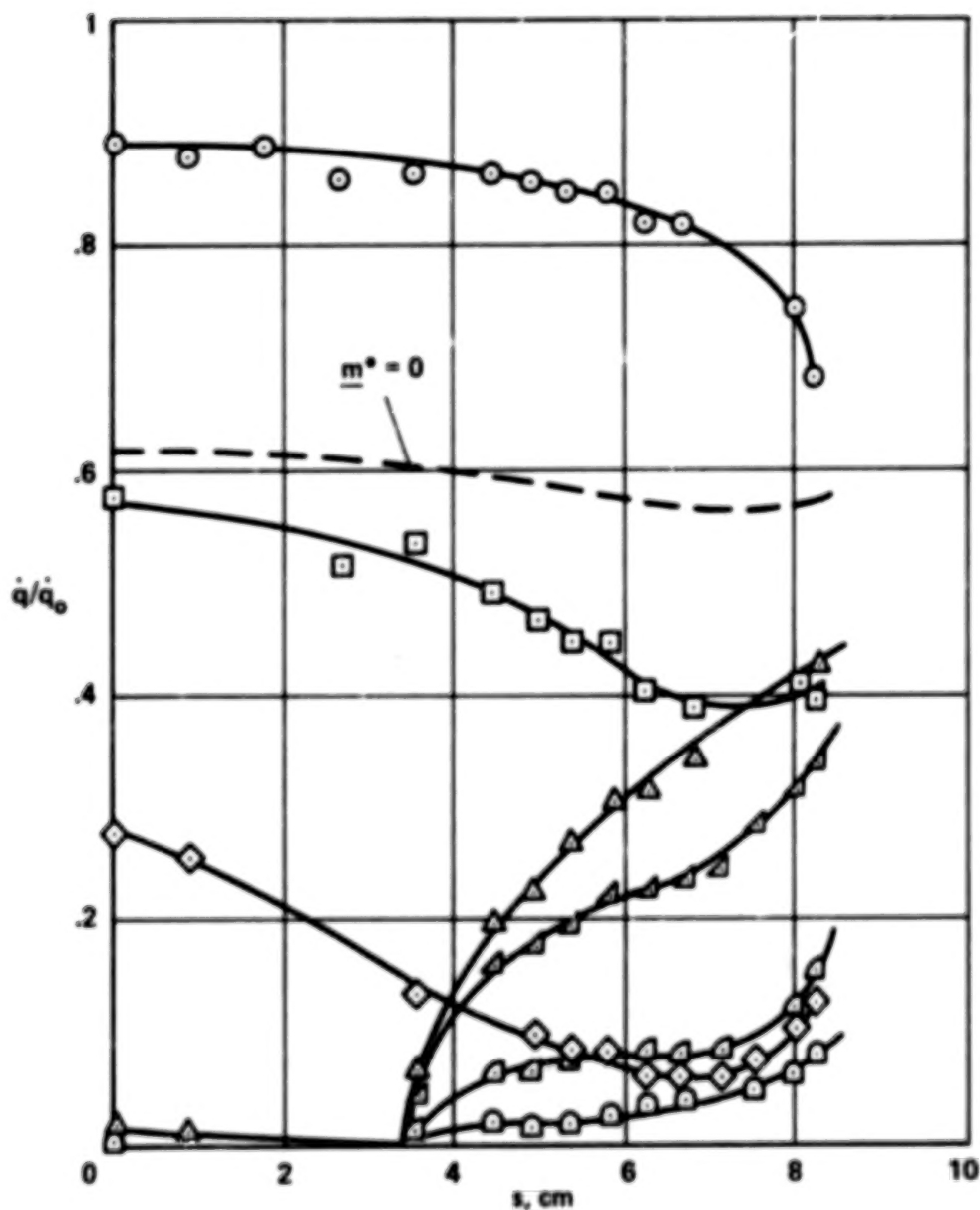
RUN	Re_D	T_{tt}	\dot{q}_0	\underline{m}^*
○ 80H2	2.58×10^6	711	11.67	0.022
□ 66H2	2.08×10^6	807	14.64	0.033
◇ 83H2	1.90×10^6	851	16.16	0.040
△ 89H2	2.39×10^6	742	12.66	0.053



(f) $P_{tt} = 552 \text{ N/cm}^2$ (800 psi), $0.022 < \underline{m}^* < 0.053$.

Figure 5.- Concluded.

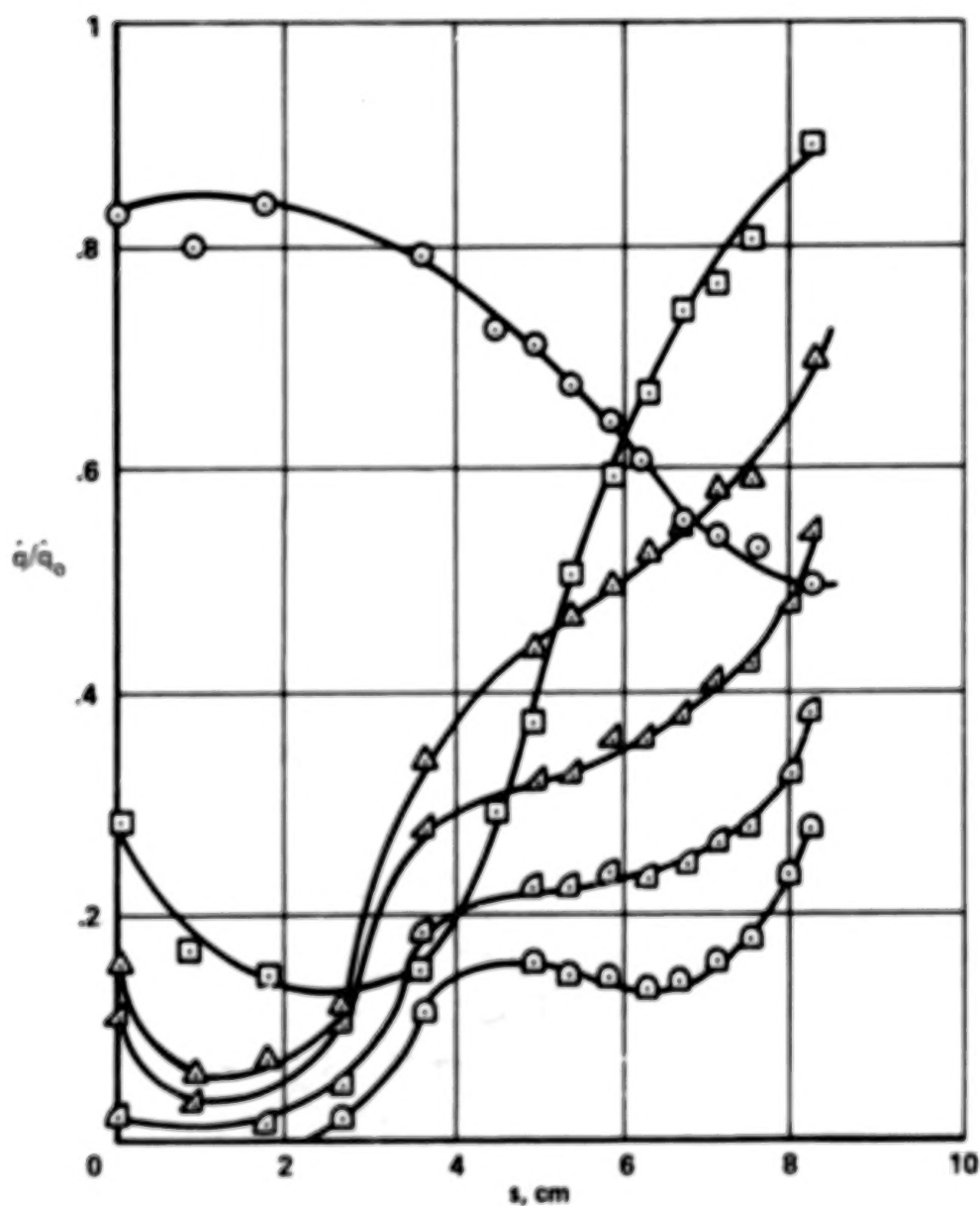
RUN	Re_D	T_{tt}	\dot{q}_0	\underline{m}^*
○ 15SS1	1.30×10^6	702	8.07	-0.002
□ 14SS1	1.44×10^6	658	7.15	0.002
◇ 17SS1	1.15×10^6	753	9.01	0.009
△ 31SS1	1.21×10^6	733	8.49	0.018
▴ 18SS1	1.28×10^6	706	7.91	0.027
▵ 32SS1	1.17×10^6	748	8.94	0.056
◻ 33SS1	1.17×10^6	745	8.96	0.079



(a) $P_{tt} = 276 \text{ N/cm}^2$ (400 psi), $-0.002 < \underline{m}^* < 0.079$.

Figure 6.- Heat transfer distribution over spherical segment model 1.

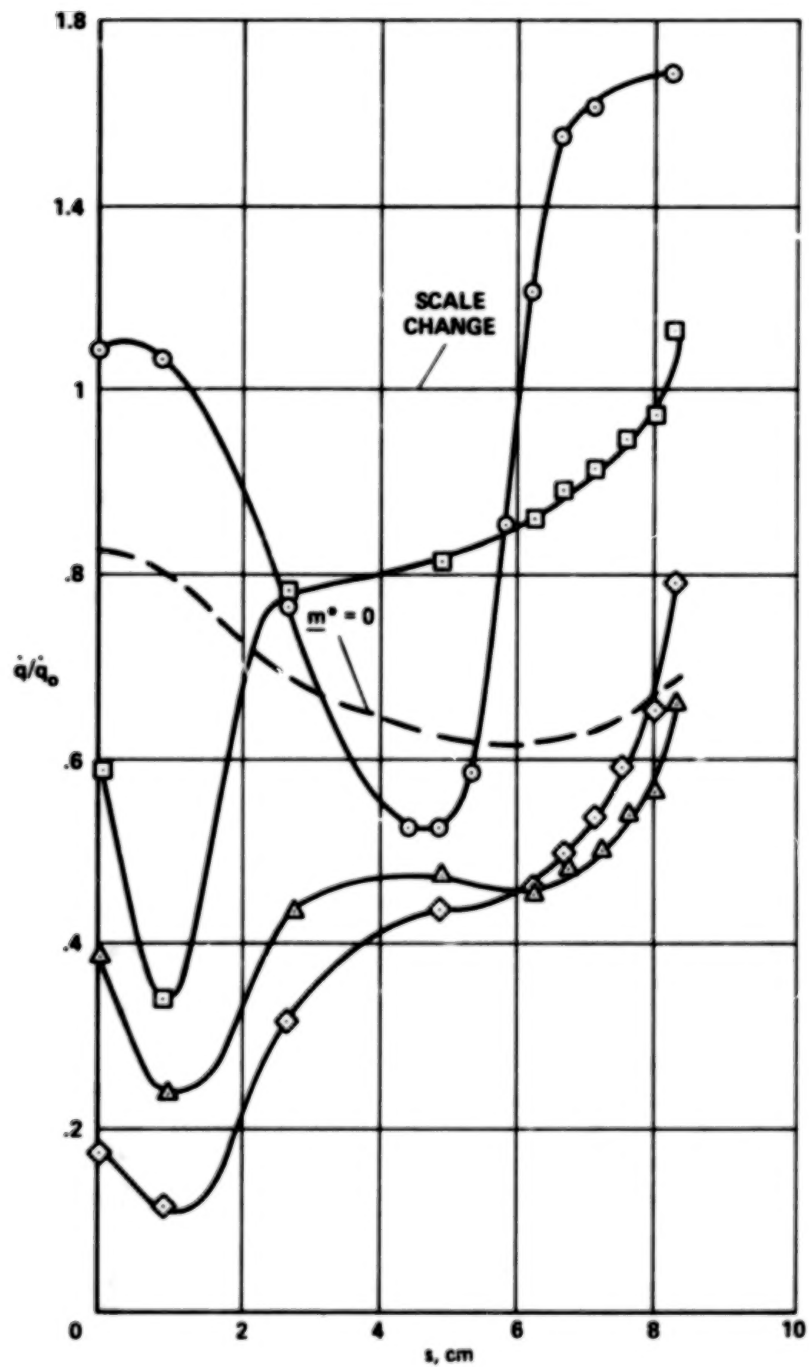
RUN	Re_D	T_{tt}	\dot{q}_0	\underline{m}^*
○ 20SS1	2.39×10^6	742	12.44	-0.001
□ 27SS1	2.32×10^6	755	12.95	0.010
△ 21SS1	2.53×10^6	717	11.74	0.017
▴ 28SS1	2.43×10^6	735	12.37	0.025
◊ 32SS1	2.21×10^6	779	13.81	0.034
◻ 30SS1	2.24×10^6	772	13.61	0.045



(b) $P_{tt} = 552 \text{ N/cm}^2$ (800 psi), $-0.001 < \underline{m}^* < 0.045$.

Figure 6.- Continued.

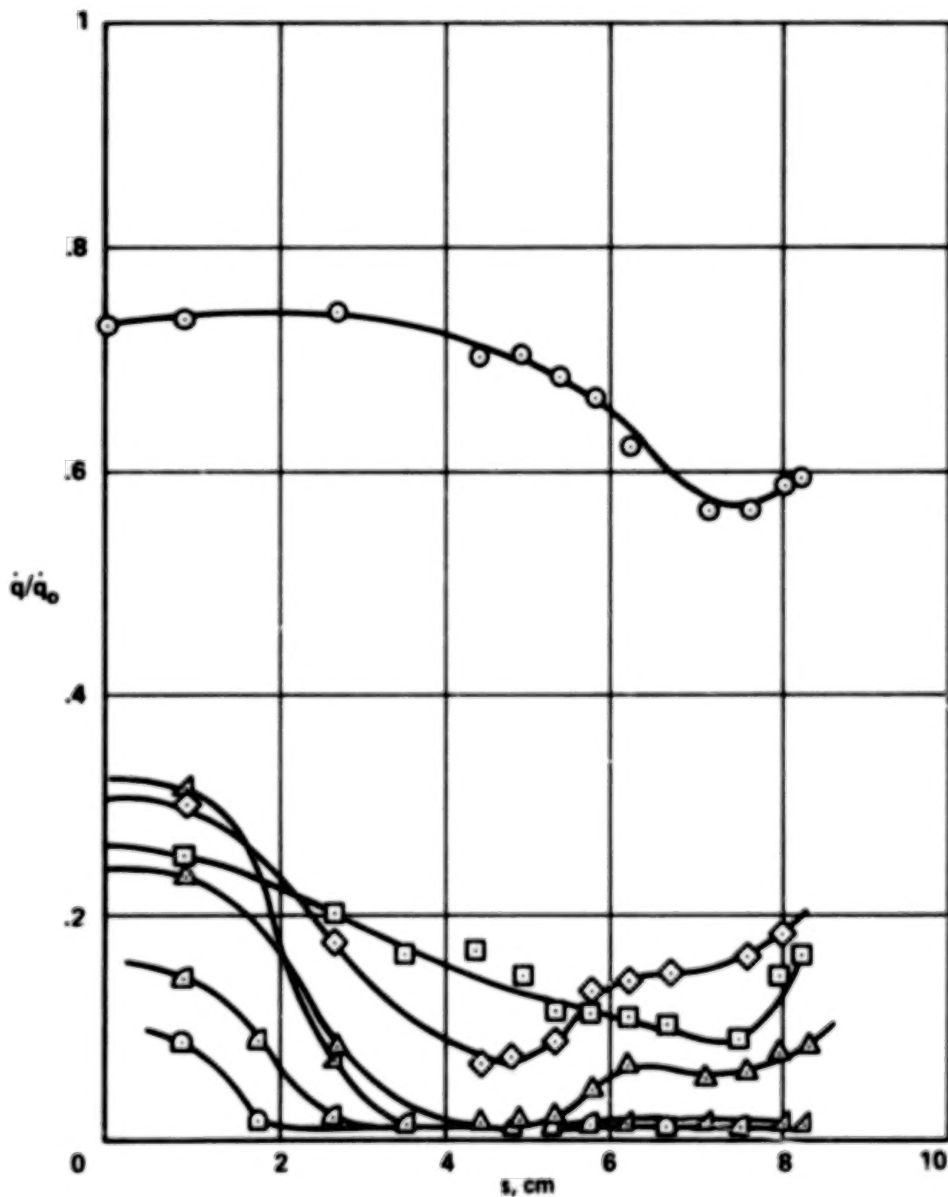
RUN	Re_D	T_{tt}	\dot{q}_0	\underline{m}^*
○ 35SS1	4.93×10^5	729	17.33	0.004
□ 38SS1	4.87×10^5	732	17.51	0.014
◇ 39SS1	3.84×10^5	814	20.41	0.026
△ 40SS1	4.61×10^5	761	18.80	0.026



(c) $P_{tt} = 1103 \text{ N/cm}^2$ (1600 psi), $0.004 < \underline{m}^* < 0.026$.

Figure 6.- Concluded.

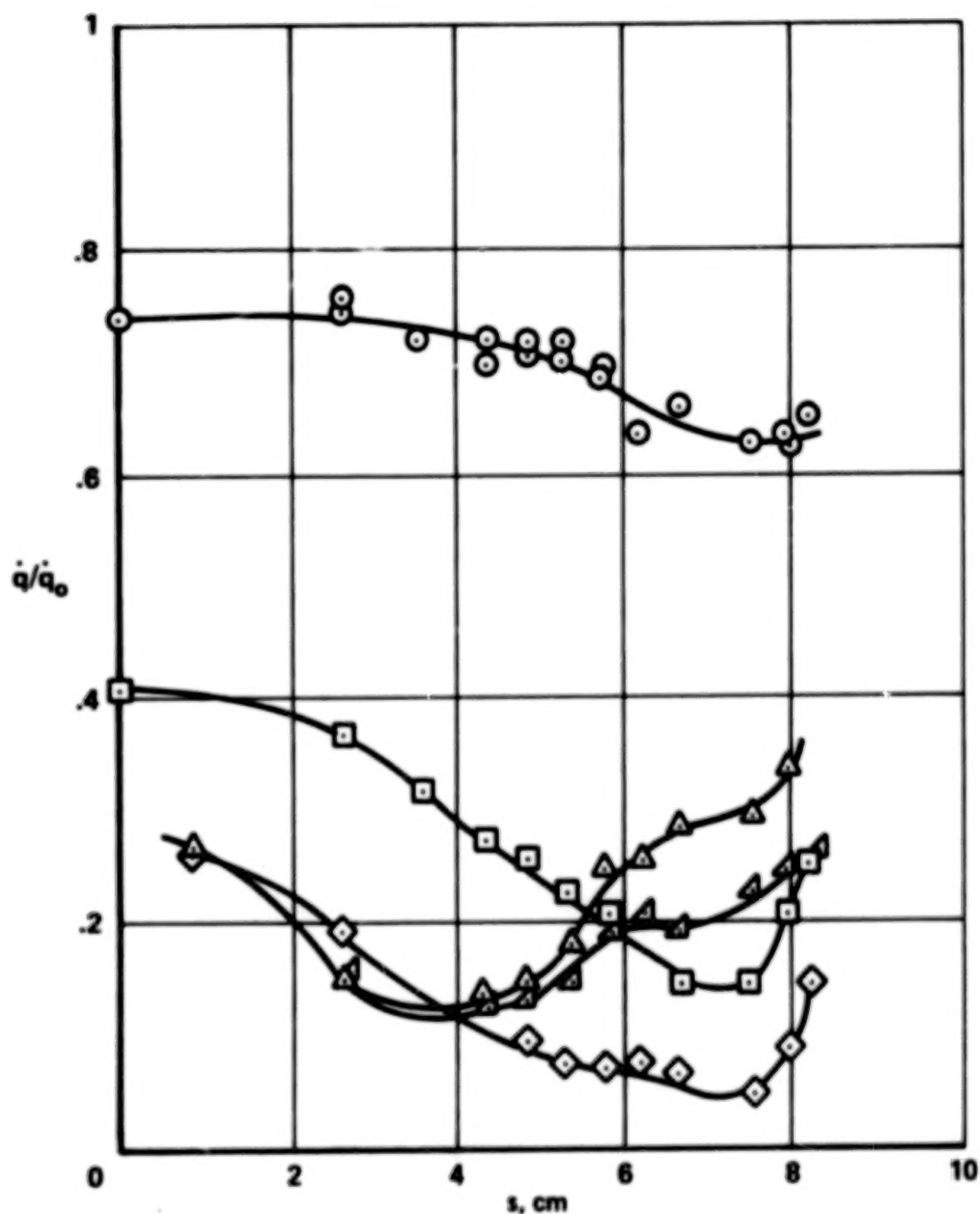
	RUN	Re_D	T_{tt}	\dot{q}_0	\underline{m}^*
○	94SS2	0.61×10^6	758	6.78	-0.001
□	97SS2	0.67×10^6	714	5.97	0.010
◇	3SS2	0.56×10^6	784	7.00	0.027
△	21SS2	0.47×10^6	849	7.97	0.060
▴	6SS2	0.64×10^6	722	6.09	0.099
▵	20SS2	0.45×10^6	877	8.56	0.214
◻	100SS2	0.49×10^6	854	8.33	0.487



(a) $P_{tt} = 138 \text{ N/cm}^2$ (200 psi), $-0.001 < \underline{m}^* < 0.487$.

Figure 7.- Heat transfer distribution over spherical segment model 2.

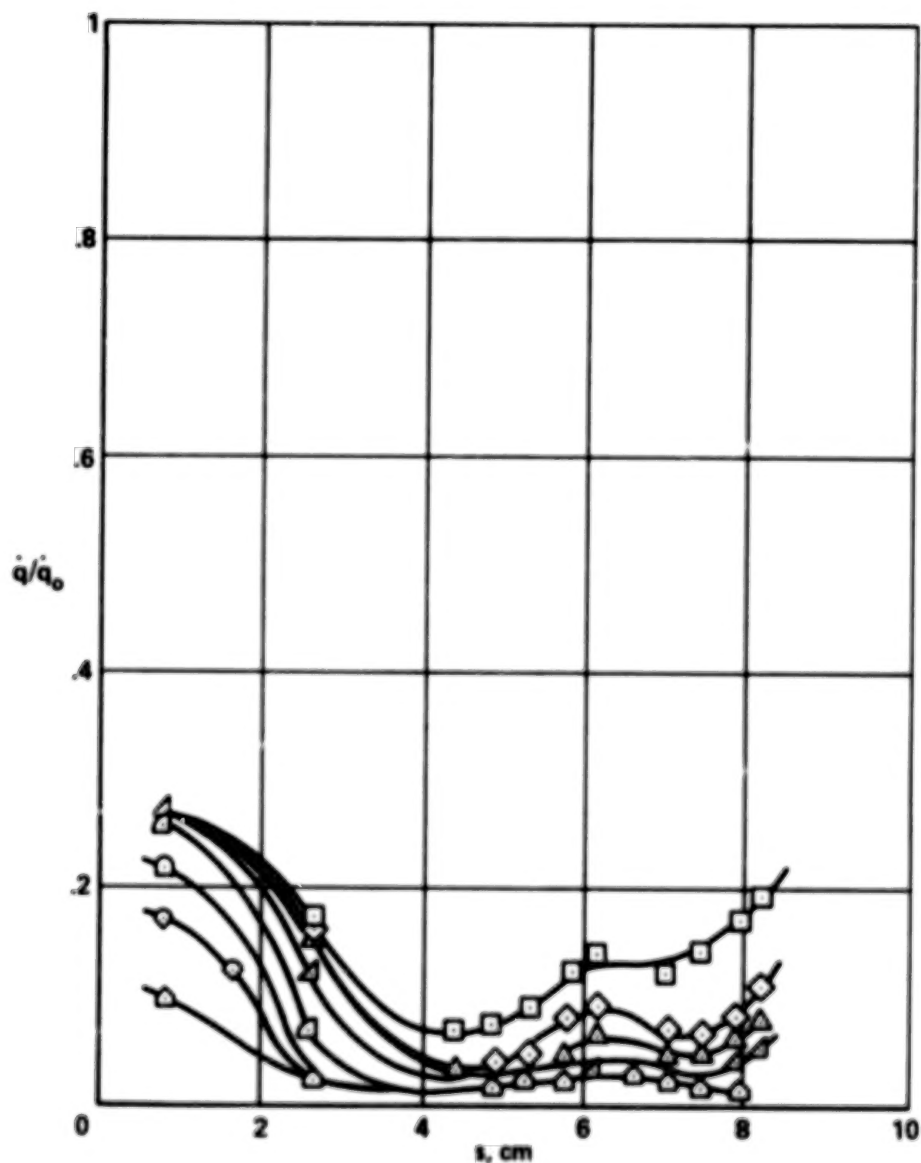
RUN	Re_D	T_{tt}	\dot{q}_0	\underline{m}^*
○ 10SS2	1.13×10^6	767	9.39	-0.002
□ 11SS2	1.03×10^6	812	10.46	0.005
◇ 8SS2	1.12×10^6	775	9.61	0.008
△ 98SS2	1.25×10^6	725	8.57	0.013
▴ 24SS2	0.90×10^6	878	11.97	0.022



(b) $P_{tt} = 276 \text{ N/cm}^2$ (400 psi), $-0.002 < \underline{m}^* < 0.022$.

Figure 7.- Continued.

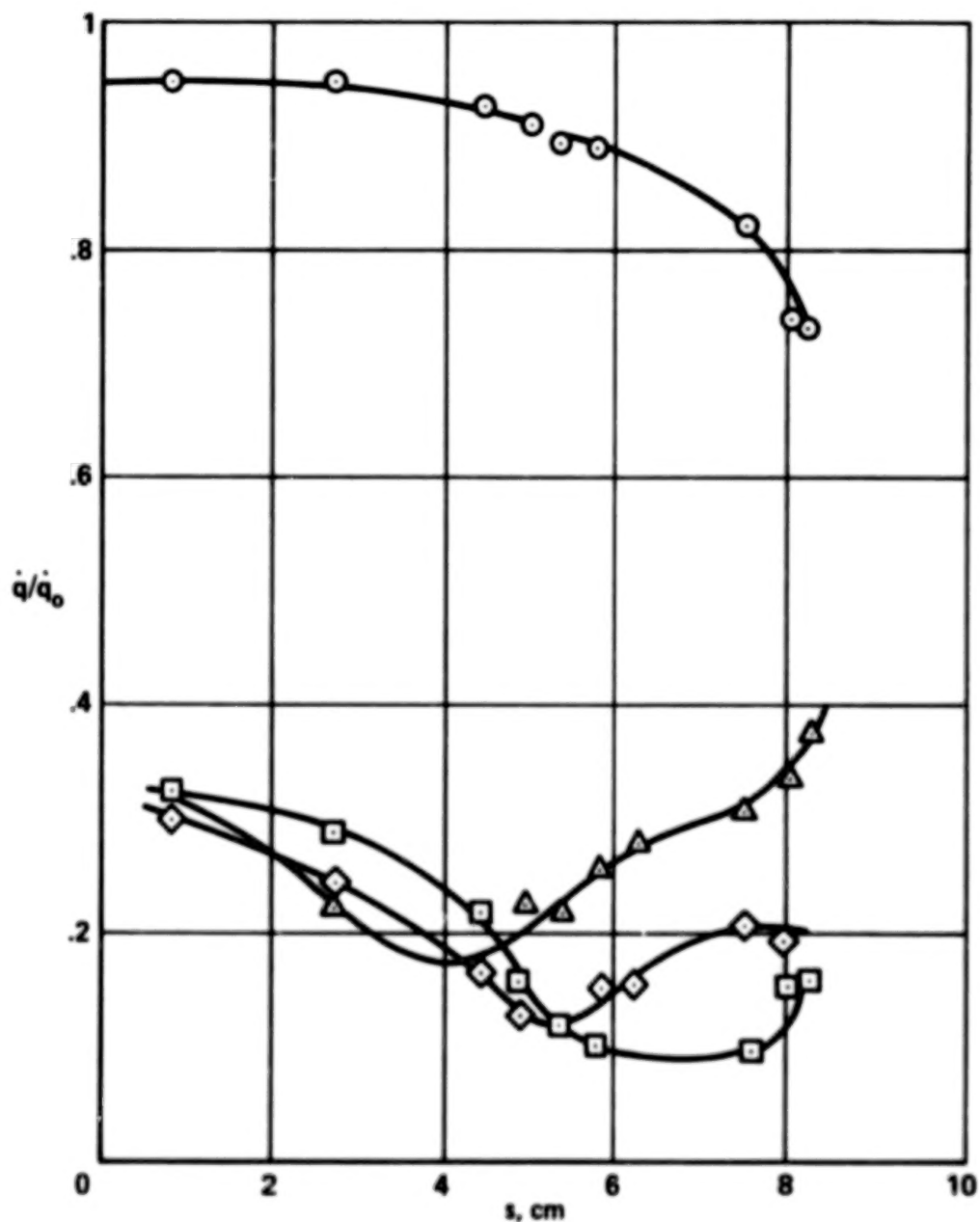
	RUN	Re_D	T_n	\dot{q}_0	\underline{m}^*
□	9SS2	1.09×10^6	786	9.91	0.035
◇	12SS2	1.14×10^6	762	9.43	0.045
△	13SS2	1.27×10^6	717	8.40	0.059
▵	14SS2	1.18×10^6	747	9.09	0.079
▢	15SS2	1.28×10^6	712	8.34	0.114
□	17SS2	1.04×10^6	807	10.43	0.155
◇	101SS2	1.00×10^6	831	11.05	0.205
△	104SS2	1.13×10^6	770	9.73	0.238



(c) $P_{tt} = 276 \text{ N/cm}^2$ (400 psi), $0.035 < \underline{m}^* < 0.238$.

Figure 7.- Continued.

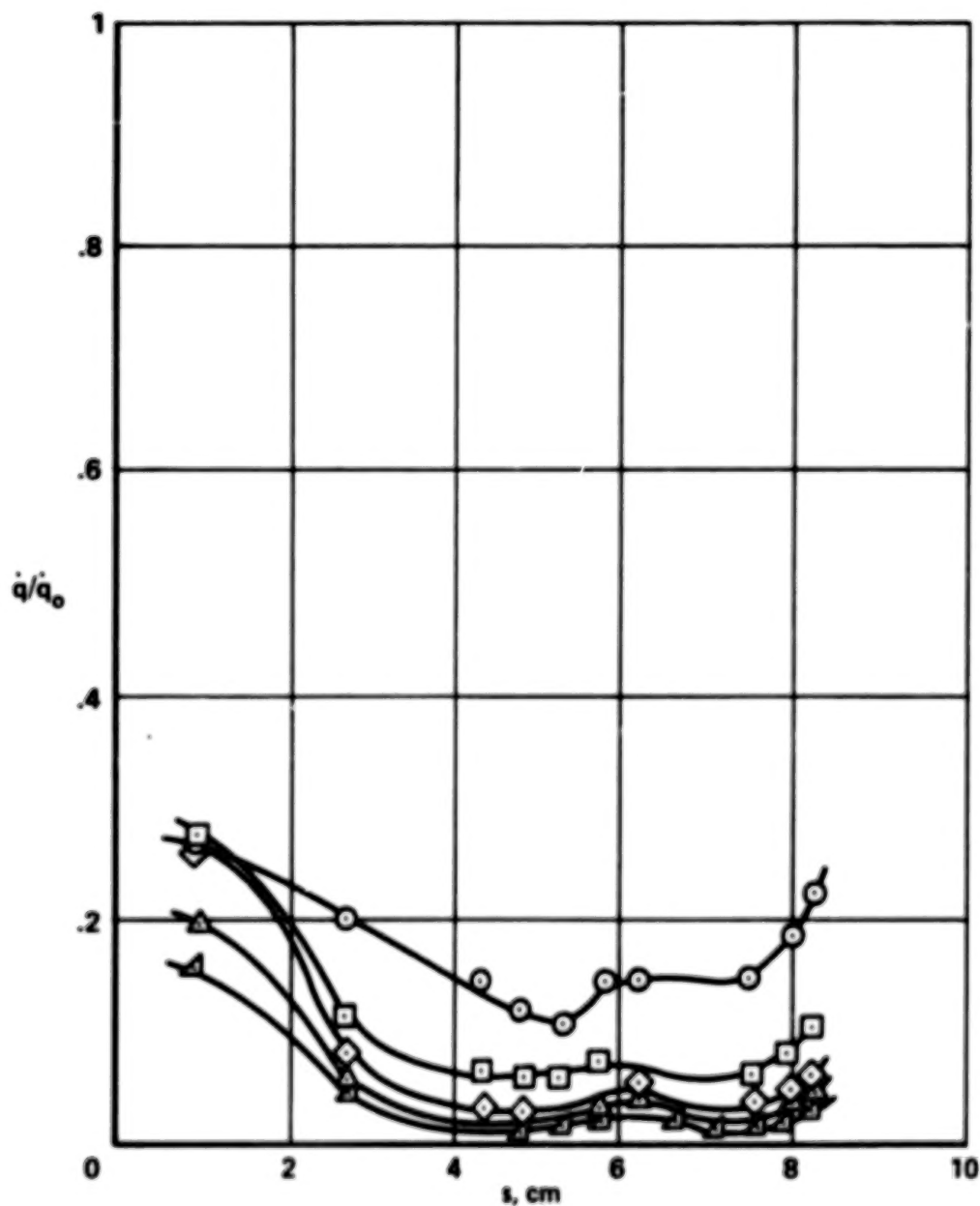
RUN	Re_D	T_{tt}	\dot{q}_0	\underline{m}^*
○ 96SS2	2.28×10^6	764	13.44	-0.003
□ 27SS2	2.14×10^6	796	14.20	0.005
◇ 99SS2	2.39×10^6	743	12.70	0.006
△ 25SS2	1.93×10^6	844	15.90	0.020



(d) $P_{tt} = 552 \text{ N/cm}^2$ (800 psi), $-0.003 < \underline{m}^* < 0.020$.

Figure 7.- Continued.

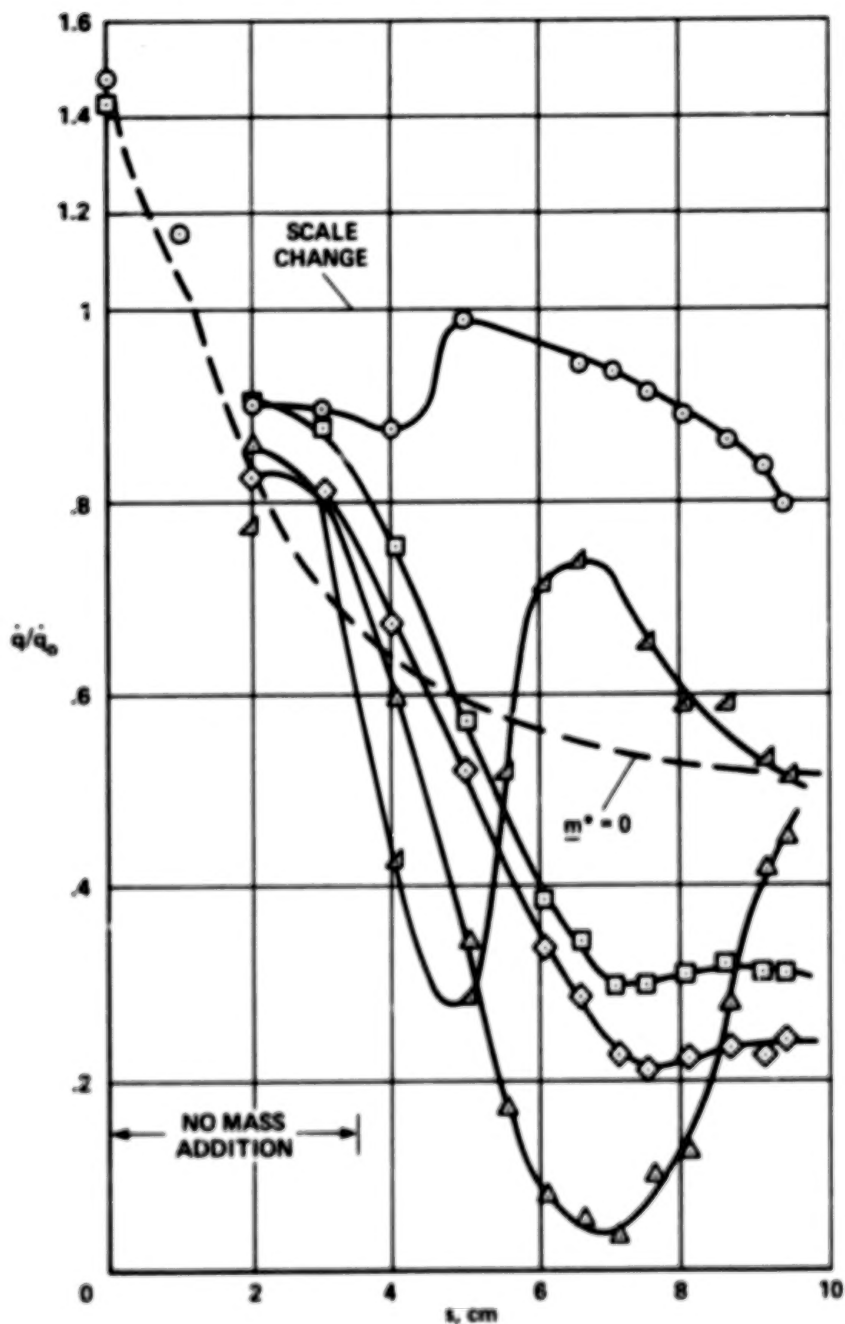
	RUN	Re_D	T_{tt}	\dot{q}_0	\underline{m}^*
○	26SS2	1.99×10^6	831	15.46	0.035
□	102SS2	2.09×10^6	805	14.70	0.055
◇	103SS2	2.26×10^6	768	13.44	0.072
△	106SS2	2.37×10^6	748	13.00	0.085
▴	105SS2	2.29×10^6	762	13.50	0.104



(e) $P_{tt} = 552 \text{ N/cm}^2$ (800 psi), $0.035 < \underline{m}^* < 0.104$.

Figure 7.- Concluded.

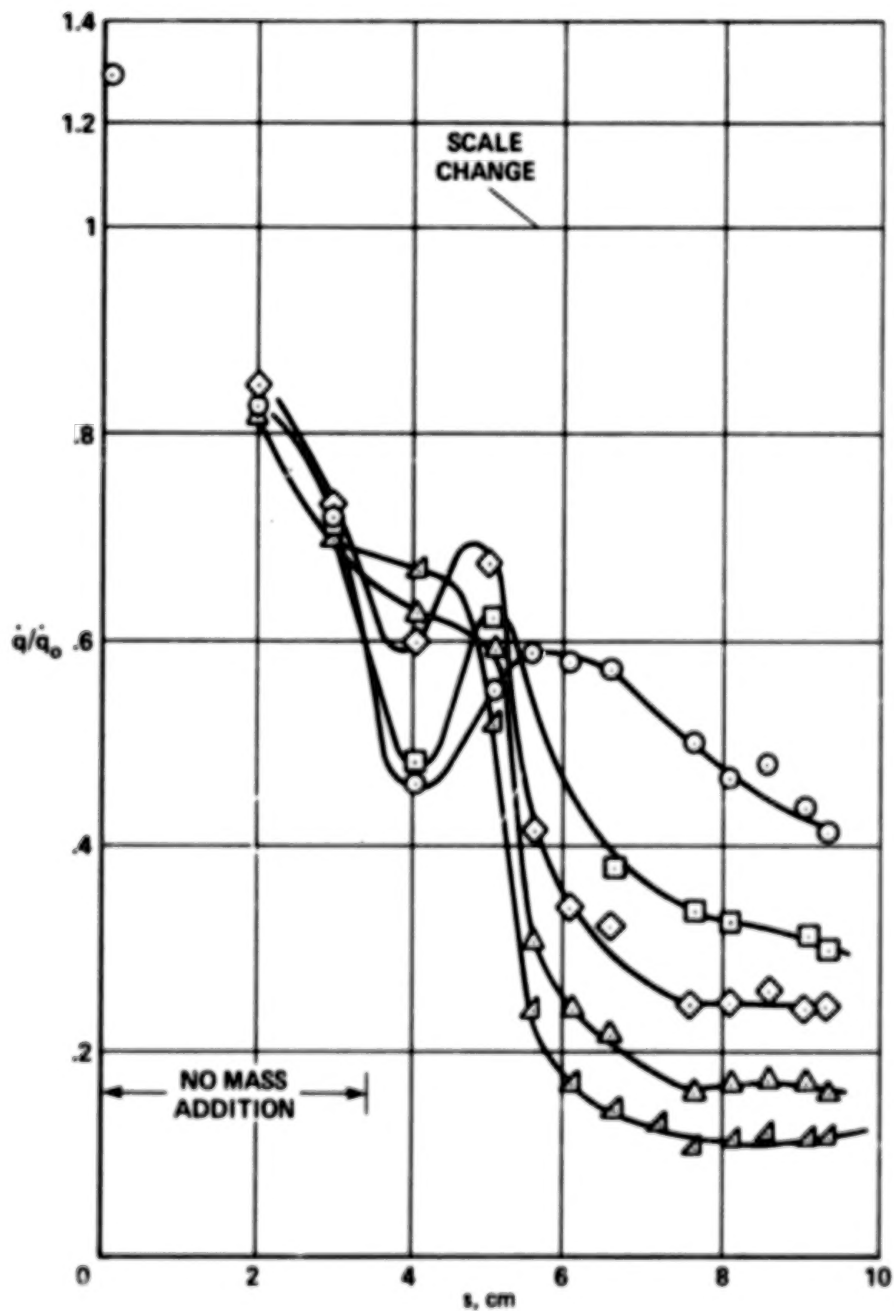
RUN	Re_D	T_{tt}	\dot{q}_0	\underline{m}^*
○ 43C1	1.46×10^6	662	7.21	-0.001
□ 52C1	1.18×10^6	742	8.81	0.004
◇ 44C1	1.45×10^6	666	7.26	0.004
△ 45C1	1.11×10^6	766	9.36	0.009
▴ 46C1	1.23×10^6	722	8.48	0.031



(a) $P_{tt} = 276 \text{ N/cm}^2$ (400 psi), $-0.001 < \underline{m}^* < 0.031$.

Figure 8.- Heat transfer distribution over conical model 1.

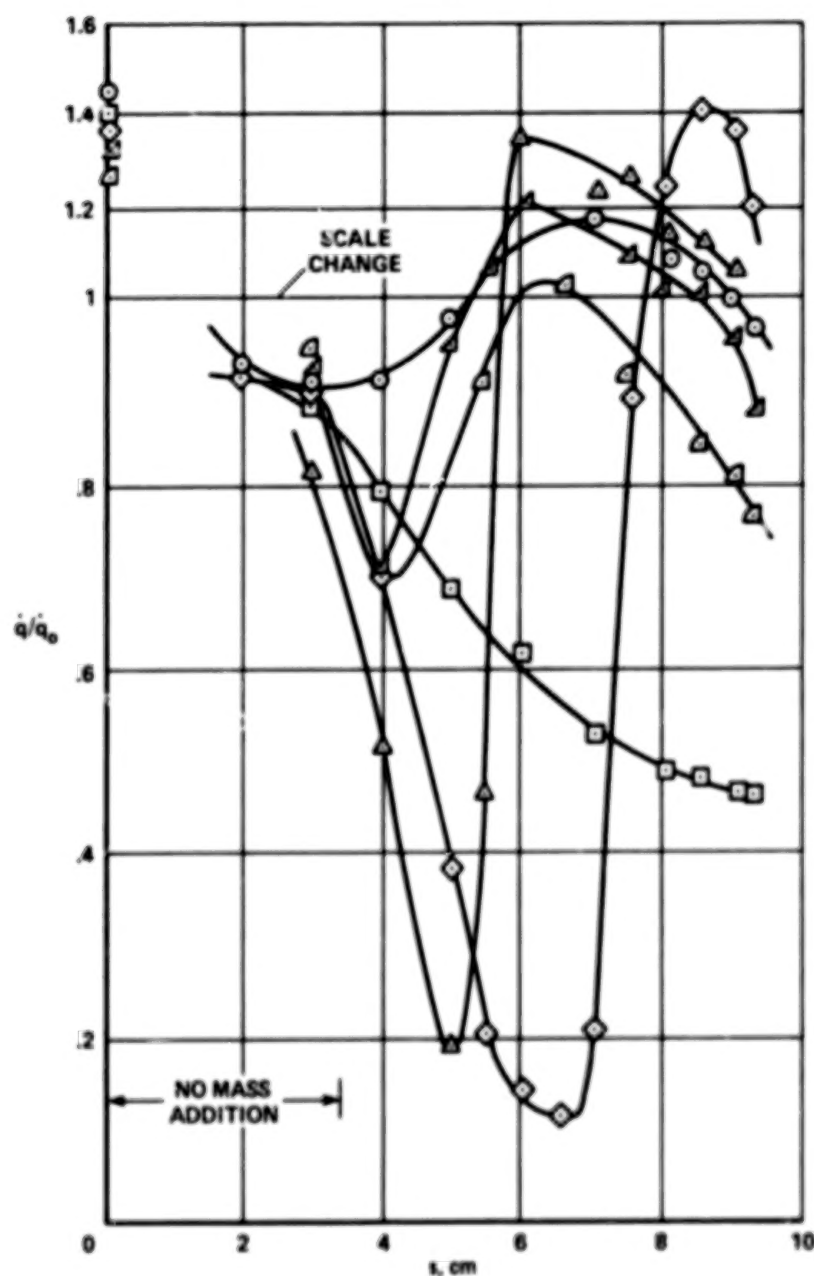
RUN	Re_D	T_{tt}	\dot{q}_0	\underline{m}^*
○ 47C1	1.17×10^6	757	9.44	0.041
□ 48C1	1.06×10^6	790	10.06	0.055
◇ 49C1	1.21×10^6	743	9.13	0.063
△ 50C1	1.14×10^6	757	9.32	0.077
▴ 51C1	1.12×10^6	764	9.53	0.090



(b) $P_{tt} = 276 \text{ N/cm}^2$ (400 psi), $0.041 < \underline{m}^* < 0.090$.

Figure 8.- Continued.

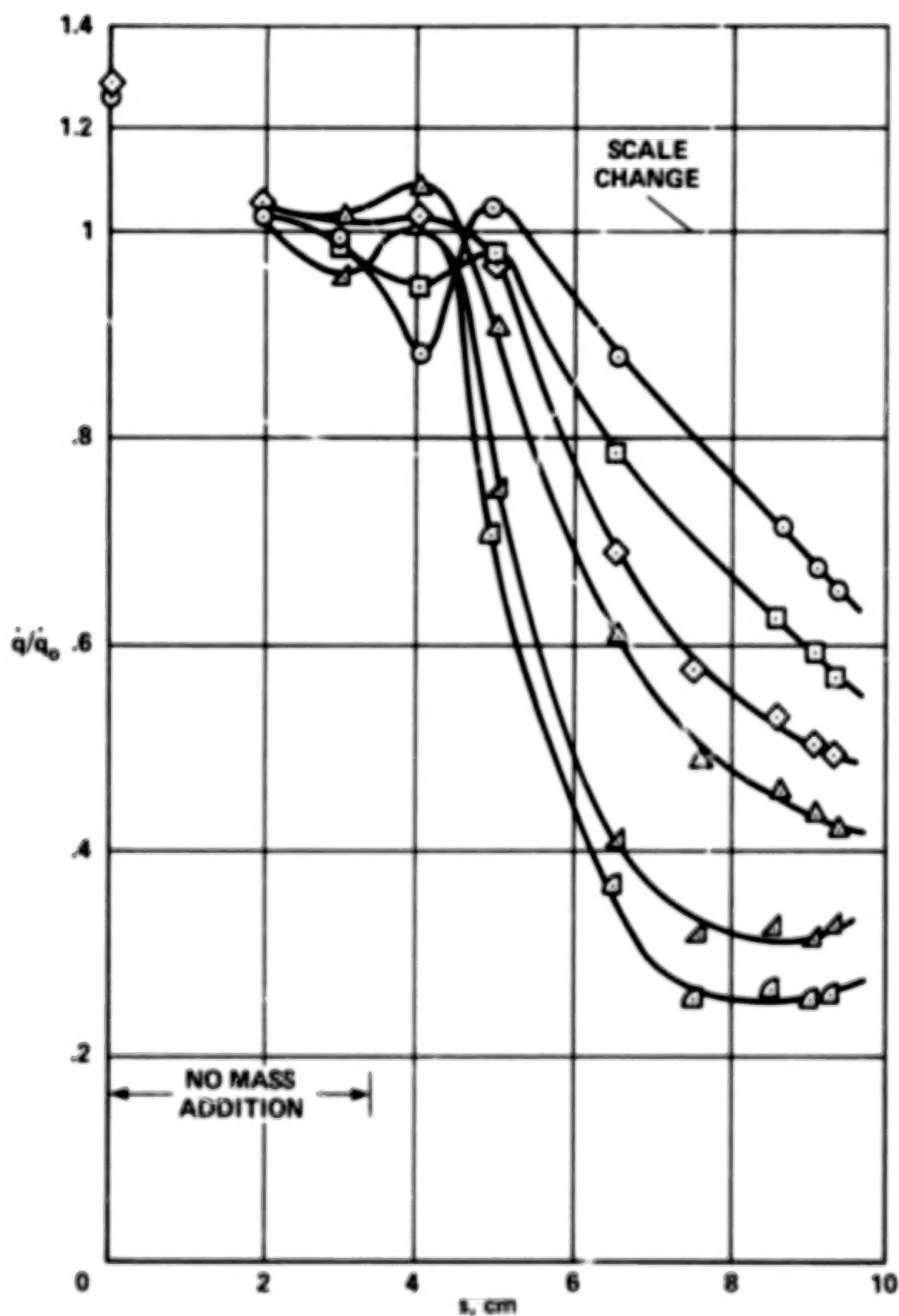
RUN	Re_D	T_{tt}	\dot{q}_0	\underline{m}^*
○ 53C1	2.23×10^6	774	13.57	-0.003
□ 54C1	2.18×10^6	783	13.98	0.001
◇ 63C1	2.37×10^6	745	12.69	0.006
△ 57C1	2.67×10^6	693	10.95	0.012
▴ 64C1	2.39×10^6	742	12.63	0.016
◁ 58C1	2.40×10^6	740	12.51	0.020



(c) $P_{tt} = 552 \text{ N/cm}^2$ (800 psi), $-0.003 < \underline{m}^* < 0.020$.

Figure 8.- Continued.

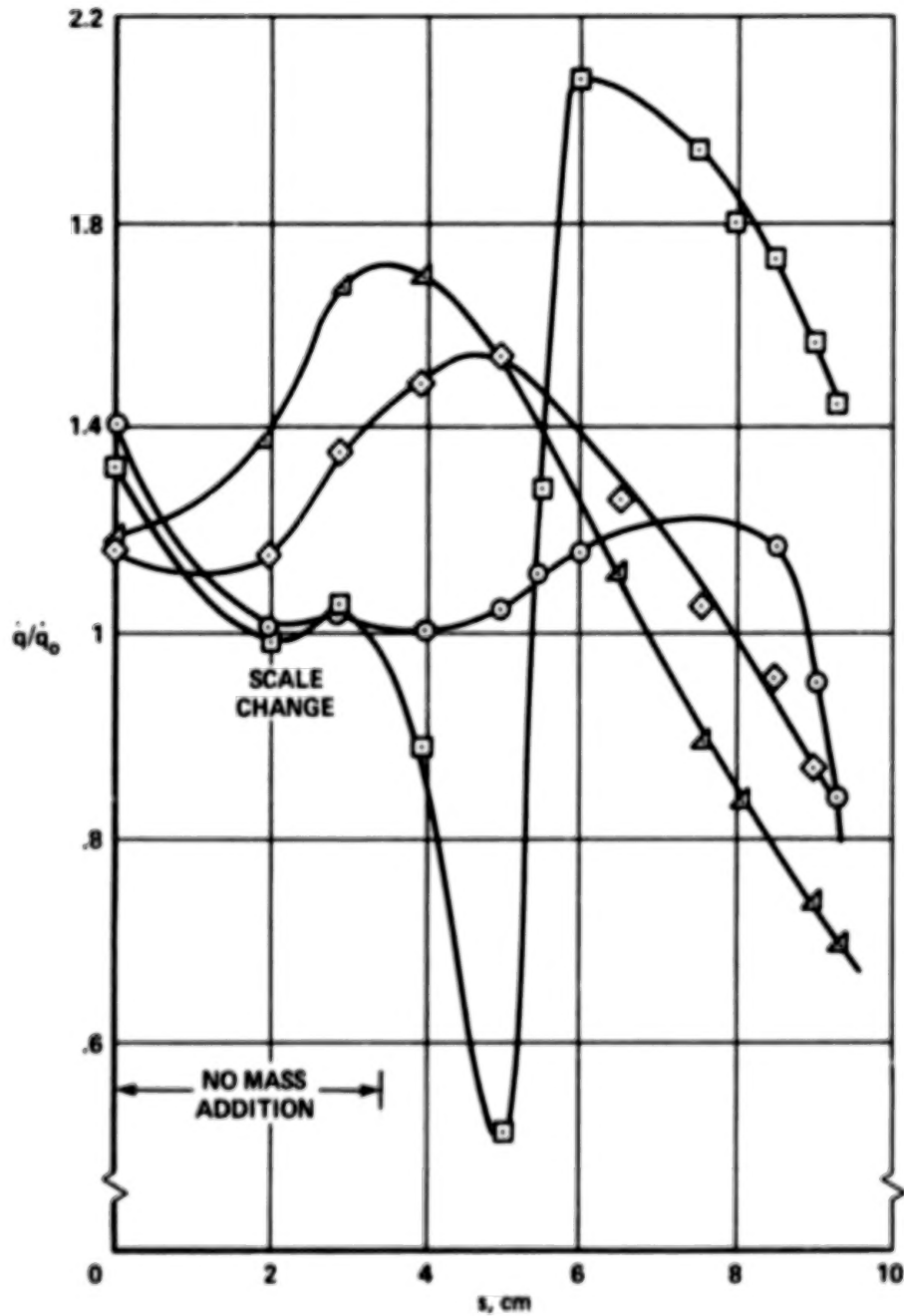
RUN	Re_D	T_{tt}	\dot{q}_0	\underline{m}^*
○ 59C1	2.35×10^6	751	12.98	0.026
□ 60C1	2.30×10^6	758	13.31	0.031
◇ 61C1	2.42×10^6	737	12.53	0.037
△ 62C1	2.48×10^6	726	12.38	0.041
▲ 65C1	2.09×10^6	802	14.74	0.054
▤ 66C1	2.31×10^6	757	13.25	0.059



(d) $P_{tt} = 552 \text{ N/cm}^2$ (800 psi), $0.026 < \underline{m}^* < 0.059$.

Figure 8.- Continued.

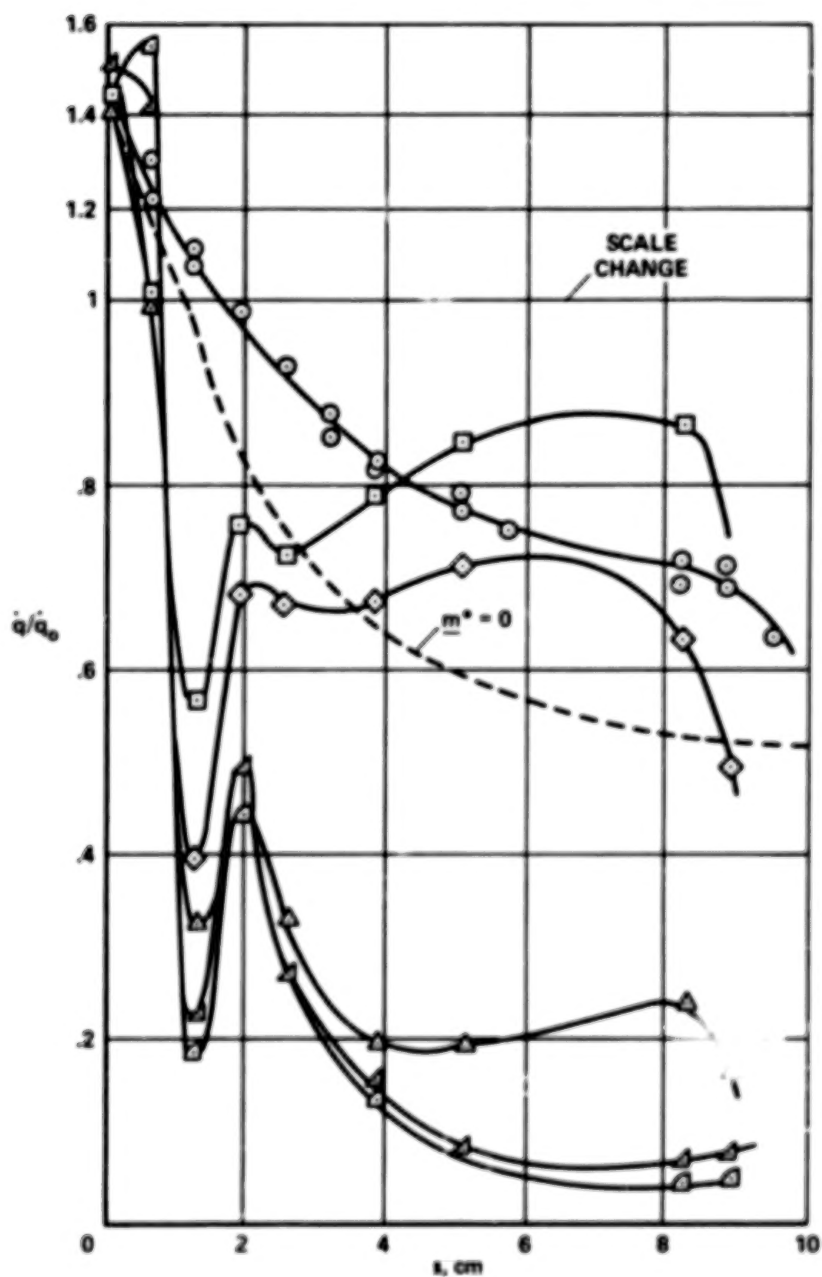
RUN	Re_D	T_{tt}	\dot{q}_0	\underline{m}^*
○ 69C1	4.83×10^6	738	17.33	-0.001
□ 70C1	4.93×10^6	730	17.22	0.007
◇ 71C1	5.15×10^6	711	16.71	0.014
△ 73C1	5.26×10^6	705	16.62	0.024



(e) $P_{tt} = 1103 \text{ N/cm}^2$ (1600 psi), $-0.001 < \underline{m}^* < 0.024$.

Figure 8.- Concluded.

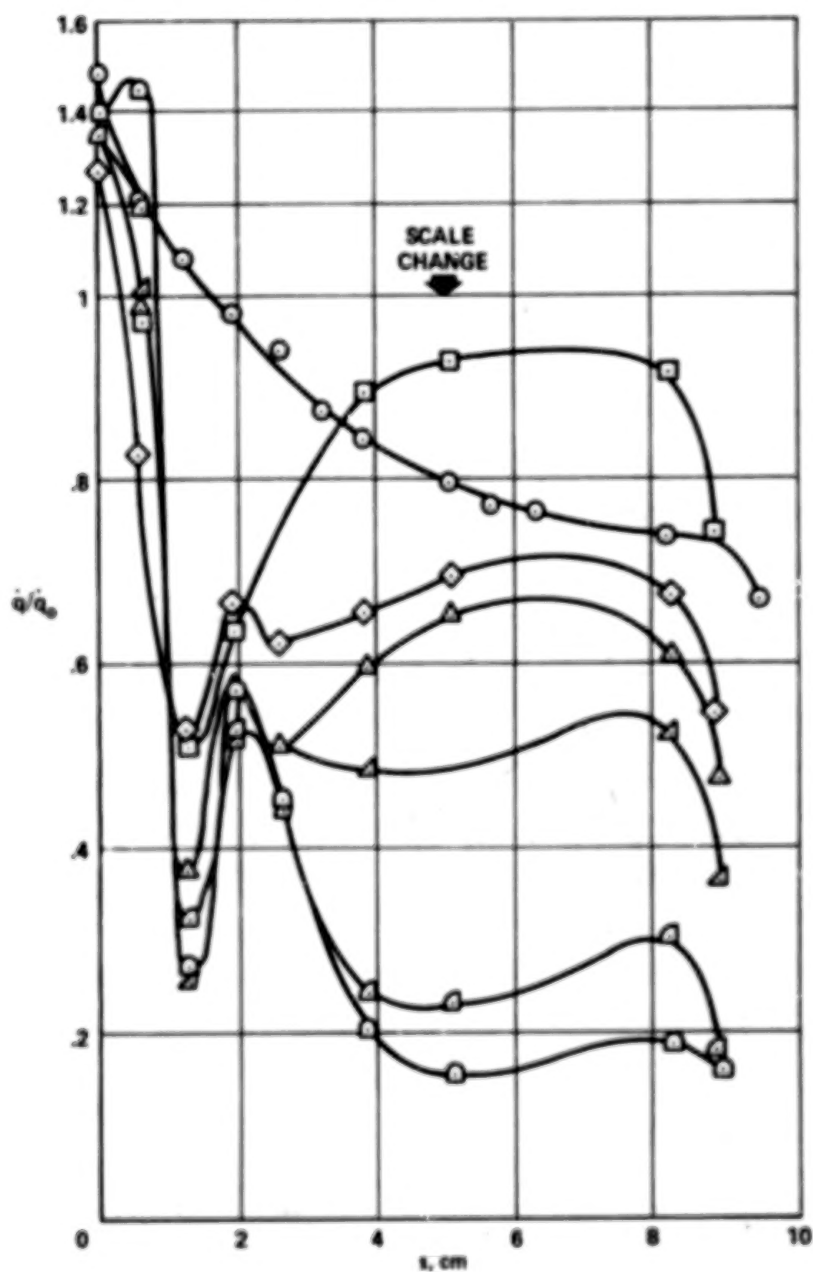
RUN	Re_D	T_{tt}	\dot{q}_0	\underline{m}^*
○ 36C2	0.50×10^6	848	8.10	-0.000
□ 29C2	0.74×10^6	675	5.44	0.023
◇ 30C2	0.46×10^6	889	8.89	0.068
△ 58C2	0.64×10^6	712	5.82	0.139
▴ 57C2	0.60×10^6	739	6.27	0.343
◁ 51C2	0.60×10^6	739	6.23	0.509



(a) $P_{tt} = 138 \text{ N/cm}^2$ (200 psi), $0 < \underline{m}^* < 0.509$.

Figure 9.- Heat transfer distribution over conical model 2.

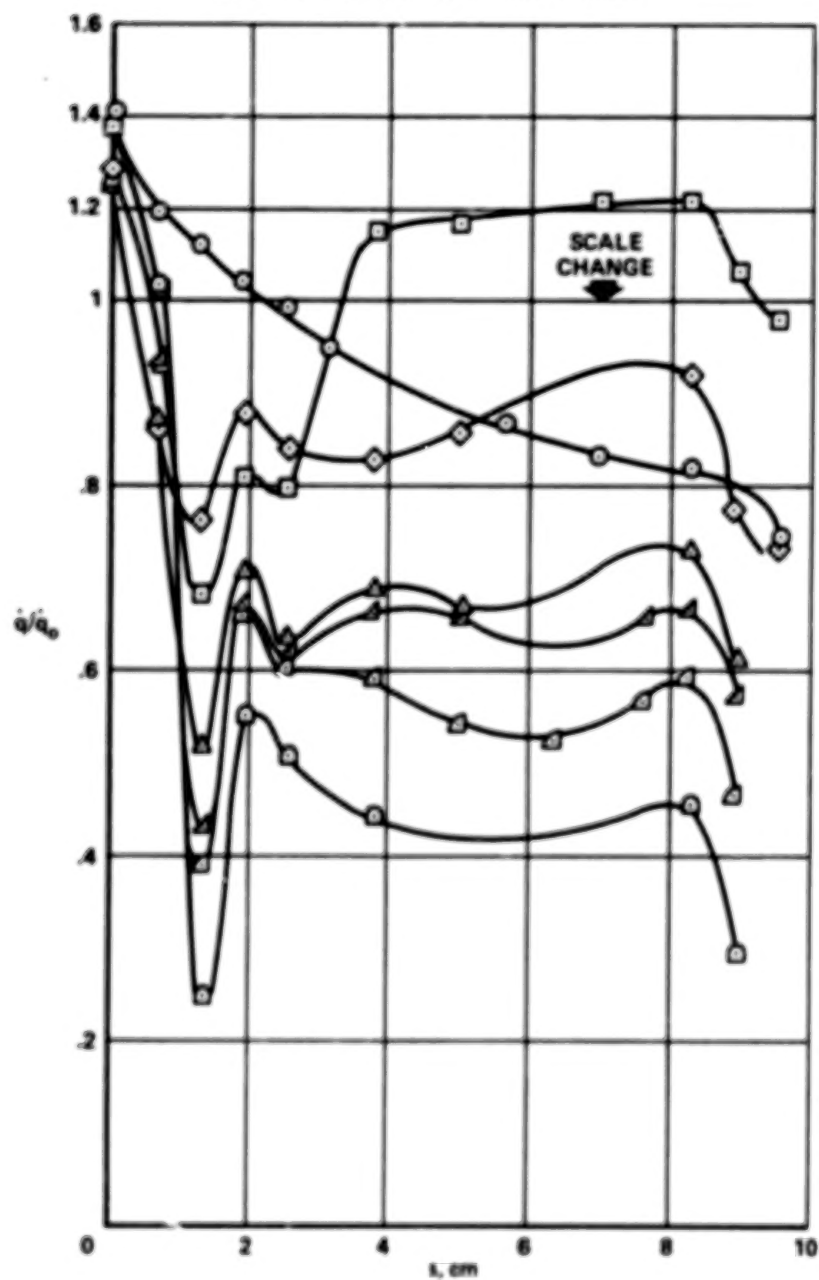
RUN	Re_D	T_{tt}	\dot{q}_0	\underline{m}^*
○ 43C2	1.13×10^5	770	9.45	-0.001
□ 42C2	1.13×10^5	771	9.51	0.007
◇ 41C2	0.96×10^5	847	11.25	0.045
△ 40C2	1.00×10^5	824	10.73	0.072
▴ 39C2	0.89×10^5	884	12.09	0.106
▵ 55C2	1.20×10^5	744	8.99	0.157
◻ 50C2	1.24×10^5	726	8.50	0.248



(b) $P_{tt} = 276 \text{ N/cm}^2$ (400 psi), $-0.001 < \underline{m}^* < 0.248$.

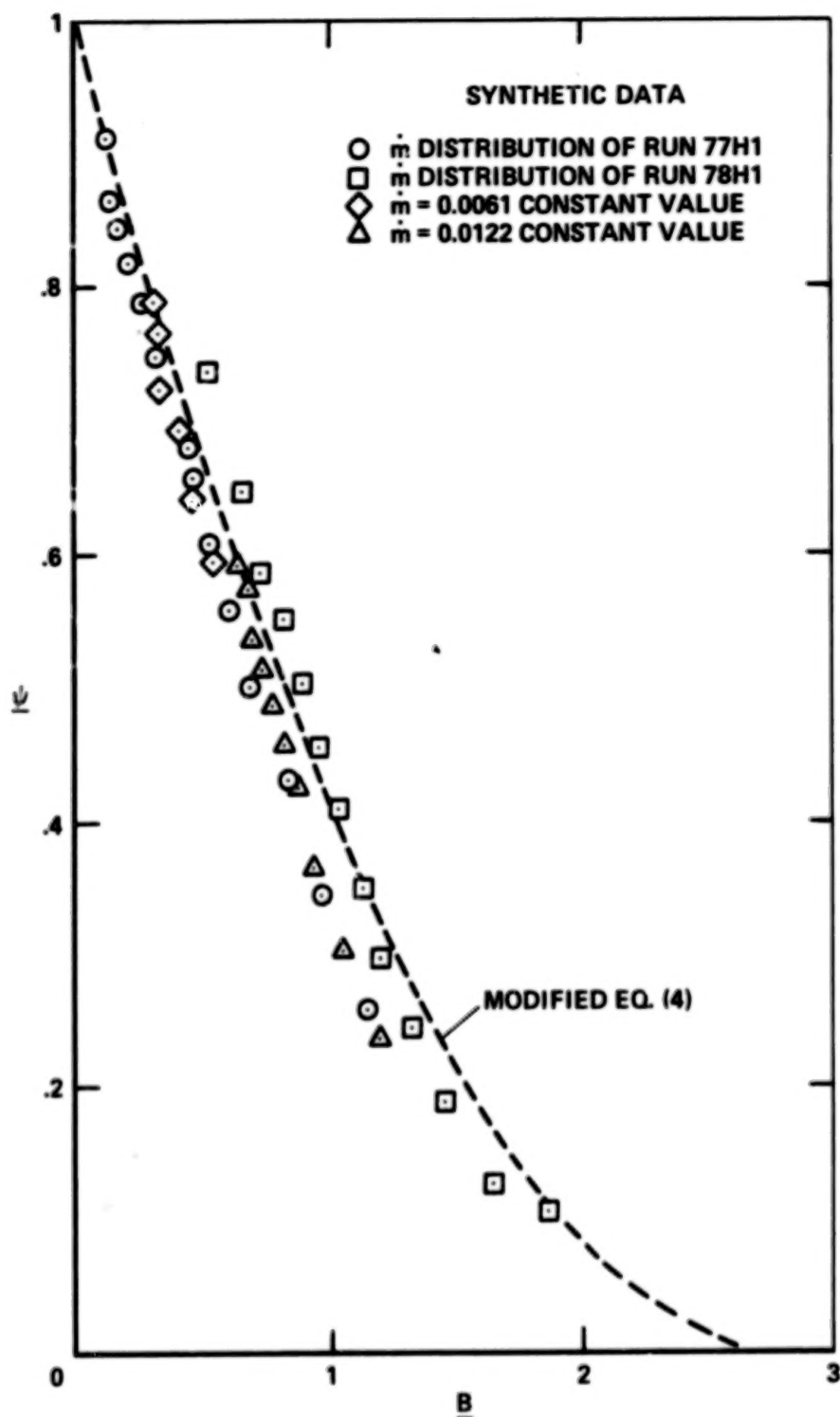
Figure 9.- Continued.

RUN	Re_D	T_{tt}	\dot{q}_0	\underline{m}^*
○ 44C2	2.10×10^5	804	14.30	-0.002
□ 48C2	2.20×10^5	783	13.63	0.004
◇ 47C2	2.14×10^5	796	14.29	0.029
△ 46C2	1.80×10^5	879	17.08	0.056
▵ 45C2	2.06×10^5	813	14.70	0.071
◁ 53C2	2.25×10^5	771	13.63	0.079
○ 52C2	2.11×10^5	801	14.60	0.135



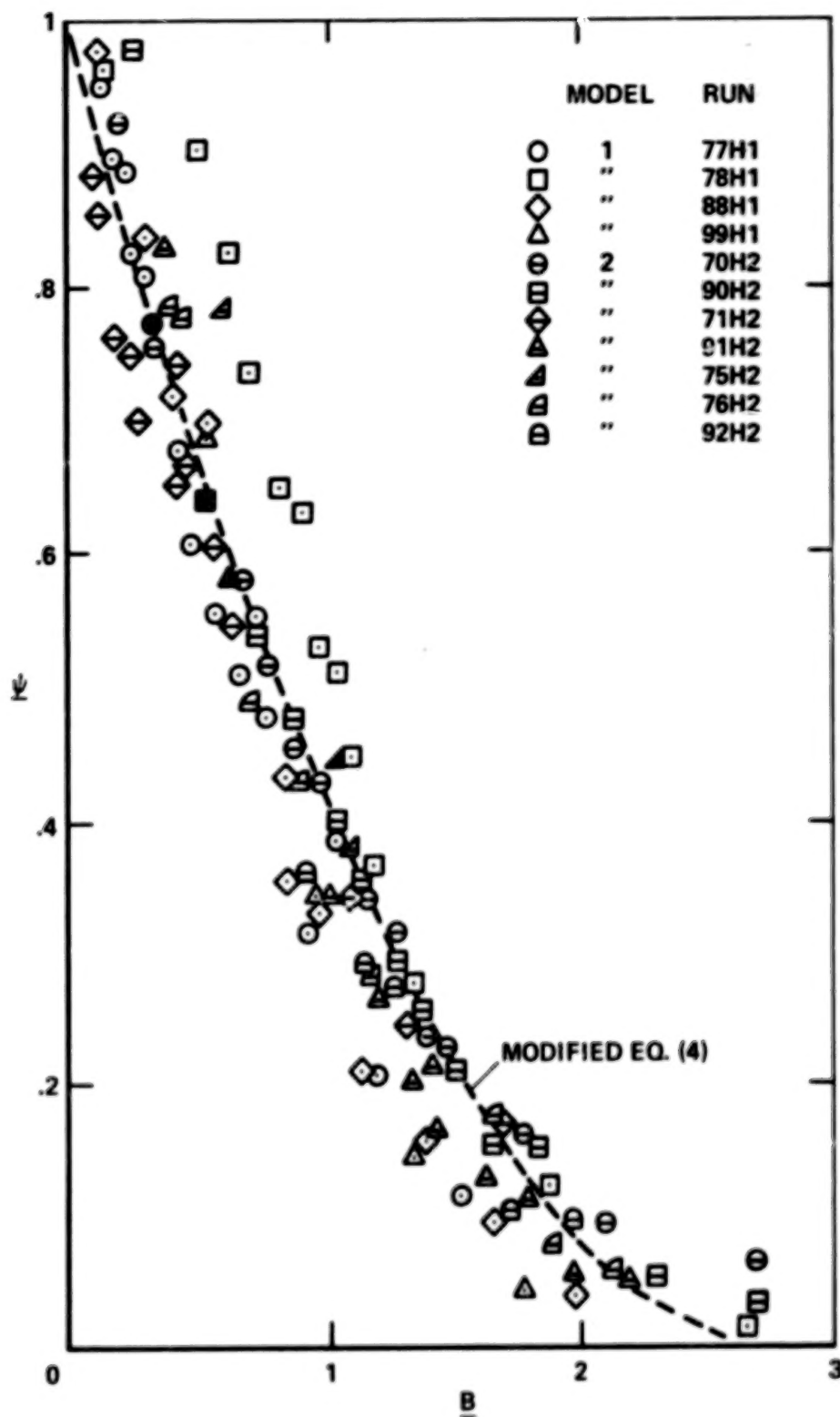
(c) $P_{tt} \approx 552 \text{ N/cm}^2$ (800 psi), $-0.002 < \underline{m}^* < 0.135$.

Figure 9.- Concluded.



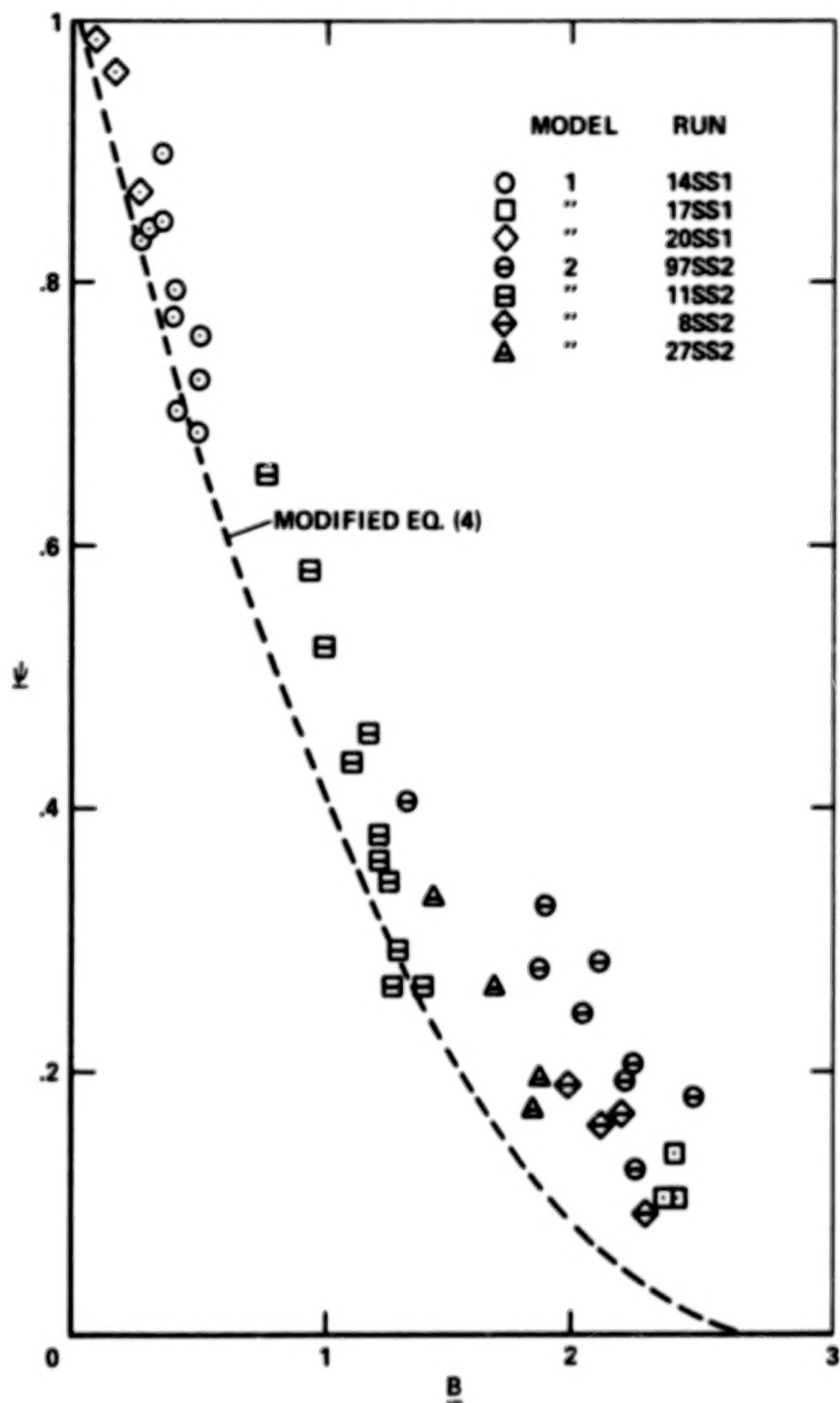
(a) Data generated by boundary-layer code of reference 5 for hemispherical model.

Figure 10.- Correlation of laminar heating rate ratio ψ with mass addition parameter B .



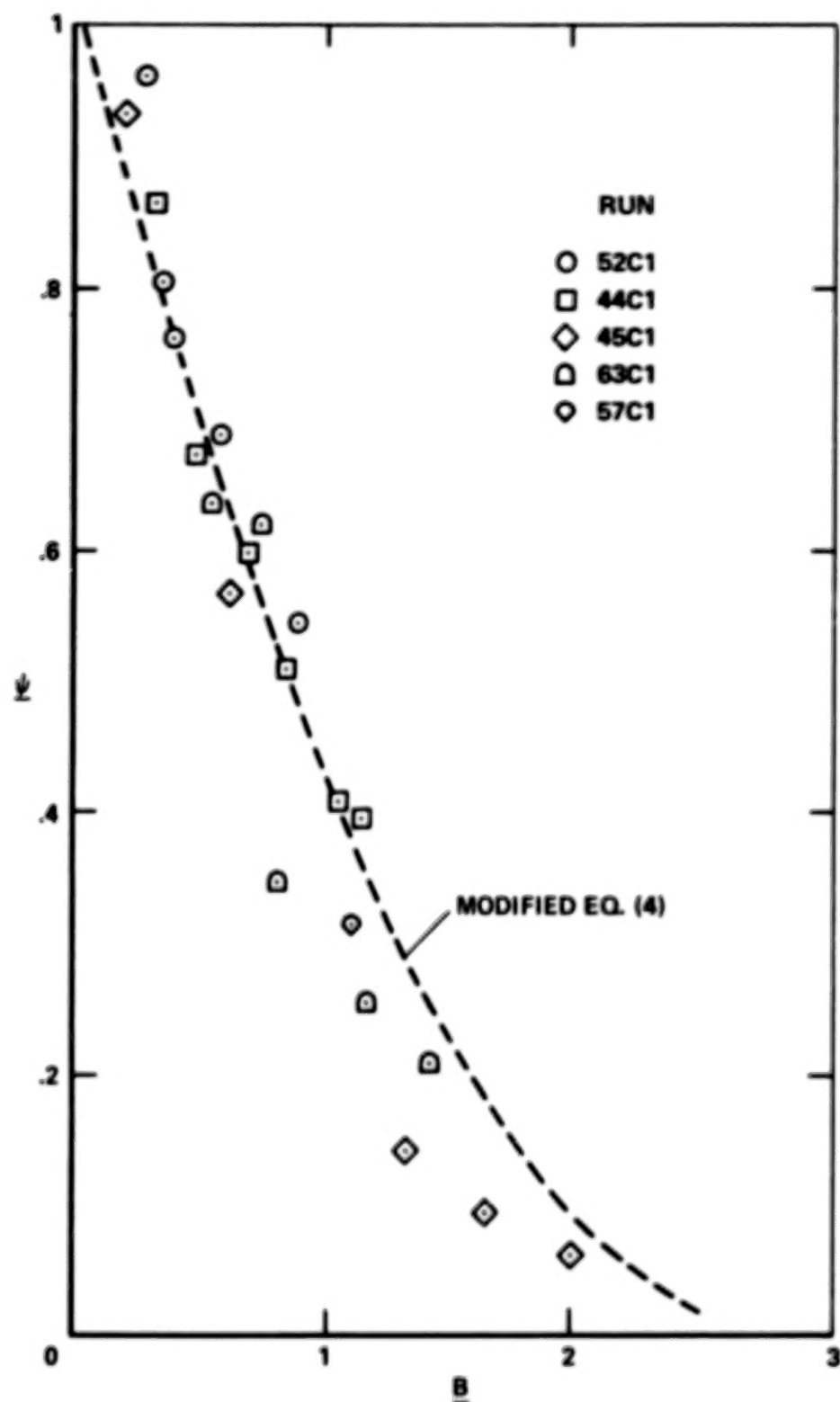
(b) Experimental data, hemispherical model.

Figure 10.- Continued.



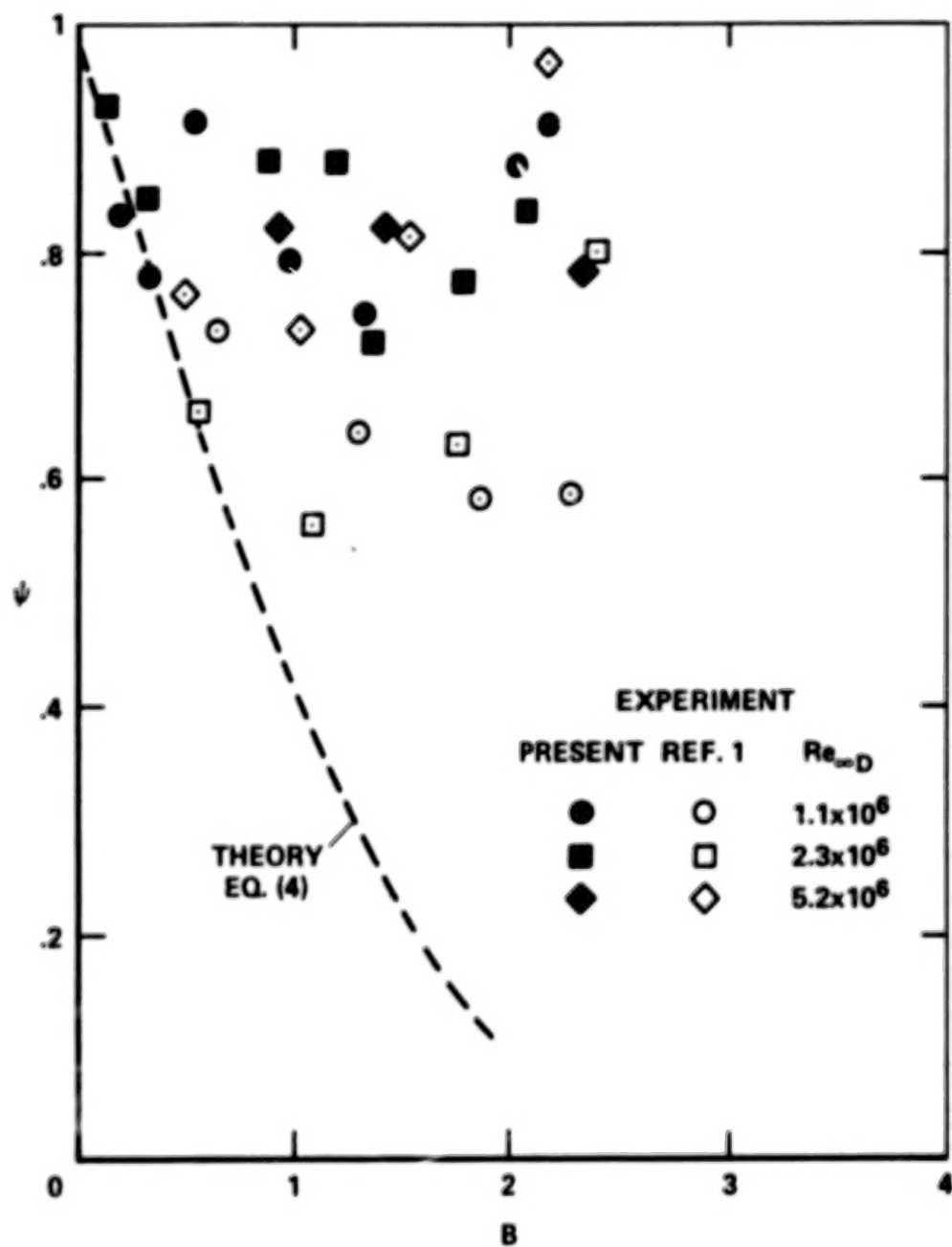
(c) Experimental data, spherical segments.

Figure 10.- Continued.



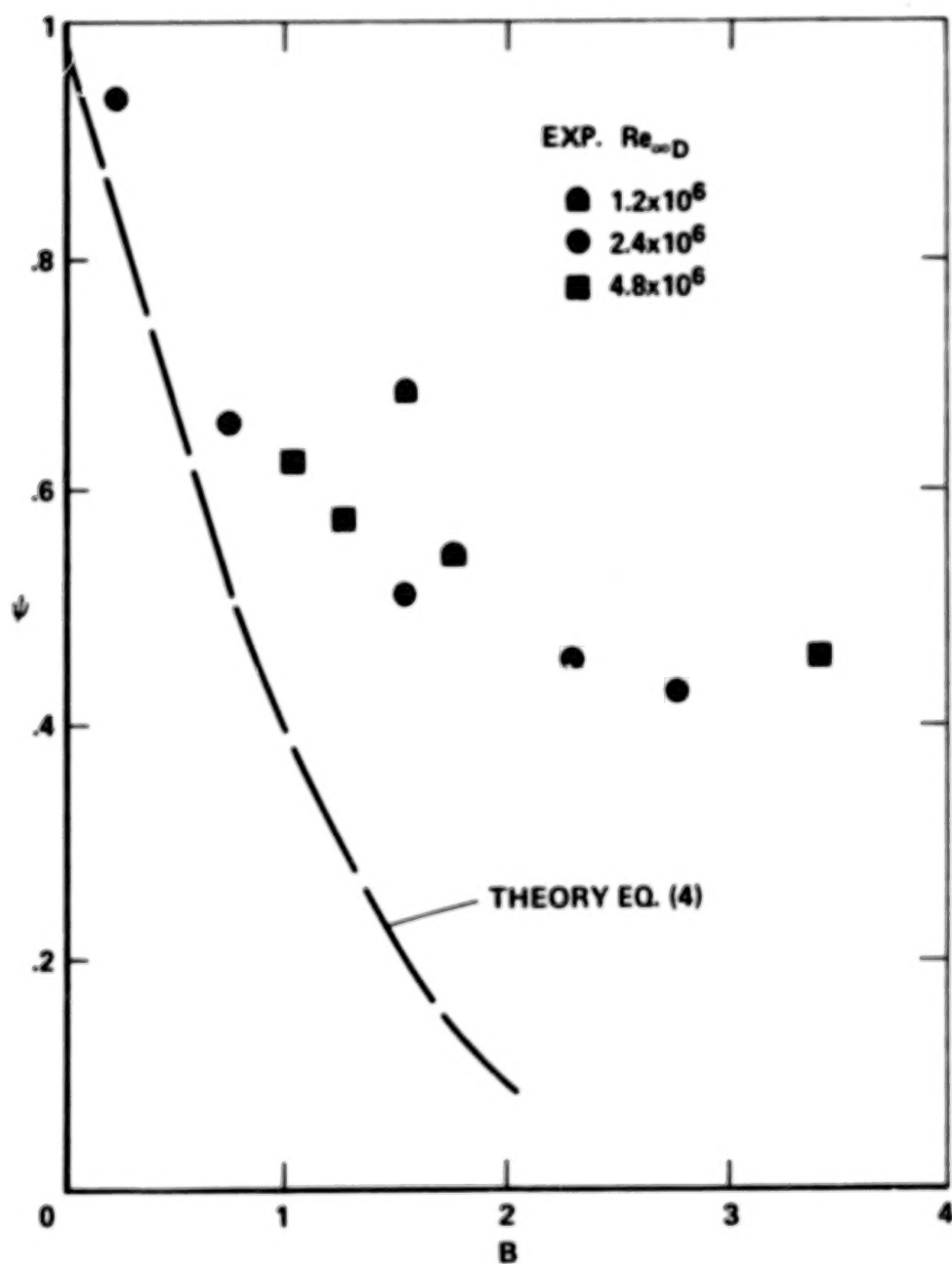
(d) Experimental data, conical model 1.

Figure 10.- Concluded.



(a) Hemispherical model.

Figure 11.- Effect of mass addition on stagnation point heat transfer.



(b) Spherical segment model.

Figure 11.- Concluded.

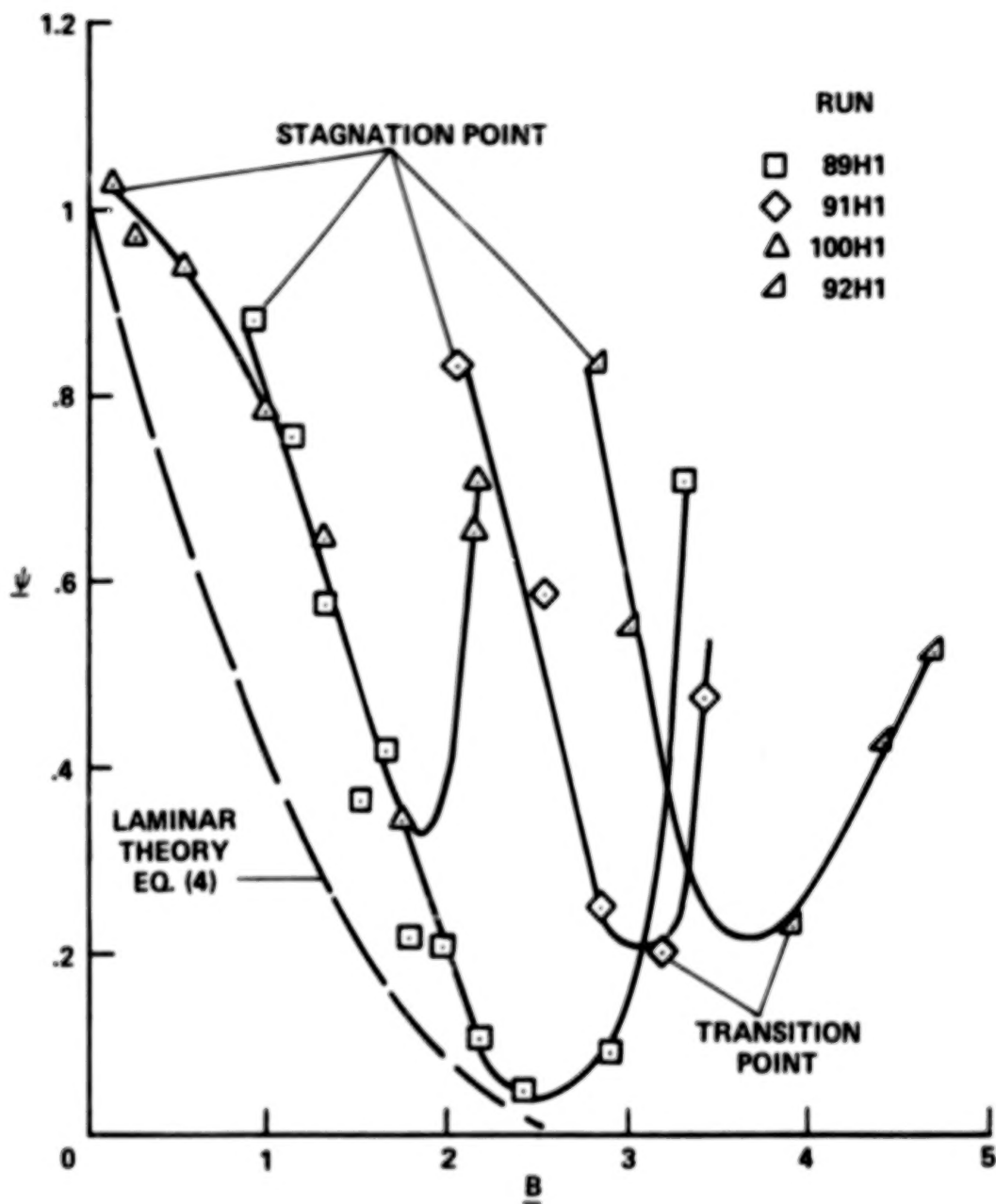


Figure 12.- Typical heating rate distribution downstream of anononously heated stagnation point, hemispherical model 1.

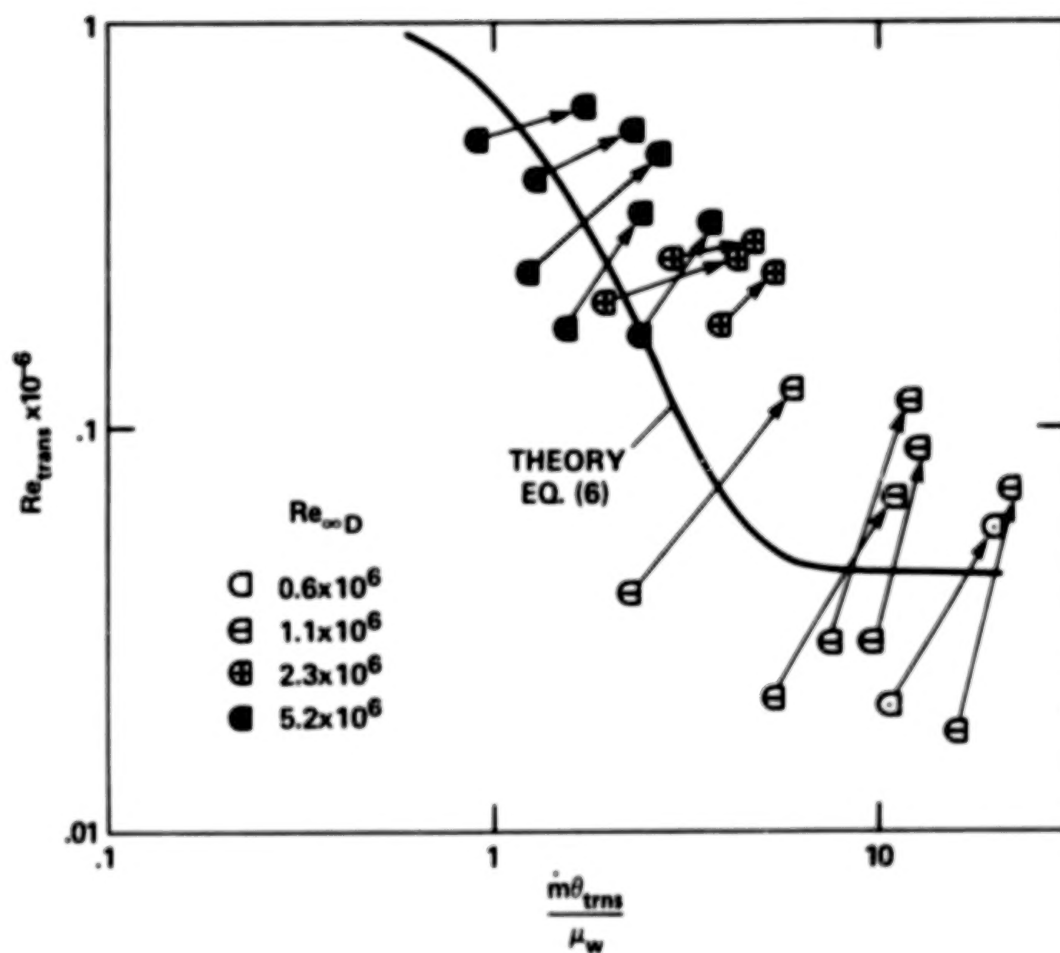


Figure 13.- Correlation of transition Reynolds numbers, hemispherical model.



Figure 14.- Photomicrograph of hemispherical model surface (20x).

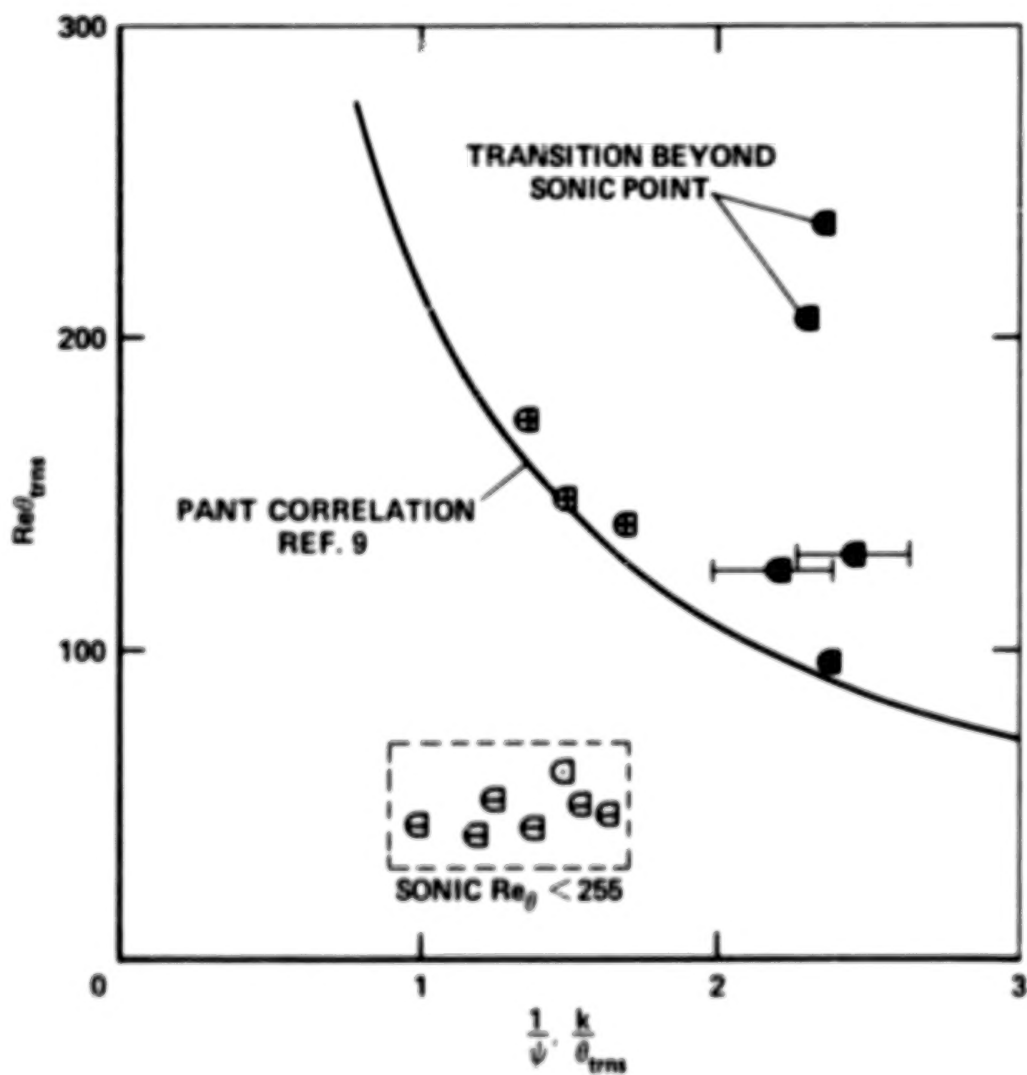
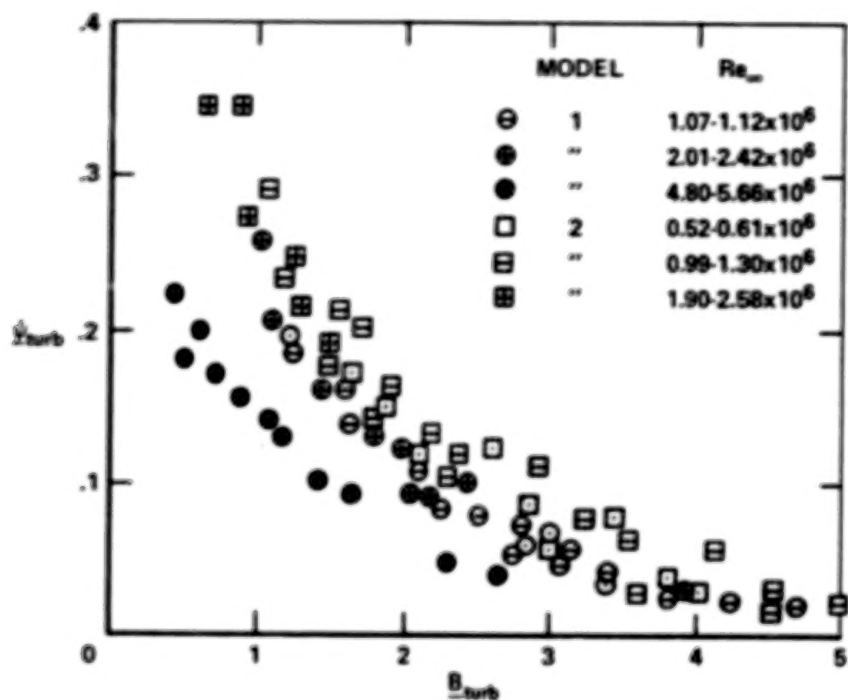
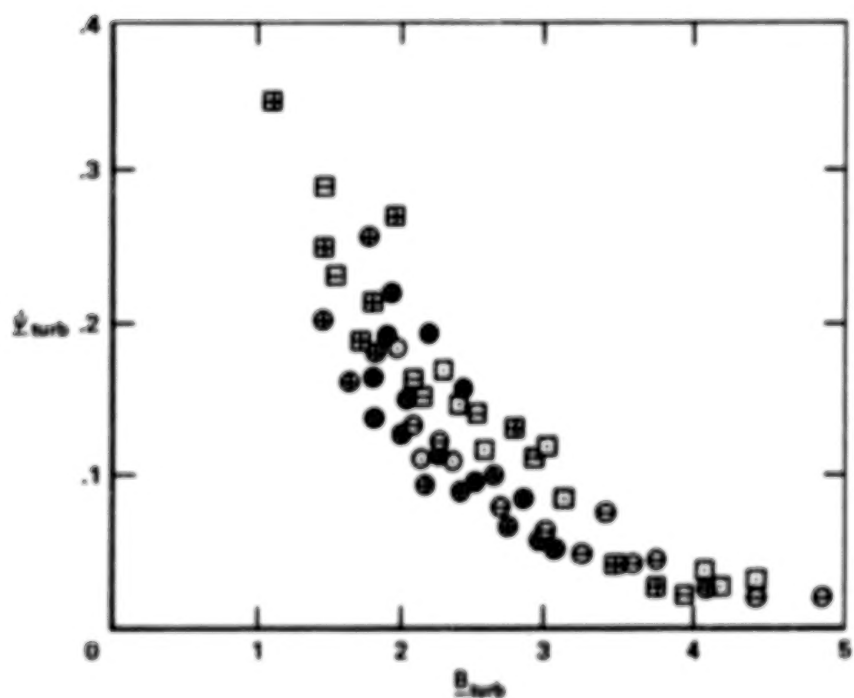


Figure 15.- PANT boundary-layer transition correlation, hemispherical model.



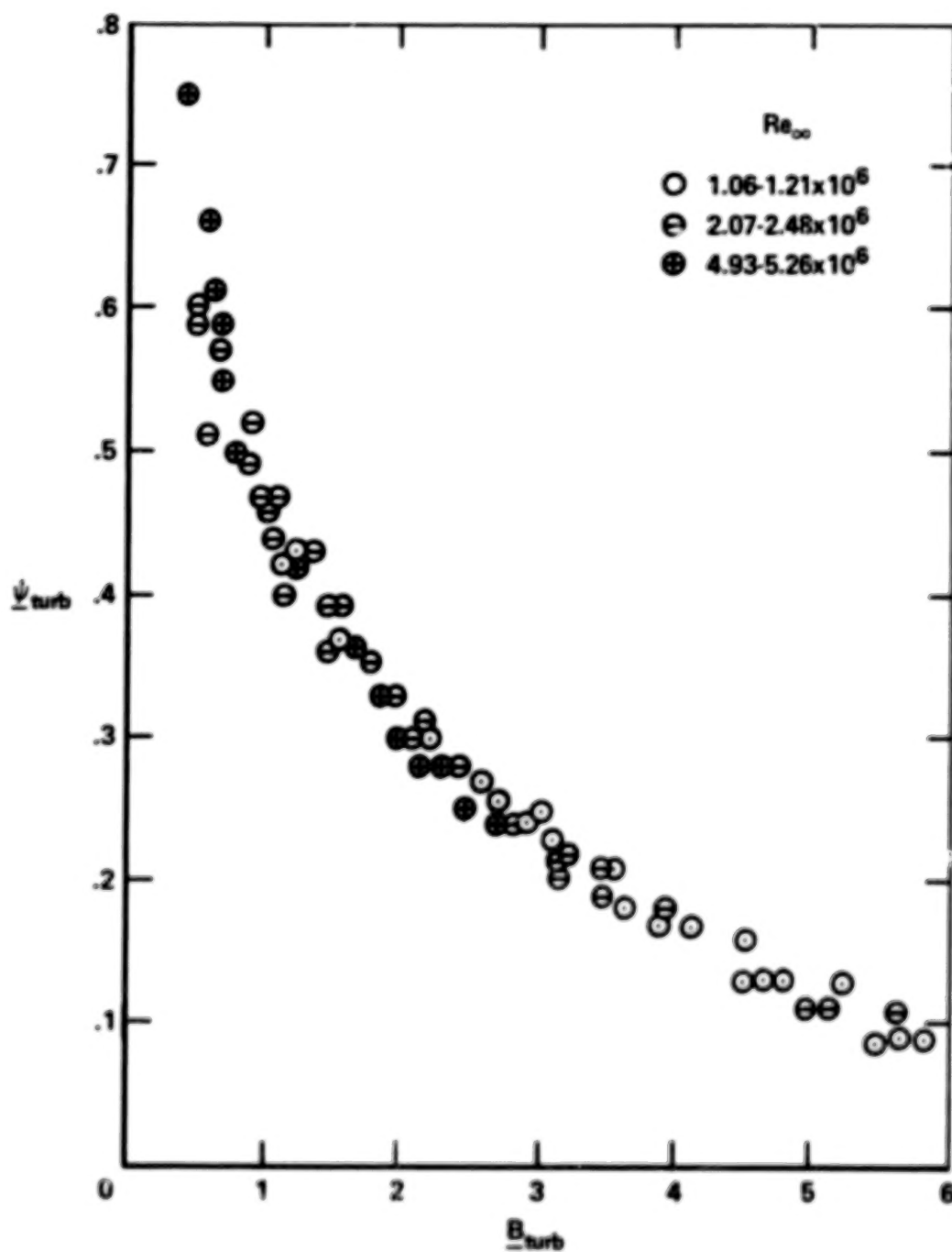
CASE I. FULLY TURBULENT HEATING REFERENCE



CASE II. MODIFIED TURBULENT HEATING REFERENCE

(a) Experimental data, hemispherical models.

Figure 16.- Correlation of turbulent heating rate ratio ϕ_{turb} with mass addition parameter \underline{B}_{turb} .



(b) Experimental data, conical model 1.

Figure 16.- Concluded.

1. Report No. NASA TP-1139		2. Government Accession No.		3. Recipient's Catalog No.	
4. Title and Subtitle EFFECTS OF MASS ADDITION ON BLUNT-BODY BOUNDARY-LAYER TRANSITION AND HEAT TRANSFER				5. Report Date January 1978	
				6. Performing Organization Code	
7. Author(s) George E. Kaattari				8. Performing Organization Report No. A-7169	
9. Performing Organization Name and Address NASA Ames Research Center Moffett Field, California 94035				10. Work Unit No. 506-26-01-00-21	
				11. Contract or Grant No.	
12. Sponsoring Agency Name and Address National Aeronautics and Space Administration Washington, D.C. 20546				13. Type of Report and Period Covered Technical Paper	
				14. Sponsoring Agency Code	
15. Supplementary Notes					
16. Abstract <p>The results are presented for an experimental investigation on the effects of mass addition on boundary-layer transitions for blunt bodies tested at Mach number 7.32. The model bodies tested were hemispheres, blunt cones, and spherical segments. The mass addition consisted of air ejected through porous forward surfaces of the models. The experimental data consisted of heat transfer measurements from which boundary-layer transitions were deduced. The data verified various applicable boundary-layer codes in the laminar and transitional flow regimes. Empirical heating rate data correlations were developed for the laminar and turbulent flow regimes.</p>					
17. Key Words (Suggested by Author(s)) Blunt-body heat transfer Boundary-layer transition Binary boundary layers Transpiration cooling				18. Distribution Statement Unlimited STAR Category - 34	
19. Security Classif. (of this report) Unclassified		20. Security Classif. (of this page) Unclassified		21. No. of Pages 66	
				22. Price* \$4.50	

*For sale by the National Technical Information Service, Springfield, Virginia 22161